The Early Stages of Halide Perovskites Thin Film Formation

Marion A. Flatken

Univ.-Diss.

zur Erlangung des akademischen Grades
"doctor rerum naturalium"
(Dr. rer. nat.)
in der Wissenschaftsdisziplin "Anorganische Chemie"

- publikationsbasierte Dissertation -

eingereicht an der

Mathematisch-Naturwissenschaftlichen Fakultät
Institut für Chemie
der Universität Potsdam

und

Helmholtz-Zentrum Berlin für Materialien und Energie

Tag der Disputation:

1. Gutachter: Prof. Dr. Andreas Taubert

2. Gutachter: Prof. Dr. Antonio Abate

3. Gutachter: Prof. Dr. Denis Gebauer

Abstract

As climate change worsens, there is a growing urgency to promote renewable energies and improve their accessibility to society. Here, solar energy harvesting is of particular importance. Currently, metal halide perovskite (MHP) solar cells are indispensable in future solar energy generation research. MHPs are crystalline semiconductors increasingly relevant as low-cost, high-performance materials for optoelectronics. Their processing from solution at low temperature enables easy fabrication of thin film elements, encompassing solar cells and light-emitting diodes or photodetectors. Understanding the coordination chemistry of MHPs in their precursor solution would allow control over the thin film crystallization, the material properties and the final device performance.

In this work, we elaborate on the key parameters to manipulate the precursor solution with the long-term objective of enabling systematic process control. We focus on the nanostructural characterization of the initial arrangements of MHPs in the precursor solutions. Small-angle scattering is particularly well suited for measuring nanoparticles in solution. This technique proved to be valuable for the direct analyzes of perovskite precursor solutions in standard processing concentrations without causing radiation damage. We gain insights into the chemical nature of widely used precursor structures such as methylammonium lead iodide ($MAPbI_3$), presenting first insights into the complex arrangements and interaction within this precursor state. Furthermore, we transfer the preceding results to other more complex perovskite precursors. The influence of compositional engineering is investigated using the addition of alkali cations as an example. As a result, we propose a detailed working mechanism on how the alkali cations suppress the formation of intermediate phases and improve the quality of the crystalline thin film. In addition, we investigate the crystallization process of a tin-based perovskite composition ($FASnI_3$) under the influence of fluoride chemistry. We prove that the frequently used additive, tin fluoride (SnF_2), selectively binds undesired oxidized tin ($Sn(IV)$) in the precursor solution. This prevents its incorporation into the actual crystal structure and thus reduces the defect density of the material. Furthermore, SnF_2 leads to a more homogeneous crystal growth process, which results in improved crystal quality of the thin film material.

In total, this study provides a detailed characterization of the complex system of perovskite precursor chemistry. We thereby cover relevant parameters for future MHP solar cell process control, such as (I) the environmental impact based on concentration and temperature (II) the addition of counter ions to reduce the diffuse layer surrounding the precursor nanostructures and (III) the targeted use of additives to eliminate unwanted components selectively and to ensure a more homogeneous crystal growth.

Zusammenfassung

Getrieben durch den Klimawandel wächst die Dringlichkeit erneuerbare Energien zu fördern und ihre Zugänglichkeit für die Gesellschaft zu verbessern. Solarenergie ist in dieser Hinsicht von besonderer Bedeutung. Derzeit sind Metallhalogenid-Perowskit-Solarzellen ein unverzichtbarer Bestandteil der Forschung an zukünftig klimaneutraler Energiegewinnung. Metallhalogenid-Perowskite (MHP) sind kristalline Halbleiter, die als kostengünstige und leistungsstarke Materialien für die Optoelektronik zunehmend an Bedeutung gewinnen. Ihre Verarbeitung aus Flüssigkeit bei niedriger Temperatur ermöglicht eine effiziente Herstellung von Dünnschichtelementen, zu denen nicht nur Solarzellen, sondern auch Leuchtdioden oder Photodetektoren zählen. Das Verständnis der Koordinationschemie in den Vorläuferlösungen der MHPs würde es daher ermöglichen, die Kristallisation der Dünnschichten, ihre Materialeigenschaften und die finale Leistung der entsprechenden Bauelemente zu kontrollieren. In dieser Arbeit werden die wichtigsten Parameter zur systematischen Beeinflussung der Vorläuferlösung ausgearbeitet, mit dem langfristigen Ziel eine systematische Prozesskontrolle zu ermöglichen.

Dabei liegt ein Schwerpunkt auf der Anwendung einer nanostrukturellen Technik zur Charakterisierung erster Anordnungen in der Perowskit-Vorläuferlösung. Die Kleinwinkelstreuung eignet sich besonders gut zur nanostrukturellen Charakterisierung von entsprechenden Teilchen bzw. Clustern in Lösung. Mit dieser Methodik können wir auf direktem Wege Perowskit-Vorläuferlösungen in üblichen Verarbeitungs-konzentrationen analysieren. Wir erhalten Einblicke in die chemische Beschaffenheit der Vorläuferstrukturen und untersuchen zudem verschiedene Perowskit-Zusammensetzungen. Strukturelle Erkenntnisse über die Vorstufe im allgemein bekanntestem MHP, Methylammoniumbleijodid (MAPbI$_3$) werden präsentiert und im Folgenden auf komplexere Anwendungen übertragen. Weiterhin wird der Einfluss von Kompositionsvariation am Beispiel der Zugabe von Alkali-Kationen (K, Rb, Cs) untersucht. Es wird ein detaillierter Wirkmechanismus vorgestellt, der erklärt, wie Alkali-Kationen die Bildung von Zwischenphasen unterdrücken und zudem die Qualität der kristallinen Dünnschicht verbessern.

Unter Berücksichtigung vorangehender Ergebnisse, thematisiert diese Arbeit zudem den Kristallisationsprozess einer zinnbasierten Perowskit-Zusammensetzung (FASnI$_3$) unter dem Einfluss von Fluoridchemie. Das häufig zugesetzte Additiv, Zinnfluorid (SnF$_2$), bindet selektiv unerwünschtes, oxidiertes Sn(IV) bereits in der Vorläuferlösung. Dieses verhindert dessen Einbau in die eigentliche Kristallstruktur und verringert so die Defektdichte des Materials. Darüber hinaus führt SnF$_2$ zu einem homogeneren Kristallwachstumsprozess, was eine bessere Kristallqualität des Dünnschichtmaterials und somit final eine bessere Solarzellenleistung zur Folge hat.

Insgesamt bietet diese Studie eine detaillierte Charakterisierung des komplexen Systems der Perowskit-Vorläuferchemie und liefert dabei notwendige Parameter, die für die zukünftige Prozesssteuerung von Relevanz sind.

Contents

1   Introduction

Higher global temperatures are only one consequence of the climate change we are currently experiencing. This warming leads to increasingly frequent extreme weather events that cause massive damage around the world.[1] One significant component of climate change is the transition to low-carbon energy production. Roughly 2/3 of global greenhouse gas emissions can be attributed to energy production and use.[2,3] Thus, decarbonizing the energy sector is of urgent interest on a worldwide scale. Emissions must be reduced to minimize environmental consequences. Hence, the shift to renewable sources must occur as fast as possible.[4] One goal set by the International Renewable Energy Agency (IRENA) is to minimize energy-related carbon emission by about 70 % by 2050 to keep the global temperature rise below 2°C. Thus, the necessity to replace current energy production with renewable alternatives is more urgent than ever before and, in addition, represents one of the most significant challenges in world history. Besides other relevant renewable energy sources, solar photovoltaics (PV) represent one of the most promising technologies. The sun delivers roughly 1.2×10^5 TW of solar radiation to the earth, overall energy being three orders of magnitude higher than the total energy consumption on the planet (status 2014).[5–7] Thus, it seems inevitable to exploit this naturally available power in the form of electricity (PV energy) and heat.[7] However, the costs of PV installations have to be reduced significantly to make the usage more accessible for the general society.

One promising rising star in the PV sector, convincing due to low manufacturing costs combined with excellent performance, is the perovskite solar cell (PSC) technology. The light-absorbing material is a polycrystalline thin film of lead halide perovskite, which can be described by the formula ABX_3. This framework includes an A-site, commonly occupied by organic and inorganic cations such as methylammonium (MA), formamidinium (FA) or cesium (Cs), a B-site filled by bivalent metal cations like lead (Pb) or tin (Sn) and a halide anion in X-site, commonly covered by iodide, bromide or chloride (I, Br or Cl). To fabricate highly reproducible, efficient, and stable PSCs, a definable crystallinity with a high, homogeneous surface coverage of the substrate is paramount. Previous studies confirm that a controlled crystallization is the key to

reaching a good surface coverage without the undesirable presence of unordered pores.[8,9] This correlation applies to lead-free perovskites as well as to their lead-containing counterparts.[8,10–12] However, the topic of crystallization from a colloidal dispersion, as it can be assumed for the perovskite precursors, is not yet fully understood. New approaches combining the non-classical nucleation with classical nucleation theory open up a variety of possible nucleation and growth pathways that are challenging to attribute precisely to the course of perovskite crystallization.[13,14] Therefore, general processes in the early stages of crystallization need to be studied in further detail. First attempts in providing nucleation pathways for better control of the crystallization kinetics are summarized in a review by J. Wang *et al.*[9], addressing classical and non-classical nucleation and growth theories. Considering the complexity of these pathways presented by J. J. De Yoreo *et al.* following the non-classical nucleation theory, the need for a better understanding of the precursor solution is essential for further development, especially for tin-based PSCs.[14]

The research about morphology improvement of perovskite thin films is advancing. Still, studying the crystallization mechanism can be of particular interest to understand the targeted use of additives,[15–19] solvent engineering[20–23] and lead-free alternatives, considering their poor morphology (i.e. low coverage and formation of pinholes) derived from its fast crystallization.[24–26] Identifying parameters to consciously manipulate crystal nucleation and growth can decisively advance perovskite-based PV science. The long-term objective will be to manufacture solar cells according to individual needs and optimally adapt them to the required production processes (with particular regard to upscaling processes towards commercialization).

Thus, the presented dissertation aims to pave the way for the first steps towards this long-term goal. Thereby a strong focus is set on using small-angle scattering (SAS) as a valid technique to characterize the early stages of perovskite crystallization from their precursor solution. In combination with various other powerful techniques, this work focuses on the structural characterization of perovskite precursor solutions to develop appropriate criteria that can be used as a starting point towards controllable tailor-made PSC fabrication.

Outline

This dissertation is divided into six major chapters. The results comprise three chapters, each of published studies, which I conducted as the first author.

In the subsequent *Chapter 2*, fundamental principles of PSCs with particular regard to the perovskite absorber material will be introduced. In addition, basic concepts of nucleation theories linked to perovskite precursor solutions and the SAS technique for nanostructure analysis will be discussed.

Diving straight into the results, the first manuscript in *Chapter 3* addresses SAS as a suitable technique for analyzing perovskite precursor solution using the example of the MAPbI$_3$ precursor solution. Uncovering size, shape and the interactions of the colloidal particles that are observed in the precursor specimen. Since the observations elucidate the importance of the inter-particle interactions within the colloidal dispersion, this work serves as a roadmap for the subsequent studies.

Chapter 4 focuses on the structural characterization of the MAPbI$_3$ precursor comparing the observed species to those from a plain PbI$_2$ solution. Furthermore, a detailed mechanism towards the perovskite crystallization process is presented, including the alkali cations' influence. Extended X-ray absorption fine structure spectroscopy (EXAFS) combined with SAS provides a comprehensive picture of the precursor structure. This knowledge is then being transferred to the addition of alkali cations and their implications on the perovskite crystallization, including the standard concept of colloidal stability.

The third manuscript in *Chapter 5* provides an example of how the knowledge of precursor solution can be transferred to other systems, such as lead-free perovskites. Providing a detailed precursor solution analysis, we present the role of SnF$_2$ in the FASnI$_3$ perovskites crystallization process.

To conclude, *Chapter 6* provides a broad discussion of the outcome of the previously presented manuscripts. In doing so, these will be correlated. The most relevant parameters for the influence of the perovskite crystallization will be elaborated to return to the question posed at the very start of this dissertation.

2 Fundamentals

This section provides relevant knowledge about scientific concepts, including material and methodology used in this study. This work focuses on examining the development of perovskite solar cells (PSCs) from a diverse perspective. Therefore, standard parameters and types of perovskites will be introduced, followed by fundamental nucleation and colloidal chemistry concepts. Since this thesis emphasizes the application of scattering methods, the most crucial concepts are presented at the end of the chapter.

2.1 Perovskites and Perovskite Solar Cells

In the past decade, perovskites, particularly metal halide perovskites (MHPs), have become a material of immense interest. Providing good material properties based on their size-tunable crystal structure, MHPs initially demonstrated excellent performance as light-emitting diodes, transistors and especially in PSCs.[27–30] In the following sections, relevant fundamentals about this frontrunner material, which rapidly became unavoidable in the development of today's green energy research, are presented.

a. Perovskite Solar Cells

Initially discovered by G. Rose, the structure type of the mineral $CaTiO_3$ was named after the Russian mineralogist L. Perovski in 1839. This first-published orthorhombic (*Pnma*) structure is a representative of the perovskite structure consisting of ABX_3. However, the corresponding aristotype is cubic (*Pm3m*). The most significant characteristic for perovskites is the corner-sharing octahedron BX_6 surrounded by a relatively large cation A (**Figure 1a**). In 1926 V. Goldschmidt defined a range of possible ionic radii for the formula ABX_3 resulting in the pseudo-cubic perovskite structure.[31] The originating Goldschmidt tolerance factor can be used to predict in which crystal system the composition might crystallize (**Figure 1b**). The perovskite type can generally be divided into oxides, sulfides, and halide perovskites. Typically, this material class is used in electrical engineering as capacitors for heterogeneous catalysis or filters and oscillators in various microwave systems. In this work, however, we focus on the use of

lead halide perovskites for solar cell fabrication. Thereby, the already mentioned ABX_3 framework most commonly comprises an A-site, occupied by organic and inorganic cations such as methylammonium (MA), formamidinium (FA) or cesium (Cs), a B-site covered by bivalent lead (Pb) or tin (Sn) cations and an X-site filled with halide anions such as iodide, bromide or chloride (I, Br or Cl).
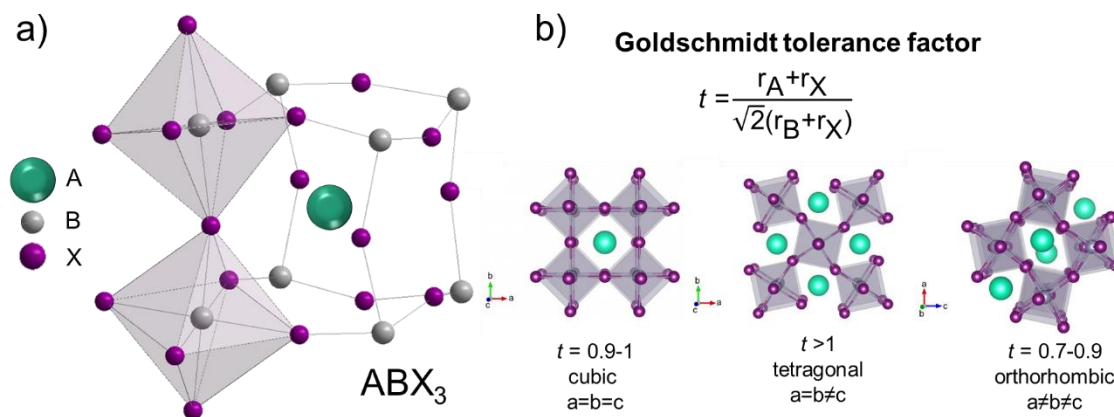
Figure 1. Perovskite type crystal structure. a) Illustration of corner-sharing octahedral of the ABX_3 framework according to the cubic structure of $MAPbI_3$. b) Goldschmidt tolerance factor and the possible crystal systems based on different radii combinations. The illustration of different crystal systems is based on the $CsSnI_3$ composition presented by E. Lora Da Silvia and coworkers. Reprinted figure with permission from E. Lora Da Silvia et al. (Phys. Rev. B, 91, 144107, 2015). Copyright (2021) by the American Physical Society.[32,33]

A. Kojima *et al.* presented the first study on the ability of MHPs to efficiently convert visible-light in photo-electrochemical cells in 2009.[34] Starting from an initial power conversion efficiency (PCE) of 3.8 %, only a few years later this was more than doubled by developing the material and the cell architecture to achieve 10.9 % in 2012.[35] This rapid growth quickly attracted the attention of the scientific community. To this day, many scientists are working on improving these materials to make them suitable for large-scale industrial use. In emerging PV technologies, PSCs hold a record efficiency of 25.5 % (on a lab scale).[36] Due to this rapid increase in PCE and additional compelling material features, MHPs offer one promising opportunity for future renewable energy harvesting. Some designated material properties are the high electron mobility (800 cm^2/Vs), high charge carrier diffusion length (exceeding 1 μm) and carrier lifetime (exceeding 300 ns).[37] Besides their outstanding PV properties, the low temperature, solution-based perovskite processing is another criterion that makes it particularly well suited for fast and cost-efficient manufacturing.[38,39] An additional reason for the attractiveness of PSCs is their tunable energy gap. The choice of compositions A, B and X directly influences the Goldschmidt tolerance factor, as shown in **Figure 1b**. This

relation reflects the degree of the octahedral distortion in the perovskite crystal lattice resulting in different crystal classes. Since the orbitals of the metal (B) and halides (X) contribute to the formation of the energy gap in the perovskite, the change of the lattice parameters has a direct impact.[40–42]

Perovskites are commonly used as a polycrystalline absorber layer sandwiched between top and bottom contact transport layers for PV applications. Besides using single-junction devices, various research groups also work on tandem solar cell approaches where the perovskite layer is deposited on another semiconductor such as silicon or copper indium gallium selenide (CIGS).[43,44] In both systems, the deposition and crystallization from the precursor solution plays an essential role in the absorber morphology. Grain boundaries, as well as the oriented growth of the perovskite strongly influences the device performance.[45–47] Hence, a fundamental understanding of the perovskite growth process is of utmost importance to systematically control the device efficiency and selectively influence PV properties.

b. Solution-based processing of perovskites solar cells

One of the significant advantages of PSCs is their low-cost manufacturing enabled via solution-based fabrication methodology in combination with low-temperature annealing processes. The ability to process a polycrystalline thin film of only several hundreds of nanometers from a liquid opens up promising opportunities for future industrial production.
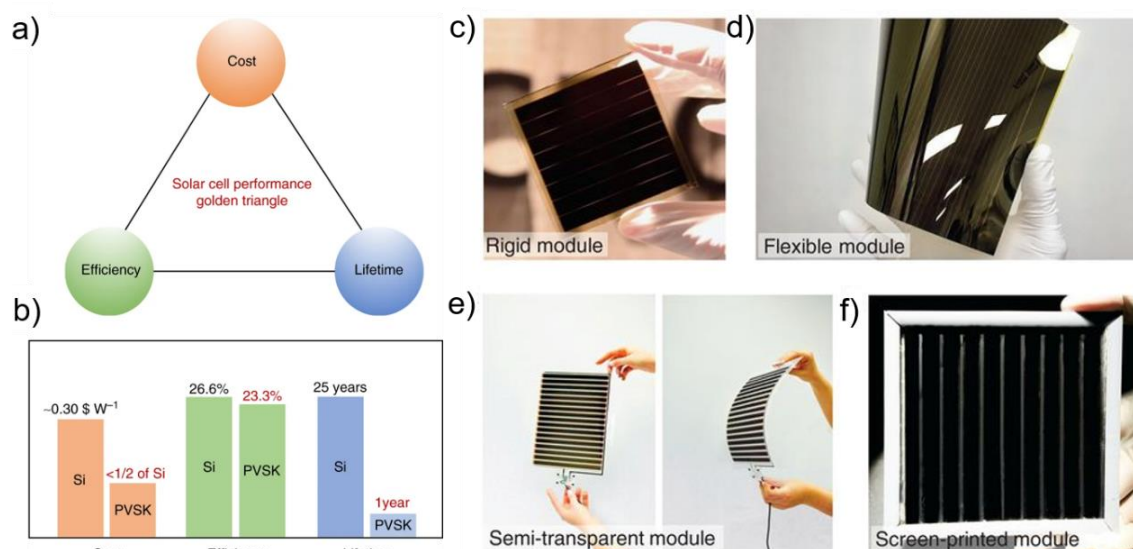
Figure 2. Future perspective for PSCs. A comparison of perovskite and silicon solar cells. a) Golden triangle of solar cells: cost, efficiency, and lifetime. From L. Meng (Nat Commun, 9, 5265, 2018). Reprinted with permission from Springer Nature.[48] b) The comparison in numbers of perovskite and silicon solar cells based on the golden triangle. From L. Meng (Nat Commun, 9, 5265, 2018). Reprinted with permission from Springer Nature.[48] Pictures of perovskite solar modules: c) Rigid perovskite mini-module. (Microquanta Semiconductor) d) Roll-to-roll processed flexible module. (Solliance Solar Research) e) Semitransparent module fabricated using an inkjet printing technique. (Saule Technologies) f) Screen-printed module by Wuhan National Laboratory for Optoelectronics at HUST. From Y. Rong (Science, 361, 1214, 2018). Reprinted with permission from AAAS.[49]

Figure 2a shows the three most relevant criteria for evaluating the technical feasibility for commercialization of PV technologies, the golden triangle consisting of cost, efficiency and lifetime. The data in **Figure 2b** are adopted from the original figure, which was published in 2018. The current PCE of PSCs in 2021 is already at 25.5 %[36,50], very close to the PCE achieved with silicon. Therefore, the direct comparison of the PSCs to their silicon counterparts demonstrates the significant cost savings of the perovskite technology. Nevertheless, the lifetime, meaning the PSC stability, is not yet comparable with the existing commercially available silicon solar cells. As presented in **Figure 2c-f** towards semitransparent or flexible modules, several upscaling techniques already proof the immense potential of the emerging PSC PV technology. The lacking stability is still a big challenge to face. Thus, it is critical to investigate these systems in more detail emphasizing their wet chemistry. The fastest achievements can be observed in lab-scale devices, commonly processed via spin-coating. For both the lab-scale processing and upscaling approaches from precursor solutions of perovskite, a fundamental understanding is needed to achieve process control and systematically improve the stability of PSCs. In the following, most relevant perovskite deposition methodologies from solution are presented, such as spin-coating in terms of laboratory-scale production and printing techniques paving the way towards commercial application.

Laboratory scale: Spin Coating

The PSCs for current record efficiencies listed in the National Renewable Energy Laboratory (NREL) chart has been prepared via spin-coating.[36] During spin-coating, which is a standard technique for uniform thin film deposition,[51] a small amount of the perovskite precursor solution of the desired composition is applied on the center of the substrate. The substrate is then rotated at a specific speed. For example, the most frequently used recipe for CsMAFA[17] and RbCsMAFA[18] (those compositions will be explained in further detail in the upcoming section) follows a two-step protocol. Thereby, a slow step with 10 s at 1000 rpm (200 rpm/s acceleration) is followed by a faster step of 20 s at 6000 rpm (2000 rpm/s acceleration).[52] The slower step should contribute to a good surface coverage from the beginning. During the second step, a specific volume of an anti-solvent is dropped in the rotation center of the substrate a few seconds before the end of the spin-coating process. Besides several other possible candidates, commonly used anti-solvent are chlorobenzene, toluene, diethyl ether, anisole or ethylacetate.[53,54] This anti-solvent step is highly sensitive to individual errors since it is not an automated process and must be executed manually by the operator. Other important parameters for the processing via spin-coating are the substrate's surface texture which strongly correlates with the surface coverage. The general precursor preparation and spin-coating setting show crucial parameters influencing the perovskite formation. Using spin-coating technique in combination with a subsequent annealing step provides an easy and fast approach to generating perovskite absorber layers for laboratory use on comparably small scale (inch by inch). Thereby quick results can be achieved, which helps to accelerate the research and optimization of full PSCs. However, the previously described anti-solvent approach involves some uncertainties. It is highly dependent on the manufacturer and, in addition, to the general environmental conditions (e.g. glove box conditions, atmosphere). For this reason, special attention needs to be dedicated to maintain the same experimental conditions to ensure comparability.

Upscaling via Printing

Besides the solution processing of PSCs on a laboratory scale, the long-term aim is to provide large devices for commercial application. To accomplish the critical challenge

of scalable PSC fabrication, the process of low-temperature crystallization from a precursor solution is of utmost importance. Some of the scalable coating and printing techniques that have attracted significant attention in the recent years of research and development are, for example, blade coating[55], slot-dye coating[56,57] and inkjet printing[58–60]. The fabrication of a good quality thin film for PSCs requires absolute control over the process window and well-managed removal of solvents to perform the crystallization in a targeted manner.[56] Since these are highly technical processing approaches, a good and detailed knowledge of the operation of the individual machines is a mandatory requirement. It is essential to study and understand the precursor solutions, the corresponding crystallization behavior and growth processes that lead to the formation of the polycrystalline perovskite thin film to achieve the best results. Then, the possibilities of the various methods can be fully exploited, and systemic upscaling can be promoted to ensure that PSCs become a viable option in the future.

c. Compositional Diversity of Metal Halide Perovskites

The ABX_3 framework, previously introduced, indicates that the application of MHPs does not only allow for selecting just one particular composition of materials. What started with a simple methylammonium lead iodide ($MAPbI_3$) perovskite providing optoelectronic properties was soon no longer sufficient. The fast forward-moving field of PSC research and the demand for consistently achieving a higher device performance led to many different approaches to improve the firstly introduced $MAPbI_3$ perovskite. Besides the pursuit of high efficiency, stability, and the ability to adjust the bandgap are other driving forces to develop further compositional engineering of PSCs. For instance, for silicon-perovskite tandem devices, a wide bandgap perovskite would be preferred. However, changing the perovskite components does directly impact the fundamental materials properties. Compositional modifications significantly influence the precursor solution, the nucleation and finally the growth of the perovskite. The implications are reflected in the systems' stability and their crystalline phase transitions. In the following some of the most relevant compositional variations will be addressed.

$MAPbI_3$ and $MAPbBr_3$ were the first published MHP showing PV properties.[61] The general form of ABX_3, in that case, consists of MA^+ as A-site cation and lead filling the metal cations position. Based on the specific condition, the current literature identifies

three polymorphs for MAPbI$_3$: cubic, tetragonal or orthorhombic.[62–64] This, however, implicates that the structure may undergo phase transitions at different temperatures and pressures that need to be considered. The orthorhombic MAPbI$_3$ is expected at standard pressure and temperatures below 162 K. At room temperature it converts into the tetragonal, and at temperatures above 327 K, into the cubic crystal system. The rising temperature leading to higher symmetry indicates the change in crystal lattice dynamics, especially the octahedral distortion, over the phase transitions.[65–67] Even though the composition stays the same, the phase significantly influences the material properties, particularly the energetic properties such as the band gap. Typically, the band gap varies from 1.3 eV for the symmetric cubic to 1.61 eV for the orthorhombic crystal system.[68] Using the example of MAPbI$_3$, scientists have explored the role of hydrogen bonding in organic MHPs and its influence on the octahedral tilting, which might be one crucial key parameter to understand better and control systematically the stability of the material.[64] The corner-sharing octahedral iodidoplumbate substructures and their tilting are significant for the perovskite stability as it is characteristic for this class of materials. The corner-sharing octahedron linkage distinguishes the perovskite crystal structure from other structures such as the edge-sharing precursor PbI$_2$ (which serves as degradation product of MHPs).[69] Since this is the first explored PV-active perovskite composition and comparably simple to fabricate, it is one of the most studied MHPs in PSC history.[56,64,70–73] Although the first results using MAPbI$_3$ in PSC were promising[34,35], the PCE seems to be reaching a limit at around 21 %, which was not yet overcome.[56,74–76] Another challenge is the comparably poor thermal stability of the small organic cation MA$^+$.[77] One promising alternative is FA$^+$, which is larger in size than MA$^+$ and therefore thermally more stable.[78,79] In recent years, the MA$^+$ and FA$^+$ were exchanged or shared the A-site of the ABX$_3$ formation.[77,80–82] Still, other monovalent cations were introduced to improve the thin film morphology in multi-cation approaches.[17,18] The addition of alkali metal cations, mostly Cs$^+$, Rb$^+$ and K$^+$, has been successfully used to achieve higher reproducibility and enhanced device stability.[17,83,84] This approach also led to the publication of one of the most widely used perovskite compounds to date, referred to as "triple cation" perovskite, since three cations (Cs$^+$, FA$^+$ and MA$^+$) share the A-site position.[17,52] This perovskite composition is known to form PSCs with excellent stability and reproducibility.[17]

Although the leading research in MHP is currently building on lead-containing materials, the lead goes along with great responsibility considering the environmental protection. Lead from perovskite gets absorbed effectively from plants if dispersed into the soil. Therefore, it can directly contaminate the food cycle.[85] A. Abate *et al.* proved that the replacement of lead with tin provides a far more environmentally sustainable alternative.[85] In 2014, the group of H. J. Snaith presented the first lead-free PSCs using methylammonium tin iodide (MASnI$_3$) with a PCE of 6.4 %.[86] Currently, the champion PCE is approaching already 15 % using formamidinium tin iodide (FASnI$_3$).[87] However, tin-based PSCs' efficiencies are still far below their theoretical limit, which underlines their great potential still to be unleashed. These materials face diverse challenges, such as their stability to oxidation and uncontrolled crystallization. Consequently, exploiting this by working on those lead-free alternatives is a challenge and motivation for many scientists to date.

2.2 Nucleation & Growth of Colloidal Systems

Complex shapes have always been a fascination of human kind and a driving force in pushing scientific research forward. The control of particle size and shape, especially in nanometer scale, can provide new pathways towards novel applications and properties. Colloids form the link between the atomic and the bulky dimension. Thus, the dimensional control is of particular interest for colloid science.[88]

In this section, the most relevant fundamentals of colloid science are presented. Colloid science itself is characterized by interdisciplinarity. In this sense, it encompasses intersecting research areas, such as physics, material science, chemistry and many other disciplines.[88] Colloids may consist of particles in the range of 10^{-9} m (1 nm) to 10^{-6} m (1 μm) (nanoscale[89,90]). Accordingly, the terms relating to nanoscale dimensions are defined in the following section. Additionally, a collection of nucleation and growth theories is being introduced by showing mechanisms relevant for this study.

a. Nanoparticles, their Interactions and Processes

A size range of 1 nm to 100 nm is commonly used to describe the nanoscale dimension.[91,92] However, other definitions even include sizes below 1 nm (size range: 0.2 nm to 100 nm), and also specific molecules are considered to still count as nanoscale, e.g. fullerenes.[91,93] This already indicates that there is no particular limit to the size of the particles belonging to this category. Following the proposal of the British Standards Institution[90] a nanoparticle (NP) is defined as follows:

"Nanoparticle: Nano-object with three external nanoscale dimensions. The terms nanorod or nanoplate, instead of nanoparticle when the longest and the shortest axes length of a nano-object are different."

Whereby a nano-object is defined as a material composed of several nanoscale dimensions.[89] NPs reunite the atomic, the molecular and crystalline world, which is one of the reasons for the ongoing interest in elucidating their nucleation processes that are explained later on. In this work we are focusing on the behavior of NPs in colloidal systems. A colloid or a disperse phase consists of insoluble, well-dispersed particles (mostly NPs) in a solvent phase.[94,95] The specific physicochemical environment, crucial for the nucleation process, directly impacts the form and shape and thus the properties

of the NP. Furthermore, it determines how particles interact with each other. Depending on the approach and settings of the particular manufacturing process, different types of arrangements exist at the nanoscale and beyond, approaching the microscale (~100 nm – 100 μm)[96]. The minor units form the primary particles, and more extensive scale arrangements are reached by nano-object accumulation to aggregates and agglomerates. Further processes like coalescence and Ostwald ripening complement the essential processes and interactions that occur during NP formation and growth.
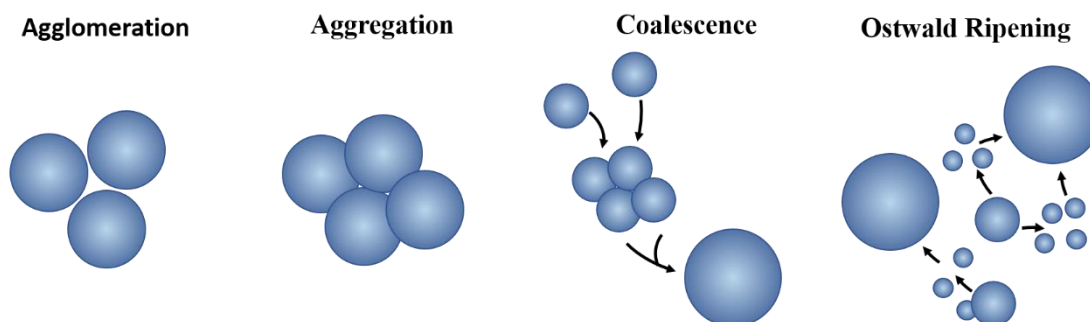
Figure 3. Schematic illustration of interacting particles: agglomeration, aggregation, coalescence and Ostwald Ripening.

The International Organization for Standardization (ISO) states that an aggregate consists of strongly bonded or merged particles.[92] Thereby the total resulting surface area may be significantly smaller than the sum of the individual surface areas of the individual particles. The formation of aggregates, their form and their shape can substantially influence the properties of a material. Generally, they range in size from the nanoscale to microscale depending on the size and number of accumulated particles.[91] Due to their high binding strength they may behave similar to strong, indivisible NPs and are not easily broken up by external forces.[97]

Therefore, not only single NPs but also aggregates may assemble and form agglomerates. In contrast to an aggregate an agglomerate consists only of weakly bonded particles connected, for instance, via van der Waals forces.[91,92] The total resulting surface area of an agglomerate equals the sum of the surface areas of all contributing individual components, as presented in **Figure 3**.

Although aggregation and agglomeration describe the assembling of nano-objects, they still differ in their inter-particle interactions. Those formations reduce the number of free particles in solution and shift the particle size distribution to larger sizes. In the same way, the primary particles growth or ripening processes, i.e. coalescence and Ostwald ripening (schematically depicted in **Figure 3**), reduce the number of particles in a

solution.[98] Coalescence describes the procedure when two nano-objects of identical composition collide and fuse to a larger particle with a strongly reduced total surface area.[99] Ostwald ripening (schematically presented in **Figure 3**) has been firstly described by W. Ostwald in 1900.[100] Here, larger particles grow at the expense of smaller particles, which means that based on the dissolution of smaller particles, the larger particles are growing. It can be viewed as the transport of matter from the surface of small particles to the surface of large particles.[101]

b. Nucleation and Growth Theories for Nanoparticles

Nucleation comprises the initial process towards the formation of a crystal from a solution, liquid or vapour.[102] Thereby, a small number of subunits (i.e. ions, atoms, molecules or clusters) arrange in a pattern specific for a crystalline solid, which serves as a site for further crystal growth.[102]

In 1926, the first approaches towards the elucidation of nucleation in supersaturated environments were published by M. Volmer and A. Weber, thereby paving the way for today's nucleation chemistry and the ability to describe first-order phase transition processes.[103] Since those transition processes cover a broad dimension range and therefore several research disciplines, it is essential to understand nucleation processes better. This thesis will apply basic concepts of nucleation and growth to the formation of polycrystalline perovskite thin films. Hence, the following provides condensed insights into the pervasive field of nucleation theory. More in-depth information is available in the related literature.[104,105]

The most fundamental description of the theoretical concept of nucleation has been studied by R. Becker and W. Döring, providing the classical nucleation theory (CNT) as a base.[106] V. K. LaMer then used this approach and further expanded it, including the nucleation and growth mechanism of NPs.[107,108] Those growth models include previously described processes like aggregation, agglomeration, coalescence and Ostwald ripening. Nowadays, however, in-situ studies enable a more detailed investigation of the transition processes. In the 2000s, researchers introduced a further developed approach to better describe the observed mechanisms during the nucleus formation and growth.[14,109] Those non-classical crystallization mechanisms offer

promising new opportunities to understand nucleation, growth and synthesis of new emerging materials.

Classical Nucleation theory

According to the CNT, nucleation is a thermodynamic model, which includes the creation of a solid particle (nuclei) in a liquid medium. Any fluctuation caused by, for example, phase separation may result in a change in the free energy of the system.[110,111] The size-dependent solubility of the particles and the liquid-solid interfacial energy form the base of CNT. This can be expressed by encountering the Gibbs-Thompson effect providing a mathematical model for the nucleation rate, including macroscopic surface energy.[106,110,111] However, the CNT only focuses on the nucleation itself, and the growth is considered a subsequent, separate event. In general, two processes need to be distinguished: homogeneous nucleation and heterogeneous nucleation. In terms of heterogeneous nucleation, NP growth occurs at nucleation sites provided by the surface of particles in solution, whereas homogeneous nucleation happens spontaneously and reasonably random. It further requires a supercritical condition, as would be the case for a supersaturated solution.
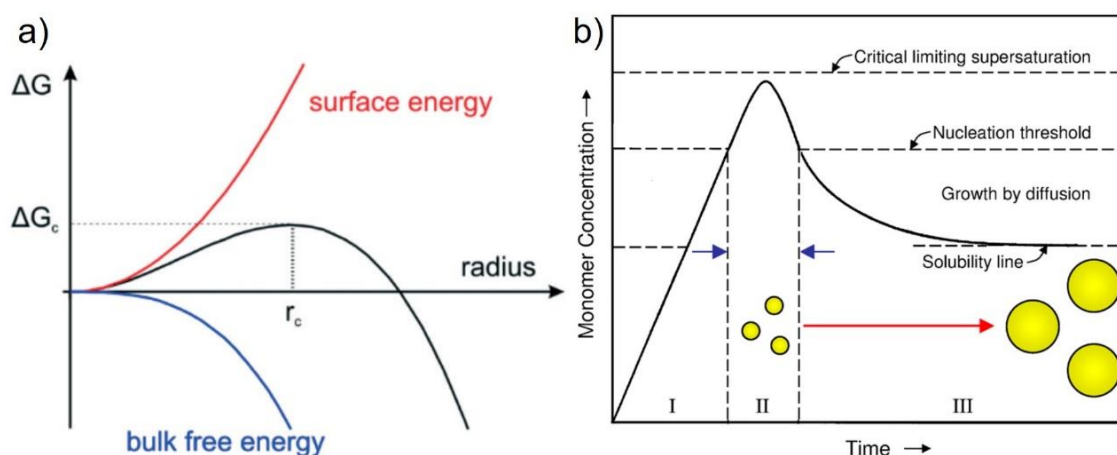
Figure 4. Models of CNT. a) Dependence of cluster free energy, ΔG, on the cluster radius according to CNT. From J. Polte (CrystEngComm, 17, 6809, 2015). Reprinted with permission from RSC.[110] b) Schematic illustration of saturation level (in monomer concentration) during nucleation and growth following LaMer model.[108] The blue arrows depict the actual nucleation period (II) followed by the red arrow demonstrating the growth (III). From F. Wang *et al.* (Chem. Mater., 26, 1, 5–21, 2014). Reprinted with permission from ACS.[112]

In the liquid phase, atoms or molecules move due to Brownian motion. This motion might result in a static collision, leading to assembles with a local structure, and a solid phase can be formed. This particle formation results in a thermodynamic gain, lowering

the Gibbs bulk free energy (**Figure 4a**). This formation can occur between two monomers or a monomer and a cluster.[110] Nevertheless, the unfavorable bond formation between those parties results in an increase of the Gibbs free surface energy.

The sum of this energy gain and loss expresses the overall Gibbs free energy as presented in **Figure 4**. Here, r_c defines a critical nucleus size assuming only one particle and one single energy. Keeping this assumption, it is possible to relate the surface energy γ_{SE} to the change of the Gibbs free energy ΔG using the following relation: $r_c = 2\gamma_{SE} / \Delta G$. The maximum of ΔG at the critical nucleation radius r_c matches the activation energy ΔG_c that is needed to overcome to form a thermodynamically stable nucleus. V. K. LaMer and R. Dinegar summarized this first nucleation approach from CNT including a growth process as a function of time dividing it into three relevant stages, assuming a reaction resulting in the formation of a monomer (**Figure 4**).[108] In the first stage (I) the monomer concentration, regarded as the saturation level of a solution, constantly rises with time until the nucleation threshold is reached. With this, the process of rapid self-nucleation starts in stage II. Reaching the critical supersaturation, the successive nucleation results in a decrease of the monomer saturation. Therefore, the nucleation rate declines as the growth of the existing nuclei commences in stage III. The particle growth thereby occurs via a diffusion-controlled mechanism with free monomers remaining in solution attaching to the surface of other particles. Stage I and II, which introduce the spontaneous nucleation, proceed rather fast considering the temporal progression. In comparison, the consecutive stage of growth (III) is relatively slow. The period of growth may include previously described processes such as aggregation, agglomeration, coalescence or Ostwald ripening (**Figure 3**).

Mainly three parameters determine the course of this time-dependent model, distinguishing between classical growths and ripening processes: the particle radius, volume and saturation level. For a classical growth process, the particles' radius increases, whereby the volume increases and the number of particles stays the same since only the already existing nuclei are growing. However, if a ripening process occurs, the number of existing particles decreases since the larger particles grow at the expense of the smaller particles. Furthermore, the total volume of particles is expected to stay unchanged, and the particle radius increases with retarded growth. This becomes possible because the critical radius shifts towards larger values. Thus, smaller particles dissolve and hence provide the matter for the growth of the larger particles.[113]

Some assumptions are required for the CNT, such as the spherical (or constant shape) nuclei, one single interfacial energy for the particle formation process and the consideration of completely homogeneous nucleation. According to today's knowledge and observations, these premises cause this theory to be far from sufficient to describe phase transition processes.[111] However, even if these requirements are not covered in most of the existing, actual systems,[110,114,115] the CNT offers essential background knowledge for the development of new approaches needed to understand nucleation and growth processes entirely.

Colloidal stability

Colloids consist of particles or clusters typically in the range of nanometers (1 nm – 1 μm, nanoscale[89,90]) interconnecting atomic to bulky dimensions. In colloidal systems with repulsive interaction, the natural control parameter is set by the diffusive transport and not by temperature as in other atomic systems.[116]

Regarding a filtered solution and hence the exclusion of impurity, nuclei are expected to form by homogeneous nucleation or by wall-induced nucleation (heterogeneous nucleation). The start of nucleation induces a random distribution of dense nuclei with enclosed surface areas. Interactions between those neighboring nuclei are the reason for their random arrangement. The solidified nuclei, NPs, are separated by grain boundaries, although bulk fluid remains in specific regions of coexistence. As long as that is the case, the NP growth process is ongoing. Hence, a further evolution of crystal shape and size occurs over time due to ripening processes at a comparably low time scale. One aspect of utmost importance in colloid science is the mechanism of NP stabilization. Colloids are considered thermodynamically unstable but kinetically stable. The primary source for the kinetic stability is the existence of an electric charge surrounding the particles surface.[94] The resulting repulsive forces control the stability of the colloidal system and can be influenced either electrostatic or sterically.[110] Without the repulsive interaction attraction triggered by van der Waals forces, electrostatic or magnetic forces between NPs commonly would lead to agglomeration, aggregation or coalescence processes. The stability concept of colloidal dispersions was developed by B. Derjaguin and L. Landau and independently by E. Verwey and J.T.G. Overbeek (DLVO), addressing the equilibrium between repulsive and attractive forces.[117,118]
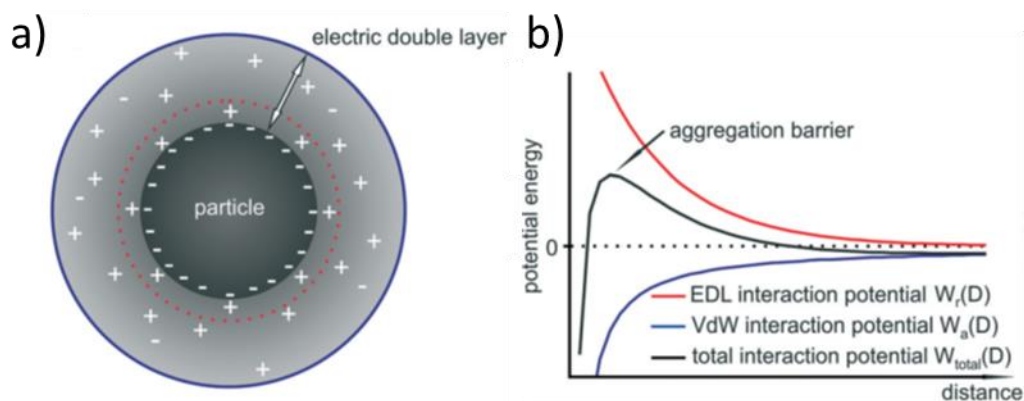
Figure 5. Fundamental concepts of the DLVO theory. a) Formed EDL around a NP including the outer diffuse layer. b) DLVO interaction potential of two NPs (black) considering the van der Waals interaction potential (blue) and the EDL interaction potential, repulsion (red). From J. Polte (CrystEngComm, 17, 6809, 2015). Reprinted with permission from RSC.[110]

The Coulomb force between individual particles decreases exponentially with their distance. With a sufficiently strong repulsion, enough distance is maintained to prevent coagulation processes successfully. The distance between charged NPs is determined by an electric double layer (EDL) made of counter ions surrounding the NP, balancing its charge and a diffuse layer (**Figure 5a**). The thickness of the formed EDL and diffusive layer depends on the ion type and concentration, the surface potential and the particle size. Those parameters directly influence the colloidal stability to be quantified via the respective aggregation barrier of two NP (**Figure 5b**). A formation of a thick diffuse layer results in sufficient large inter-particle distance to maintain a stable colloidal dispersion based on more pronounced repulsive forces compared to the attractive ones. However, a reduced layer leads to a reduced distance between the particles and therefore, the attractive forces might predominate resulting in a collapse of the double layer.[112] Adding counter ions or changing the ratio of the NP surface charge to the number of counter ions affects the dimension of the diffusive layer around the NP and therefore change the colloidal stability.[110,119] Additionally, solvent properties directly impact the system and influence the degree of particle interaction and the addition of large molecules, demonstrating a steric stabilization of the colloidal system. The strategic use of such parameters allows to modify the colloidal properties and thus to influence the nucleation and growth.

Non-classical nucleation theory approaches

Proposed in 2015 by J. Polte for most syntheses, the minimum particle size is determined by their colloidal rather than by their thermodynamic stability, as it is proposed by the CNT model (**Figure 4**).[110,111] Research on colloidal metal systems reveals that not all the observations are covered by the CNT models published.[109] Significant advancement became possible with the emergence of in-situ scattering and microscopic methodology. These techniques allowed to study the different formation and growth pathways referred to as non-classical nucleation theory. The CNT is based on the ions/molecules forming primary NPs and subsequent growth mechanism to a single crystal.[109]
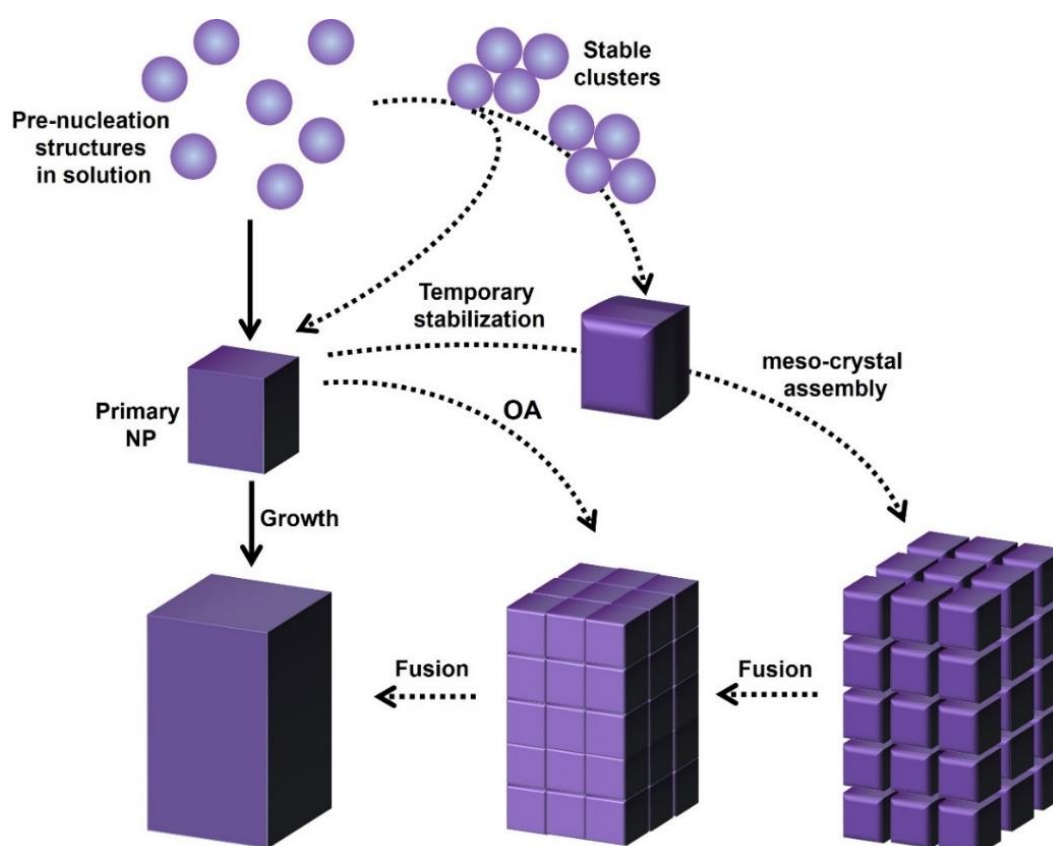
Figure 6. Schematic illustration of classical and non-classical crystallization pathways. Classical crystallization pathway represented by solid arrows and non-classical nucleation routes depicted with dotted line arrows. This figure is inspired by literature covering CNT and non-classical nucleation pathways.[109,111]

The common crystallization pathway based on CNT is provided in **Figure 6**, following the solid black arrows. However, crystallization can also occur along particle-based reaction channels, covered by the non-classical nucleation theory. The dotted arrows depict some exemplary pathways in **Figure 6**. Thereby, self-assembled pre-nucleation clusters and primary NPs can form superstructures that arise via metastable or

amorphous particles as an intermediate state.[109] The formed meso-crystals consist of highly oriented subunits that develop based on a self-assembly approach.[120,121] Due to melting processes (i.e. fusion), the meso-crystal can convert into a single crystal. Similarly, primary NPs can grow via oriented attachment (OA) to iso-oriented crystals that can fuse to a single crystal (**Figure 6**). OA represents a typical non-classical crystal growth mechanism, describing the repeated attachment events of crystalline NPs that contain specific crystal faces, which are additionally lattice-matched.[14]
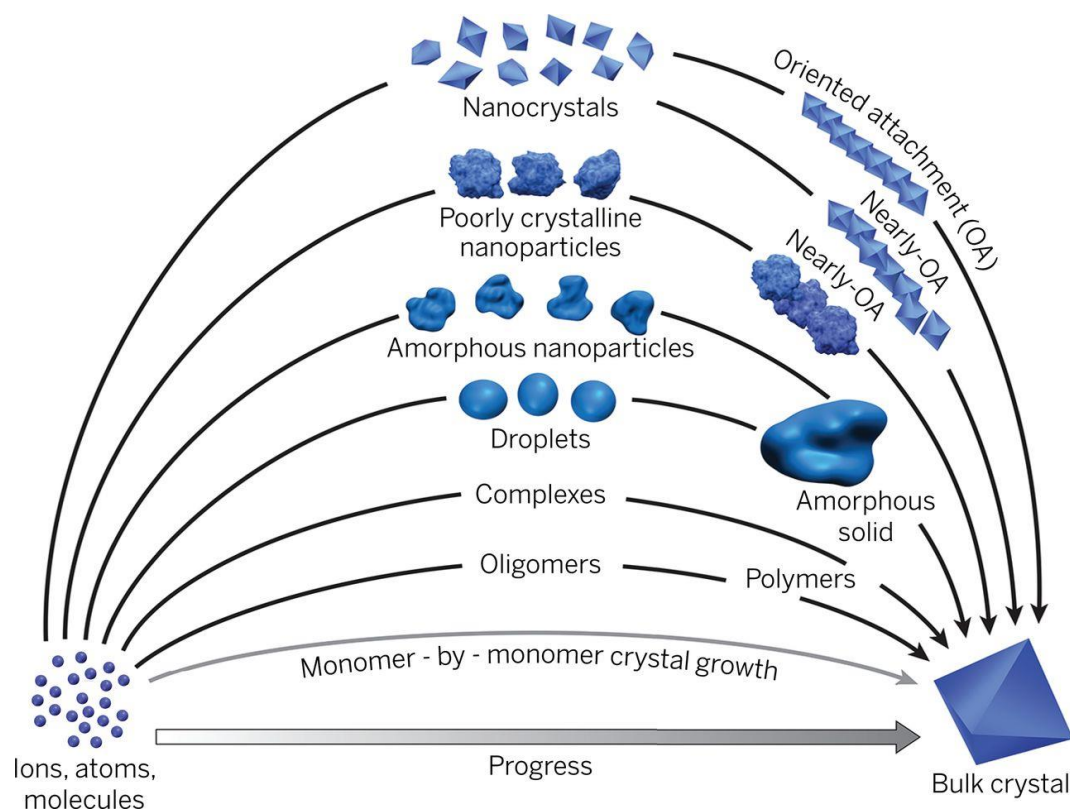
Figure 7. Pathways to crystallization by particle attachment. From J. J. De Yoreo *et al.* (Science, 349, aaa6760, 2015). Reprinted with permission from AAAS.[14]

The observation of multistep crystallization pathways opens up new opportunities to rethink crystallization processes. For instance, the formation pathway via metastable clusters may lower the nucleation barrier. The stabilization of pre-nucleation structures, however, could slow down the crystallization or even create barriers to prevent crystallization processes completely.[111] **Figure 7** presents an overview of many possible pathways of crystallization via general particle attachment. This diversity highlights the complexity of the topic and that it is not possible to just create a "one-fits-all" approach of crystallization.[111] It is instead needed to investigate further and understand the regarded system in detail to develop guidelines that help to provide suitable predictions to implement customized material requirements in the future.

c. State of the Art Precursor Chemistry of PSCs

As commonly applied manufacturing processes of PSCs are solvent-based, fundamental principles of the presented nucleation theories should be applicable for the perovskite crystallization. For this reason, it is a topic that is to date constantly under investigation and of great interest in the research community. In recent years, the interest in precursor solutions has increased enormously. At present, high PSC efficiencies are reachable, and further development going beyond becomes a question of fine-tuning, which requires fundamental knowledge of the crystallization process. Recent studies that support the classification of this work are highlighted in the following.

In 2018 K. H. Stone *et al.* investigated the functionality of adding lead chloride ($PbCl_2$) to the precursor solution of $MAPbI_3$ since it has been used to improve the intrinsic crystal quality. They uncovered the formation of intermediate solid NPs of MA_2PbI_3Cl in the solution coexisting with methylammonium chloride (MACl) retarding the actual crystallization of $MAPbI_3$.[15] The evaporation of MACl thereby self-regulates the growth process.[15] Other additives such as methylammonium thiocyanate (MASCN) tend to cause lower nucleation density and larger nuclei sizes.[16] Using MASCN as an additive thus supports the formation of a polycrystalline thin film with large grain formation and homogeneous surface coverage. As addressed in section 2.1 c, alkaline cations represent common additives improving perovskite performance, film quality and stability.[17,18] In mixed lead halide PSCs, (A-site cation shared by FA^+ and MA^+, X-site shared by Br^- and I^-), degradation might result in the formation of MAI- and FABr-rich phases. However, the systematic addition of Cs^+ or Rb^+ can alter the crystallization process to suppress this phase segregation and thus promotes the formation of a phase-pure thin film.[122]

The general growth process of the perovskite thin film was investigated by S. Chen *et al.* in 2021 using grazing incidence X-ray diffraction technique (GIXRD).[47] The polycrystalline film undergoes a top-to-bottom downward growth towards the substrate initiated by solvent evaporation.[47] This understanding provides valuable information for the targeted production of PSC since the presented growth behavior is only marginally affected by the composition of the perovskites and the wettability of the underlying substrates. In September 2021, the group led by P. Müller-Buschbaum correlated the

solution-based spin-coating fabrication mechanism of perovskite thin films with four stages of perovskite formation.
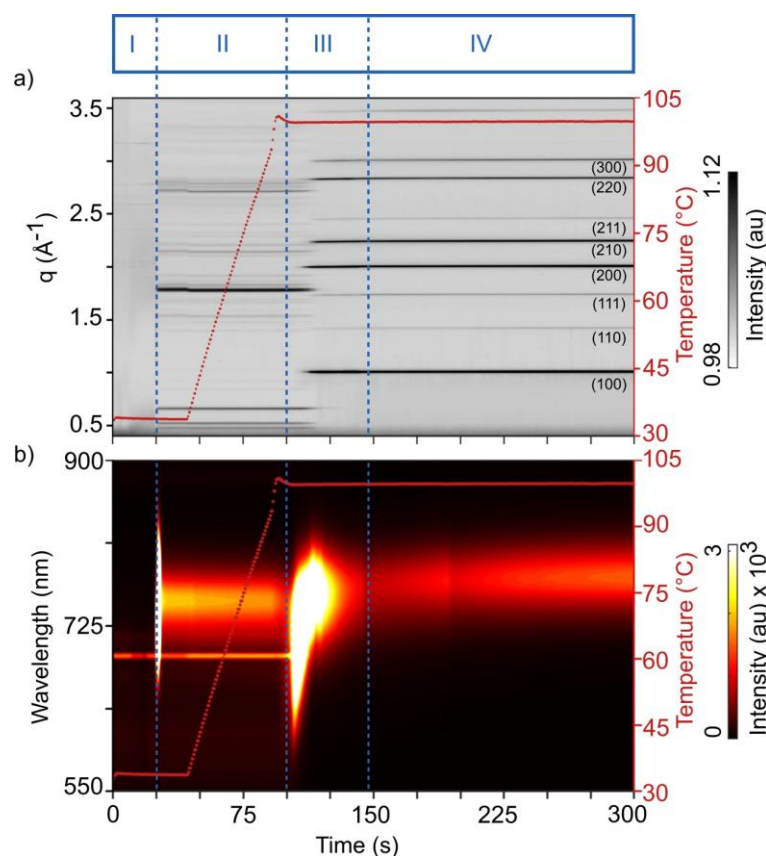
Figure 8. Time dependence of the four phases of the colloidal conversion process of the perovskite precursor to the final MAPbI$_3$ perovskite thin film. a) GIWAXS data as a function of the scattering vector q and b) PL data as a function of wavelength. (The emission line at 690 nm is related to the diffuse reflection of the laser used in the position alignment system of the beamline.) The substrate temperature is presented on the right y-axis. Anti-solvent drop at t=25 s. In phase II, the diffraction can be assigned to Pb$_3$I$_8$.2(CH$_3$)$_2$SO.2CH$_3$NH$_3$ (MAPbI$_3$·DMSO), a solvent-complex phase, converted into MAPbI$_3$ in phase III during annealing. From S. Pratap *et al.* (Nat Commun, 12, 5624, 2021) reprinted with permission from Springer Nature.[123]

As presented in **Figure 8**, the synchrotron-based in-situ grazing incidence wide-angle X-ray scattering (GIWAXS) data combined with optical photoluminescence (PL) measurements reveal the final perovskite formation of MAPbI$_3$. The data allow the elaboration of the following stages towards crystallization: I) instant nucleation of polydisperse MAPbI$_3$ NPs with an anti-solvent drop, II) instantaneous partial conversion of metastable NPs into an orthorhombic solvent-complex by coalescence, III) thermal decomposition (dissolution) of the stable solvent-complex into iodidoplumbate subunits upon evaporation of solvent from the complex and IV) formation (recrystallization) of cubic MAPbI$_3$ crystals in a thin film.[123] Following the proposed mechanism for MAPbI$_3$,

some parallels appear to the proposed crystallization pathways of the non-classical nucleation theory (**Figure 7**).

Although the research about morphology improvement of perovskite thin films advances, lead halide perovskites do not seem to struggle as much as their lead-free alternatives with poor coverage and the evolution of pinholes. Thus, studying the crystallization mechanism can be of particular interest for lead-free PSCs, considering their poor morphology (i.e. low coverage and formation of pinholes) originated from its rapid crystallization process. Dimethyl sulfoxide (DMSO) is still one of the most promising solvents used for efficient tin-based PSCs, focusing on solvent properties.[124–126] One reason for the focus on this particular solvent possibly lies in the fact that it is the solvent with the best-understood working behavior for lead-based perovskites, including the formation of an intermediate phase decelerating the crystallization.[11,127–129] Taking into account the difficulty of the reported too rapid crystallization of tin perovskites, the use of this solvent seems, therefore, inevitable. Nevertheless, even when using DMSO as a solvent for the solution-based processing of tin-based thin films, efforts have been made to control and to enhance the crystalline morphology either by using additives or solvent engineering.[19,130,131] Yet, a dead-end might be approached following this strategy knowing about the ability of DMSO to oxidize the Sn(II) from the perovskite.[132]

The precursor holds the key in controlling the crystallization kinetics and looking for suitable solvents for a successful perovskite processing. Methodology like small-angle X-ray scattering (SAXS) or in-situ GIWAXS can reveal insights into the physicochemical properties of the precursor solution in dependence on the solvent.[133]
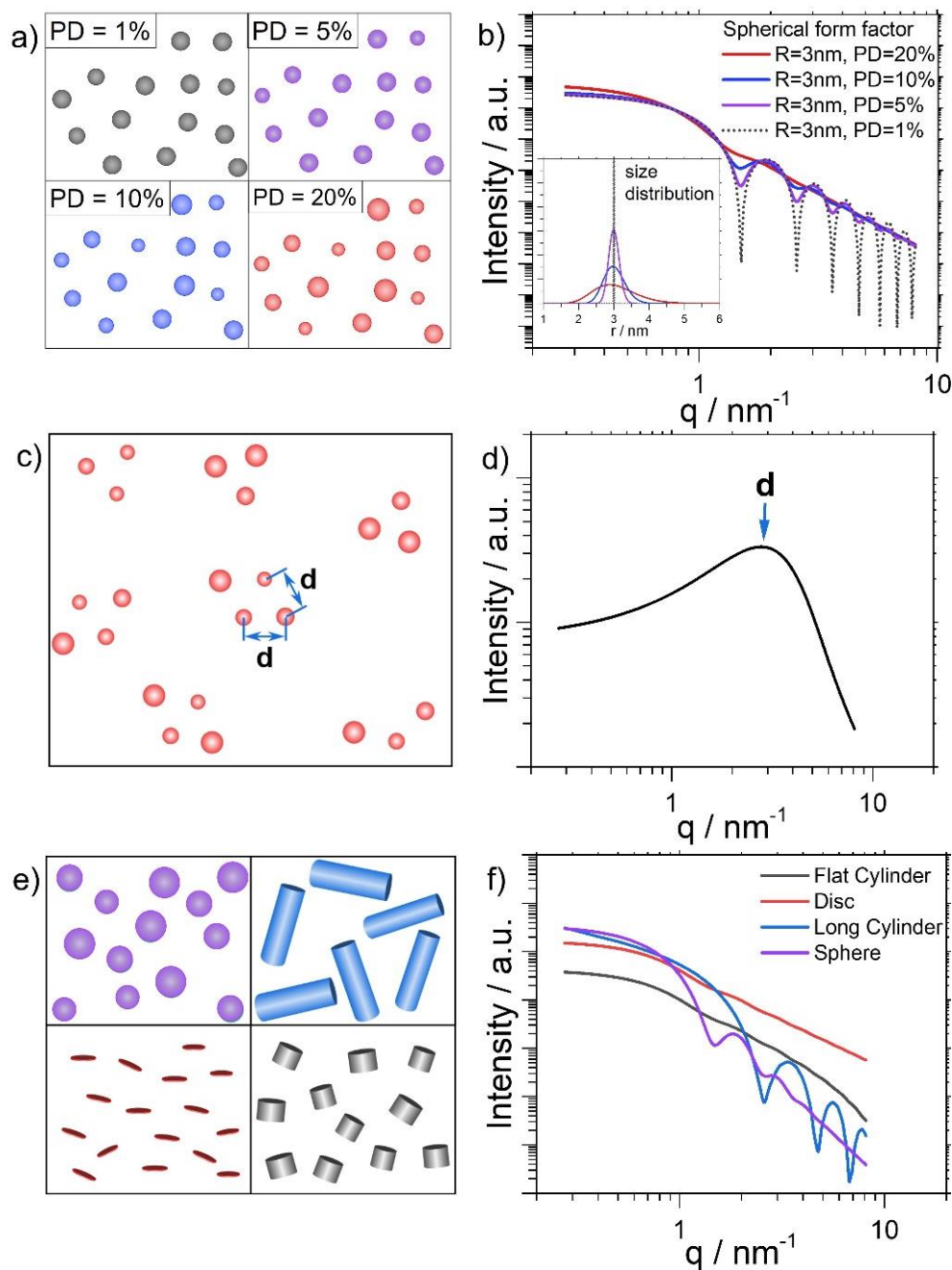
2.3 Small-Angle Scattering

SAS is a well-known technique for structural analysis of the condensed matter. It is particularly suitable for investigating structural details with characteristic dimensions at length scales above interatomic distances up to 100 nm and beyond. SAS covers mainly three analytical techniques: small-angle neutron (SANS), X-ray (SAXS) and light (SALS, or just LS) scattering. All of these methodologies are based on the elastic scattering of monochromatic radiation from a sample. The final scattering pattern provides information about the size and shape (form factor) and structure/orientation of disordered or partially ordered systems in the sample (structure factor). In this section, the primary and most relevant concepts of SAXS and SANS are described since these methods are employed in all three publications that emerged from the here presented thesis. However, the following content will by no means cover all the theoretical details and background. Instead, it aims to give a broad overview of the perovskite precursor solutions' main technical features and applications. For further insights, more advanced readers are encouraged to look into SAS in the related literature.[134–137]

a. Data Processing SAXS/SANS

The predominantly random orientation of scattering objects in solution results in an averaged scattering curve. This circumstance results in the possibility of collecting only one-dimensional information about an actual three-dimensional structure. One of the resulting challenges of SAS is to derive the three-dimensional structure information from these one-dimensional scattering curves from the experiment.[138]

Postulating of structural models (covering form and structure factors) and fitting their variable parameters to reproduce the sample scattering curve is a standard method to interpret the obtained small-angle scattering data. **Figure 9** depicts different typical structure models: spheres with various size-distribution (a), clustered spheres with a specific recurrent distance (c), and a comparison of other form factors: spheres, long cylinders, discs, and flat cylinders (e).

Figure 9. Diversity of structural information available from a one-dimensional scattering curve. (a) Model structures of spherical particles with different polydispersities ranging from 1 % to 20 %, (b) their corresponding calculated small-angle scattering curves and their corresponding size distributions in the inset. c) Model structure of clustered spherical particles with a recurrent distance d and d) the corresponding calculated scattering curve. e) Model structures with different form factors and f) their corresponding calculated scattering pattern.

The corresponding calculated scattering curves of these structure models are shown in

Figure 9b, d, f. As presented within the structure models, various parameters affect the

scattering curves distinctively and distinguishable such as the particle size, size

distribution, particle-particle interaction and particle shape.

The scattering intensity as a function of q, I(q) can be described by the following equation:

$$I(q) = N_P \int \{\Delta\rho V_P(r) \, P(q,r)\}^2 \, S(q,r) \, N(r) \, dr$$

N_P: number of particles
$\Delta\rho$:   scattering length density difference ($\Delta\rho = \rho_{particle} - \rho_{matrix}$)
$P(q,r)$: form factor
$S(q,r)$: inter-particle interference (structure factor)
$N(r)$:   size distribution

Monodisperse spheres of radius *r* generate a scattering curve with interference fringes, following a Bessel function. Increasing the polydispersity, broadening of particle size distribution dampens the interferences fringes and leads to more indistinct scattering curves (**Figure 9a, b**). The general shape of the scattering curve, however, remains. A simulation of partially ordered spherical particles (**Figure 9c**) with a recurrent distance *d* results in a scattering curve as depicted in **Figure 9d**. This curve shape provides the information about clustering and the inter-particle interaction of the scattering objects under investigation. The polydisperse spheres gather in small groups of several spheres with an average distance *d* to form superstructures. This superstructure leads to the development of a peak maximum that dominates the corresponding scattering curve. The blue arrow indicates this peak position at q = 2π/*d*. This relationship allows us to calculate the inter-particle distance *d* as discussed by V. S. Raghuwanshi *et al.*[139]. Furthermore, nanoscale particles and nanostructures can exist in many shapes, as presented in **Figure 9e**. These shapes, described by form factors, result in distinct scattering curves characteristic of the respective shape, depicted in **Figure 9f**. The one-dimensional scattering curves thus make it possible to distinguish between the shapes of nanostructures.

All SAS curves analyzed within this thesis were fitted with the program SASfit[140]. The particular structure model including a specific form factor and a hard-sphere structure factor chosen to fit the scattering curves is explained in further detail in the experimental section of the respective chapter.

b. Scattering Interaction with Matter

Although the identical SANS and SAXS data methods can be used to extract structural information, there are crucial differences in how X-ray photons and Neutrons are produced and interact with the scattering object under investigation.[141] For X-ray photons, the scattering arises from the electrons of the sample whereas neutrons interact with the system's nucleus. One necessary measure to quantify the different scattering properties of a sample is the scattering length densities (SLD).[133]
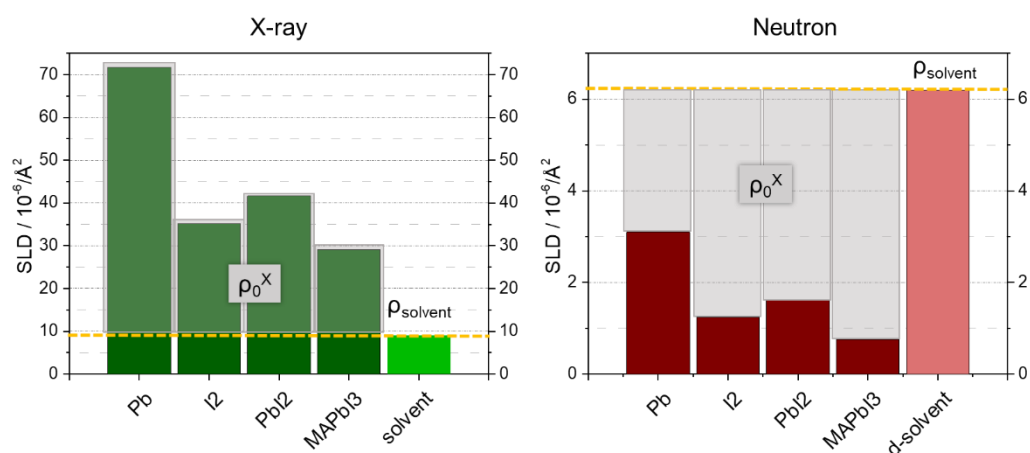
Figure 10. Contrast differences between neutron and X-rays. Calculated SLDs of possible objects present in solution compared to the SLD of the solvent $\rho_{solvent}$ for X-ray interaction in green and neutron interaction in red. Shaded in grey the SLD contrast ρ_0^x, i.e. the SLD difference between the scattering object X and the solvent (NIST).

Depending on the interaction, the SLD of a scattered object differs. **Figure 10** shows the SLDs of different known systems that are comparable with dissolved compounds of a perovskite precursor solution, such as MAPbI₃. Still, the structural information about the colloidal solution is not sufficient to absolutely calculate the SLD of the scattering objects expected. Regarding the equation for the measured intensity I(q) in SAS, it becomes evident that it matches the SLD difference $\Delta\rho$ ($\Delta\rho = \rho_{particle} - \rho_{matrix}$). Hence, in **Figure 10** the calculated SLDs of the scattering objects can be compared to the SLD of the matrix, represented by the solvent mixture. The solvent data depicted in **Figure 10** correspond to a *N,N*-dimethylformamide (DMF) and DMSO solvent mixture in a ratio 6:1 (v/v) or deuterated, d-DMF:d-DMSO (6:1), in case of neutron scattering.

Comparing the SLDs of specific elements like Pb in neutron and X-ray scattering highlights the differences in contrast. Thus, features in the scattering curve caused by the form or structure are expected to be more pronounced in the case of X-rays. One

reason for that behavior might be based on the significant higher $\Delta\rho$ that is shown for X-rays compared to neutron. A further relevant impact on the resulting scattering data consists of the origin of the respective radiation source. In terms of a synchrotron X-ray source, the beam is highly collimated, monochromatic with a wavelength smearing of about 2 x 10^{-4}.

However, the wavelength smearing ranges about 10.5 % in the case of neutrons, which can be observed in smearing effects in the derived 1D curve.[142] The interaction of neutrons with matter is weak, corresponding to only negligible absorption. Therefore, the resulting penetration depth of neutrons allows the probe of bulk properties of comparably thick samples. It is easier to penetrate a large sample volume with neutron scattering, particularly considering the high absorption of perovskite precursor solutions. Hence, a significantly larger sample volume was probed in neutron scattering compared to the thin capillaries required to perform successful SAXS experiments. By carrying out SANS measurements before performing SAXS, we can exclude multiple scattering effects when using X-rays.

c.   The Interplay of Multiple Techniques

SAS data needs to be supported by further analytical techniques to provide a more complete picture about the chemical nature of the perovskite precursor solutions. Since SAS mainly covers the nanoscale dimensions, additional methods deliver further insights about the interatomic level and information of superordinate structures.
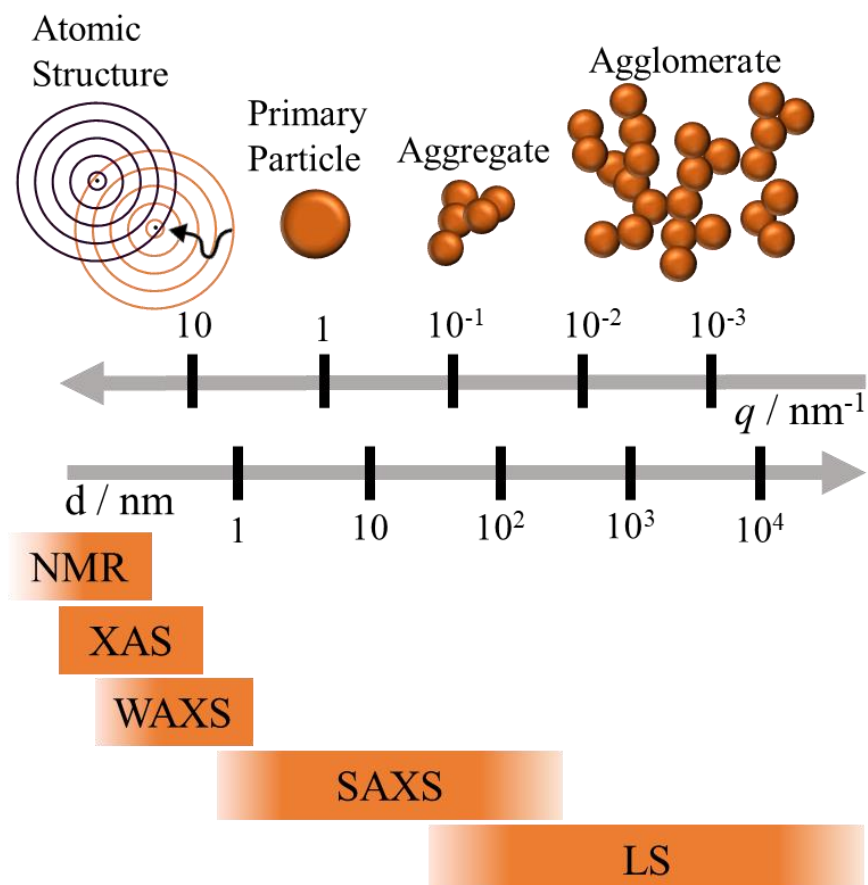
Figure 11. The interplay of different characterization techniques concerning the size of the scattering objects. As used throughout this thesis. The size is given in real (d / nm) and reciprocal space (q / nm^{-1}) to illustrate their correlation.

Therefore, other techniques, such as nuclear magnetic resonance spectroscopy (NMR), X-ray absorption spectroscopy (XAS), wide-angle X-ray scattering (WAXS) and light scattering (LS) are complementing the previously introduced SAS experiments (**Figure 11**) throughout the results of the thesis.

3 Small-Angle Scattering revealing Halide Perovskite Precursors

The presented chapter is based on a manuscript that has been published under the title "Small-Angle Scattering to Reveal the Colloidal Nature of Halide Perovskite Precursor Solution" by **Marion A. Flatken**, Armin Hoell, Robert Wendt, Eneli Härk, André Dallmann, Albert Prause, Jorge Pascual, Eva Unger and Antonio Abate in Journal of Materials Chemistry A 2021, 9, 13477.
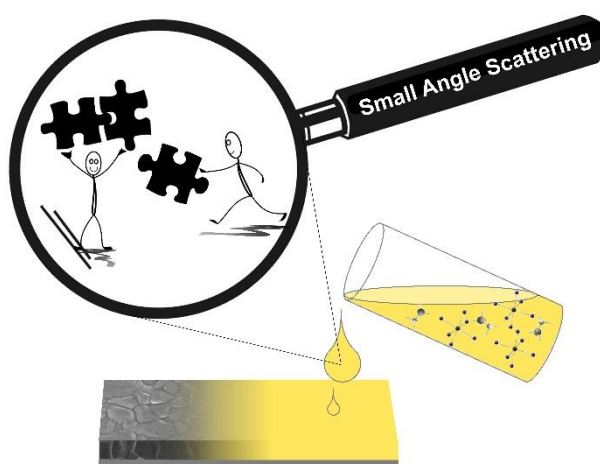
Figure 12. Graphical abstract for the publication by M. A. Flatken et al. „Small-Angle Scattering to Reveal the Colloidal Nature of Halide Perovskite Precursor Solution". Published on the webpage of Helmholtz-Zentrum Berlin (HZB) in the section *Science Highlight*.

M. A. Flatken conceptualized and investigated the presented research question, performed the SAXS measurements and took care of the data evaluation and interpretation and the evaluation and analysis of NMR data. She was responsible for the general project administration and wrote the original draft. R. Wendt supported SAXS data evaluation and interpretation. J. Pascual assisted in writing the original draft. E. Härk helped to record the SANS data as a beamline scientist of the V4 beamline at BERII. A. Dallmann was responsible for recording the NMR spectroscopy data. A. Prause performed and evaluated the DLS data. E. Unger supported the writing process by reviewing and editing. A. Hoell is in charge of the ASAXS instrument from HZB used. He supervised and reviewed the manuscript. A. Abate supervised, provided the resources, reviewed and edited the manuscript before submission.

3.1 Introduction

In recent years, the efficiency of perovskite solar cells (PSCs) has increased in record speed. Due to its outstanding properties, metal halide perovskites are considered to be the future in the photovoltaic (PV) industry and find applications as light-emitting diodes, nanowire lasers or photo-detectors.[39,143,144] Besides their excellent PV properties, the low temperature, solution-based perovskite fabrication procedure is another criterion that is particularly well suited for fast and cost-efficient manufacturing.[38,39] The absorber material, perovskite, is not sufficiently understood to control the device efficiency systematically or to explain and selectively influence observed PV properties. One approach to gain further knowledge that has received considerable attention is to study the chemical organization in the precursor solution used to synthesize the perovskite thin film.[8,145] As the crystalline thin film is growing directly from solution, a detailed understanding of the crystallization mechanism is critical to enable control of the perovskite formation. In this regard, the colloidal chemistry of perovskite precursor solutions contributes significantly to the crystallization process and thus to the perovskite morphology, which is known to impact the performance of PSCs directly.[8,12,146] In a theoretical study, E. Radicchi *et al.*[147] present the iodidoplumbate complexes $[PbI_mX_n]^{2-m}$ that can be expected in particular solvents, being X *N,N*-dimethylformamide (DMF) and dimethyl sulfoxide (DMSO). The role of solvents and coordination chemistry of the central atom Pb is critical in solution chemistry for perovskite precursors.[15,145,147] Weakly coordinating solvents tend to favour faster crystallization. In contrast, stronger coordinating solvents like DMSO form an intermediate state, which leads to a slower crystallization process and thus a better film morphology.[11,148] However, though trends are observable and the resulting film properties are characterized in detail, the actual solution chemistry, including the specific structure of the colloidal particles and a mechanism to explain the fast, low-temperature crystallization, remains unclear.[149]

Methods preferably used for solution characterization, like dynamic light scattering (DLS), UV-vis spectroscopy or cryogenic transmission electron microscopy (cryo-TEM), should be used with caution, as often the nature of the regarded system slightly differs, or crucial properties are only indirectly determined.[8,12,150–152] Considering the origin of biochemical solutions (e.g. micelle formation), DLS is particularly suitable to

detect larger nanostructures in the range of 5 nm to 1000 nm. It measures fluctuations, which can be related to Brownian diffusivity of particles and not directly their size. Though one can then calculate the particle size, this implies making assumptions that are not suitable for every colloidal system.[153] Thus, it occurs that derived particle sizes from a microscopy technique (e.g. TEM) differ from the calculated distributions derived by DLS. Whereas J. Kim *et al.* refer to colloidal sizes in the range of 100 nm based on DLS studies,[8,154] the first study using cryo-TEM reveals insights on the size of colloidal structures found in the perovskite precursor solutions, which are in the range of 1 nm.[150] Still, it remains unclear what effect the cryo shock freezing has on the colloid chemistry in solution.[155] Unfortunately, also the colloidal interactions in liquid are not considered. UV-vis spectroscopy is frequently used to identify characteristic absorption spectra, which can determine possible species in solution.[12,145] However, it is challenging to apply this method to solution concentrations above 1 mol L^{-1} typically used for thin film deposition in solar cell fabrication.[8] Considering that a solution-based deposition process fabricates most of the PSCs, it is essential to characterize the solution properties in their nature, close to the application.

Herein, we apply small-angle scattering using synchrotron radiation (SAXS) and neutrons (SANS) to characterize the perovskite precursor solution on a nanostructural level. We observe well-structured colloidal nanoparticles (NPs) in solution, interacting and forming a dynamic arrangement. We demonstrate that this method can be applied directly to the precursor solution used for processing PSCs without the need for further adjustments.

3.3 Experimental Details

Sample Preparation

All chemicals used were of analytical grade and were used as received without any further purification. The perovskite solution is mixed from 1.3 mol L^{-1} of PbI$_2$ (Tokyo Chemical Industry, > 98 %) and CH$_3$NH$_3$I (Dyenamo, > 99.99 %) in mixed solvent (DMF:DMSO (Sigma-Aldrich) prepared by volume/volume (v/v) ratio of 6:1). For the neutron scattering and NMR experiments deuterated solvents DMF-d7 and DMSO-d6 (Sigma-Aldrich, >= 99.5 atom %) are used. The resulting perovskite solution is shaken at 60 °C for 5 min to dissolve all components. The perovskite solution is then diluted with the solvent mixture (DMF: DMSO 6:1, v/v) to reach the desired concentration (0.4, 0.6, 0.8, 1.0, 1.1 and 1.2 mol L^{-1}).

Nuclear Magnetic Resonance Spectroscopy, ^{207}Pb NMR

The spectra were acquired on a Bruker AVII 400 MHz or Bruker AVIII 500 MHz equipped with room temperature TBO or BBO-probe heads respectively. Typically, a sweep width of 897 ppm was used, and 8192 points were acquired, resulting in a total acquisition time of 54.48 ms. The center frequency had to be adjusted from sample to sample in order to detect the desired signal. Therefore, a full scan of the possible shift range was acquired on new samples until the peak was detected. We used a 30° pulse to minimize the recycle delay to 200 ms (for samples with broad peaks, acquisition time and recycle delay were adjusted down to 50 ms). The number of scans thus ranged from 512 for very concentrated samples (~1 mol L^{-1}) to 132k scans for very dilute samples with broad peaks (0.1 mol L^{-1}). All other spectra were measured with standardized parameter sets from Bruker Topspin version 2.1 (AV400) and 3.0 (AV500).

Dynamic Light Scattering, DLS

Dynamic light scattering (DLS) measurements were carried out with a 3DSpectrometer (LSinstruments, Switzerland). The setup uses a He-Ne laser with a wavelength of 632.8 nm and a goniometer to set the scattering angle 2θ between 15 ° and 145 °. The samples were measured from 20 ° to 135 ° in 5 ° steps with 30 s for each measurement.

The temperature was set to 25 °C. Analysis of the obtained intensity correlation data represented as $g^{(2)}(\tau) - 1$, was performed with self-written python-based software. The intensity correlation function $g^{(2)}(\tau)$ is related to the field correlation function via the Siegert relation $g^{(2)}(\tau) = 1 + \beta \left(g^{(1)}(\tau) \right)^2$. The data were fitted with a bimodal exponential model, see the following equation.

$$g^{(2)}(\tau) - 1 = \beta(a_1 e^{-\Gamma_1 \tau} + a_2 e^{-\Gamma_2 \tau})^2 \text{ with } a_2 = 1 - a_1$$

where β is the instrument-specific coherence factor, τ the correlation time, and a_i and Γ_i the amplitude and decay rate for the corresponding species I, respectively. The collective diffusion coefficient D_{coll} was deterimined by a linear fit of Γ versus q^2, where q is the scattering vector magnitude. From this fit, D_{coll} results from the slope according to $\Gamma = D \cdot q^2$. The hydrodynamic radius was finally calculated via the Stokes-Einstein equation, $R_h = \frac{k_B T}{6\pi\eta D}$, where k_B is the Boltzmann constant, T the absolute temperature and η the viscosity of the solvent.

The perovskite precursor solution was measured previously filtered with a PTFE membrane filter with a pore size of 0.22 μm as well as unfiltered.

Small-Angle Neutron Scattering, SANS

SANS measurements were performed at the V4 beamline at the BERII reactor, HZB in Berlin[156]. The detector distance was 1 m with using a wavelength of 4.5 Å. Hence, a *q*-range of approx. 0.5 nm^{-1} to 8 nm^{-1} was covered (0.78 nm - 12.6 nm). The perovskite solutions for SANS measurements were measured inside quartz cuvettes Hellma® cuvette (Hellma Analytics, Germany) with a 1 mm optical path length. The quartz cuvettes filled with the perovskite solution were sealed with polytetrafluoroethylene (PTFE) caps and Parafilm® M to inhibit the evaporation of deuterated solvent from the sample and to prevent the adsorption of moisture from the outside environment. Each sample was measured with a temperature control at 20, 22, 24, 26 and 60 °C and finally again at 20 °C. An "Ultra-Cryomat" from Lauda was used to set and hold the temperature during the measurements. An aperture with a diameter of 13 mm was used in front of any cuvette filled with the perovskite solution. Scattering contribution from mixed solvent DMF-d7 and DMSO-d6 solution was measured separately. At each

temperature, the SANS curves of each sample were recorded every 5 min, followed by a 20 s transmission scan. Of these, four repetitions were performed to increase the statistics for each condition. As shown in **Figure S3.1**, the measured SANS curves (run 1 to 4) are in good agreement, coincide and are reproducible. Therefore, the four runs were merged for each condition respectively to achieve better statistics. The measured SANS patterns overlap, and no change in the measured transmission can be observed, which gives rise to the assumption that we do not observe any change in solution.

Data reduction and radial averaging: For data reduction and for the radial averaging to the 1D scattering SANS pattern, the BerSANS software was used[157]. Normalization and background subtraction routines were performed employing the scattering data from standard H_2O-filled cuvette, empty cuvette, and beam stopped with cadmium plate, respectively. Respective transmission values for each sample were taken into account. For 5 minutes scattering runs were merged to achieve better statistics.

Small-Angle X-ray Scattering

The reported SAXS data were measured using synchrotron radiation at the four crystal monochromator beamline in the laboratory of PTB (Physikalisch-Technische Bundesanstalt) at BESSYII[158]. The SAXS instrument of Helmholtz-Zentrum Berlin (HZB) contains an adjustable about 3,5 m long support structure with a long edge-welded bellow system to allow the possibility to vary the sample to detector distance without breaking the vacuum[159]. The two-dimensional scattering images were collected by a windowless Dectris 1M PILATUS2 in-vacuum hybrid-pixel detector. The measurements were carried out at two different distances (0.8 m and 3.7 m) at photon energies of 10 keV and 8 keV, respectively. Thus, a *q*-range from 0.05 nm^{-1} to 8.5 nm^{-1} was covered. For a sample-sensitive measurement, the solutions were measured with an exposure time of 600 s with two repetitions for the shorter distance and three for the long distance to achieve good quality data and to monitor unwanted but possible changes of the specimen over time (which can therefore be safely excluded, see **Figure S3.2**). Due to the low transmittance of the lead-containing precursor solutions, especially thin (0.1 mm), rectangular borosilicate cuvettes (with a wall thickness of 0.1 mm) purchased from CM Scientific (UK) were used.

By constraining the beam with a low-scatter pinhole of germanium 500 μm in diameter, the total flux on the sample could be determined for each energy. Accordingly, for the long distance (3.7 m) where 8 keV was used, we can indicate $4.8 * 10^9$ photons/s and $2.6 * 10^9$ photons/s for the short distance (0.8 m) where 10 keV was used.

Table 1. Technical parameters of the SAXS measurement. Transmission of measured samples, a sample to detector distance, energy and acquisition time.

Sample Name: Concentration / mol L^{-1}	Transmission	Sample to detector distance / m	Energy / eV	Acquisition Time / s
empty beam	1.000	3.750	8000	600
empty capillary	0.228	3.750	8000	600
0.4	0.113	3.750	8000	600
0.6	0.079	3.750	8000	600
0.8	0.058	3.750	8000	600
1.0	0.044	3.750	8000	600
1.2	0.033	3.750	8000	600
empty beam	1.000	0.810	10000	600
empty capillary	0.463	0.810	10000	600
0.4	0.315	0.810	10000	600
0.6	0.258	0.810	10000	600
0.8	0.219	0.810	10000	600
1.0	0.187	0.810	10000	600
1.2	0.160	0.810	10000	600

Data processing: For data reduction and radial averaging to the 1D scattering pattern, the BerSAS software was used, a modified version applicable for SAXS and SANS of the BerSANS software[157].

All SAXS curves of the investigated samples were fitted with the program SASfit[140]. A structure model with a cylindrical form factor and a hard-sphere structure factor was chosen to fit all sample scattering curves.

The choice of a cylindrical form factor was motivated by the assumption of having "distorted" Pb-I-solvent complexes with approximately cylindrical geometry in the precursor solution. Furthermore, the cylindrical form factor leads to the best fit compared to other geometrical objects tried in the fitting procedure. The underlying equations of the applied Porod's approximation for a long cylinder can be found elsewhere.[160,161] In SASfit, the width parameter *s* of the distribution function used (lognormal) is directly related to the polydispersity of the system.
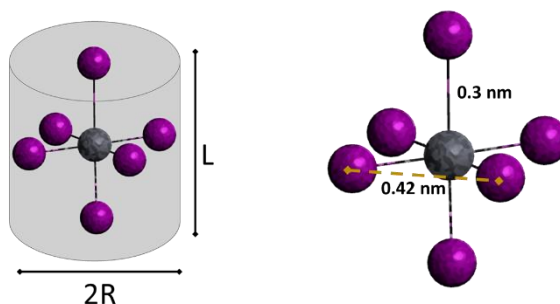
Figure 13. 6-fold coordinated iodidoplumbate formation. Expected distances in an iodidoplumbate assuming 90° I-Pb-I angle.

Using the cylindrical form factor, this parameter is 0.045 for 1.2 mol L^{-1} and 0.097 for the concentration of 0.4 mol L^{-1}. A scheme of the assumed bond length dimensions resulting in the choice of the cylindrical form factor are presented in **Figure 13**.

The herein investigated particles were considered as hard spheres. Thereby, these particles are assumed as incompressible resulting in fixed radii for each particle and an infinite repulsive force at a specific interparticular separation. The hard spheres model neglects attractive forces but describes various colloids in organic solvents fairly well.[162–164] However, we used the monodisperse Percus-Yevick approximation for hard spheres to fit the interaction of the analyzed colloidal particles.[165,166]

3.4 Results & Discussion

Earlier recorded DLS data (**Figure S3.3**, **Table S3.1.**, 9.1) indicate that large higher-level structures in the micrometer range are present in a perovskite precursor solution (1 mol L^{-1}). In addition, small sizes in the order of nanometers have been detected. By combining DLS with diffusion ordered spectroscopy (DOSY), we can prove that these can be assigned to the solute and cannot be traced back to the solvent itself (**Figure S3.4**, 9.1). To better understand these sub-nanometer scale particles and simultaneously explain the occurrence of the large sizes, we decided to use SAXS and SANS for further characterization.
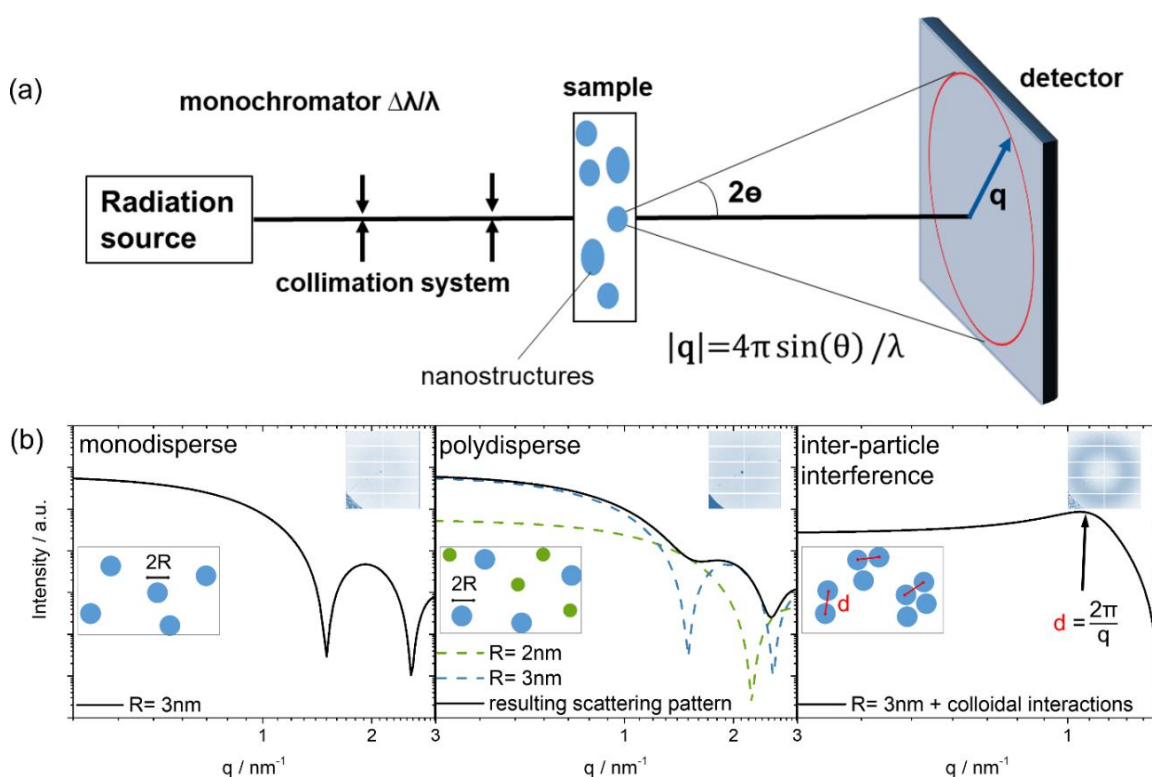
Figure 14. SAS technique. (a) The basic scheme of a SAS instrument. (b) Series of theoretically modelled 1D scattering curves derived by radial averaging of a 2D-detector image as shown in the top right corner of each plot.

SAS is a characterization technique to determine the structure of nanometer-sized particles, distances, and arrangements in a material system.[134,138,167] A scheme of the general SAS technique is provided in **Figure 14**. An azimuthal integration of the 2D detector image produces the final 1D scattering pattern. The variations of the resulting scattering pattern give the first indication about changes of size, size distributions, shape and possible arrangement of colloidal particles observed in the sample. Simulated scattering patterns of a typical spherical-shaped form factor for a monodisperse sample

and a polydisperse sample are modelled in **Figure 14b**. The form factor contains the primary information about a nanosized shape, whereas the structure factor describes the inter-particle interaction between the colloidal particles.[134,168] Thus, most simply, for a monodisperse colloidal solution without any particle interaction, the experimentally derived scattering pattern can be expressed as the form factor multiplied by the number of colloids in the beam.

The maximum in a 1D scattering pattern evolves due to the interaction of particles. This trend leads to a dominant structure factor in the scattering pattern, which becomes evident in the formation of a broad peak. In that case, the scattering intensity of the single spheres is reduced to the benefit of an arising peak at $q = 2\pi/d$ as indicated by the black arrow in **Figure 14b**. The mean spacing d between the mass centers of interacting colloidal particles can be calculated (**Figure 14b**, right panel) using the magnitude of q at the peak maximum as discussed by V. S. Raghuwanshi *et al.*[139]

In the current case, we are focusing on the characterization of perovskite precursor solutions, particularly MAPbI$_3$ precursor solutions using a solvent mixture of DMF and DMSO. As it is known from the literature, instability of perovskite devices, and perovskite solutions, is one crucial topic in the research field, which could lead to suspicion of radiation damage.[169,170] At HZB, we were able to use synchrotron radiation at BESSYII and neutrons at BERII to perform SAXS and SANS on perovskite precursor solutions. Using SAXS at BESSYII at X-ray energies of 8 keV and 10 keV ($\pm$ 2 eV), respectively, we cover a broad q-range from 0.05 nm^{-1} to 8.5 nm^{-1} (size range: 209.4 nm - 0.74 nm) to achieve a good overview of particles and size distribution in the perovskite precursor. With SANS, we cover a q-range from 0.5 nm^{-1} to 8.5 nm^{-1} (size range: 12.6 nm - 0.78 nm), measured at the V4 instrument at BERII reactor with a wavelength of 0.45 nm. A critical advantage of the uncharged neutrons is their weak interaction and high penetration depth to probe the bulk of the sample non-destructively.
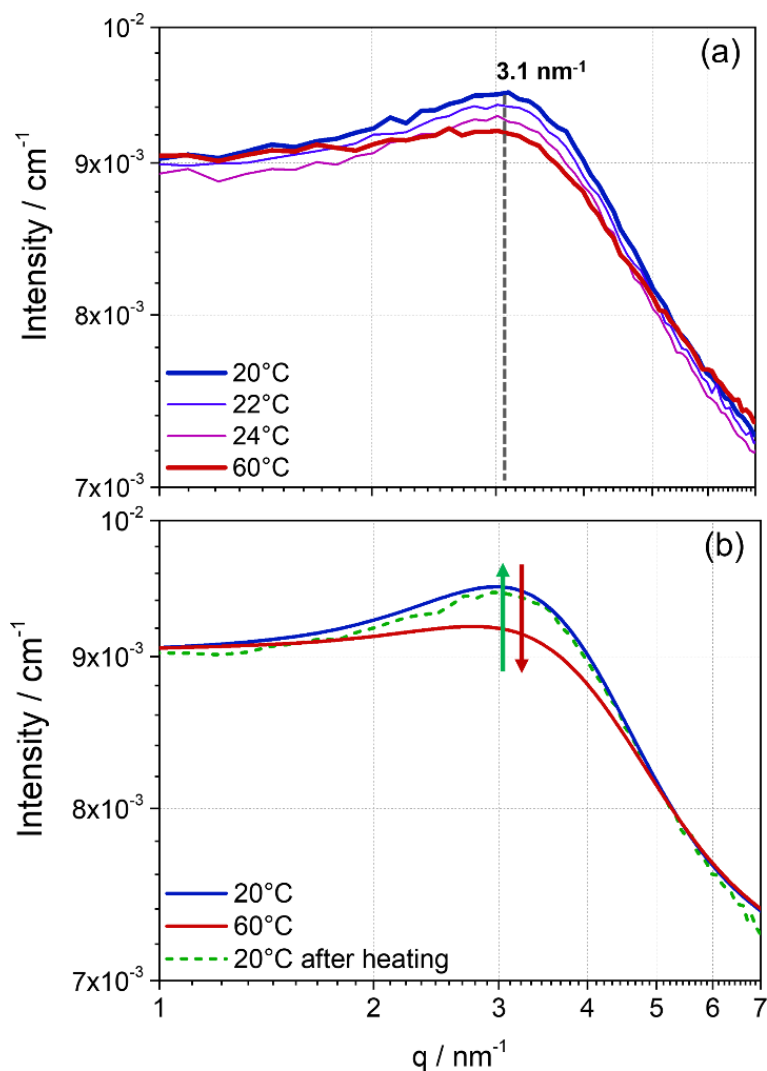
Figure 15. Temperature dependence of a perovskite precursor solution probed with SANS. Scattering pattern of MAPbI$_3$ solution (1.3 mol L^{-1}) measured at different temperatures. (a) Temperature ramping from 20 °C to 24 °C in 2 °C steps and at 60 °C giving a specific recurring distance d at q = 3.1 nm^{-1} and (b) cooling from 60 °C to 20 °C. The reversible temperature effect is indicated by the smoothened scattering data in (b). Here, the green and red arrows illustrate increasing temperature (red) and cooling (green).

The measured scattering intensity is given in the SANS pattern (**Figure 15**) firstly proves the presence of particles in perovskite solution. As the DLS data indicated, the curve of scattering intensity gives rise to assume the existence of two phases in solution, particles and solvent. Additionally, the integrated detector signal in the 1D pattern of the perovskite precursor solution exhibits the features of inter-particle interference (**Figure 14**). An arising broad peak in the SANS pattern reveals that these particles interact, which allows us to suspect that these particles form a dynamic colloidal network explaining the formation of higher-level structures observed in DLS. In the case of the 1.3 mol L^{-1} MAPbI$_3$ precursor solution shown in **Figure 14**, the colloidal arrangement is characterized by a mean spacing *d* between the mass center of the individual particles of

approximately 2 nm (maximum of the peak position at $q = 3.1$ nm^{-1}). This inter-particle short-range order already indicates the first starting points for growth into the long-range ordered crystal. Hence, the strong interaction seems to be a "quasi-crystalline" prearrangement of colloidal particles as an early stage of crystallization.[14,171]

The precursor solution was stepwise heated up to 60 °C (**Figure 15a**) to get further information about the colloidal network. With increasing temperature, an apparent reduction of the maximum intensity is observed. Due to higher mobility caused by rising temperature, the observed network shows fewer inter-colloidal forces, and consequently, the maximum in the measured scattering pattern decreases. Accordingly, the observed effect of the structure factor in the scattering pattern is significantly reducing. Cooling the solution back to room temperature, the maximum is again more pronounced and stays in the same position as before, concluding that the assembly process and breaking the assembles due to external temperature effects is reversible (**Figure 15b**).

In consequence, without further modification, SANS can provide fast and direct information about the colloidal interactions observed in the perovskite precursor solution. Furthermore, the reproducibility of each measurement run proves the non-destructive character of the neutron source. For each temperature and sample, four SANS curves were measured, which were merged to achieve better statistics (**Figure S3.1**, 9.1).

Besides the colloidal interaction in solution, further information about the NP structure itself, which represents the subunits of the colloidal network, can be obtained. In particular, a concentration series of MAPbI$_3$ precursor solutions is analyzed using the SAXS technique in combination with ^{207}Pb NMR, **Figure 16**. Starting from a concentration of 0.4 mol L^{-1} to higher concentrations, the chemical shift in the ^{207}Pb NMR is shifting upfield (**Figure 16a**). The chemical environment of the probed atom (here: Pb) can influence its electron density, i.e. through the polar effect. According to Lenz's law, atoms with higher electron density have higher induced fields, and therefore the nucleus is more shielded. To exclude any electronic effects of the environment, we kept the solvent mixture unchanged (i.e. DMF:DMSO, v/v 6:1).
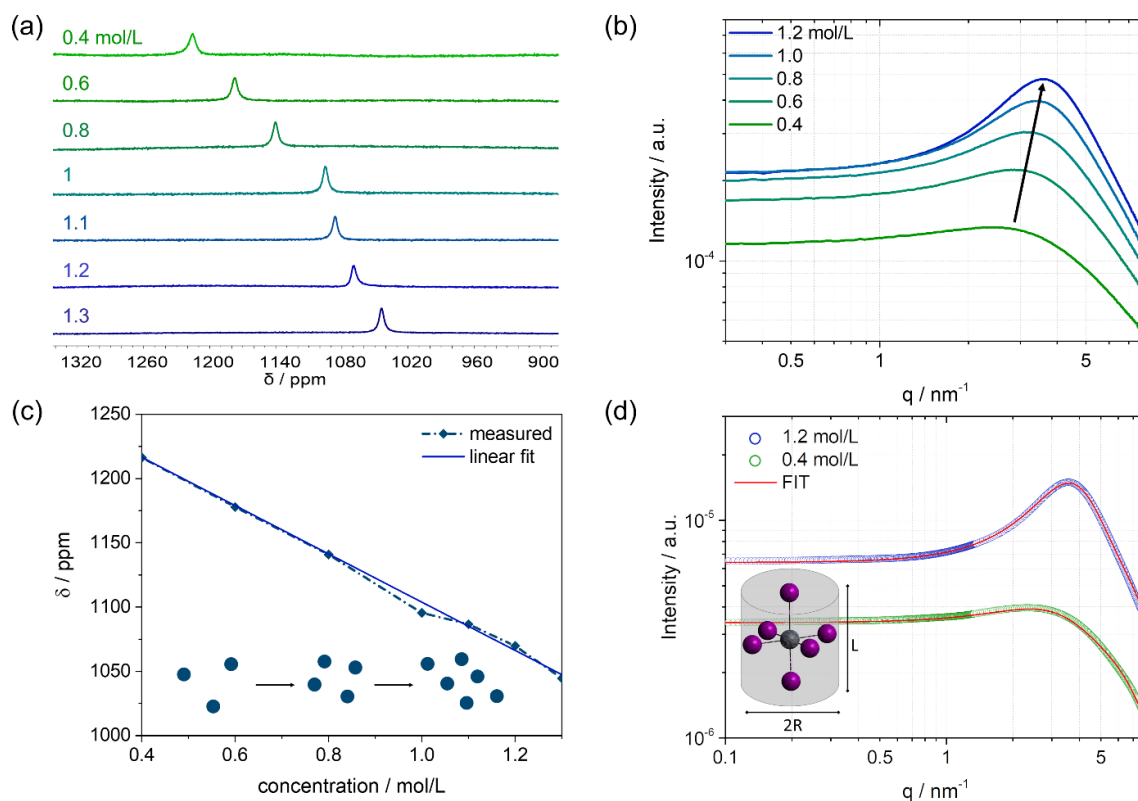
Figure 16. Concentration series of the perovskite precursor solution. (a) ^{207}Pb NMR and (b) SAXS patterns for 0.4 mol L^{-1} to 1.2 mol L^{-1} solutions of MAPbI$_3$ (1.3 mol L^{-1} for NMR). The linear trend is given in (c) combined with a scheme of the colloidal distances that changes with higher concentrations (derived from SAXS data). (d) Two concentrations (0.4 mol L^{-1} and 1.2 mol L^{-1}) were chosen to demonstrate the fitted SAXS data with a suitable form and structure factor using SASfit©.

The electron-donating effect of iodides being direct neighbors to Pb can explain the increase in electron density leading to an upfield shift. We can assume that the more concentrated the precursor solution is, the more iodides will be near the central atom Pb. This scenario can be interpreted to mean that a colloidal network of iodidoplumbates becomes more prominent with increasing concentration, which results in higher shielding of the regarded lead core and thus causes a shift to lower ppm values (**Figure 16a**). The SAXS scattering cross-sections of the precursor solutions show a substantial increase in intensity from 0.4 mol L^{-1} to 1.2 mol L^{-1} (**Figure 16b**). The higher the concentration, the more colloidal particles contribute to the scattering pattern, which leads to an increase in intensity.

Considering the previously explained effects of form and structure factor, the precursor solution with a concentration of 0.4 mol L^{-1} is mainly determined by the form factor that holds the information about the shape and size of the colloidal subunits. Moving towards higher concentration, the influence of the structure factor on the scattering curve, meaning the colloidal interaction, is increasing. In addition, the evolving broad

maximum is shifting significantly with higher concentrations to larger q values, to lower mean d spacing, between the colloidal particles. The trend of the reduced inter-particle distance is depicted in **Figure S3.5**. The lower mean d spacing can be directly related to the tendency of the ^{207}Pb NMR signal towards higher shielding with increasing concentration. **Figure 16c** illustrates the linear dependence of the chemical shift *vs* solution concentration. The blue spheres represent the colloidal particles in solution and schematically describe their increasing interaction with higher concentrations as observed in the respective SAXS pattern. With a more pronounced interaction, higher electron density at the Pb nucleus is observed (upfield shift in NMR). Simultaneously, as the interaction of the colloidal particles become more robust and the distance d between the particles shortens, the density of the electron-donating iodides around the lead increases and becomes apparent by a lower chemical shift (**Figure 16a**, **c**). Combining the information derived from SAXS with ^{207}Pb NMR, the methods complement each other. We can postulate that the observed interacting NPs are indeed subunits of coordinated lead that agglomerate to the extent that it depends on the concentration of the solution.

The software SASfit©[140] was used to extract the structural information from the scattering curves to fit a specific form factor to the measured scattering pattern. The software offers several different models of form factors describing different shapes of colloidal particles. For example, the concentration of 0.4 mol L^{-1} with almost no contribution of the structure factor and 1.2 mol L^{-1} with the most pronounced maximum is discussed further. Under the inclusion of highly valent iodidoplumbates, we hypothesize the presence of octahedral colloidal subspecies stretched due to distortion.[172–174] A cylindrical shape can be taken as an approximation to describe this in a model. Therefore, the form factor for a long cylinder was used, including the input parameters: radius of the cylinder R and length of the cylinder L as given in **Figure 16d**. The best fit, shown in red, was achieved with the input parameters for the form factor using R= 2.5 Å and L= 6.5 Å for 0.4 mol L^{-1} and changing slightly for 1.2 mol L^{-1} to R= 2.5 Å and L= 7.5 Å.

Further, the structure factor in the form of a hard-sphere model was included in the fit. Here, a volume fraction of 0.035 was used to model the 0.4 mol L^{-1}, whereas 1.2 mol L^{-1} showed a significantly higher volume fraction of 0.14. Thereby, the volume fraction is the measure of interacting NPs in the colloidal network.[168] Taking into account an

average atomic distance of 3 Å between the center atom lead and iodide,[175] the values are given by the applied model could fit the proposed high-valent iodidoplumbate formation in solution. Previous work shows that we can expect iodidoplumbates in solution and that the number of iodides surrounding lead should increase with concentration.[145,175,176] Thereby experiments, e.g. UV-vis, mainly were carried out for extremely diluted solutions, based on experimental limitations.[12,145] Thus, generally, only lower valent iodidoplumbates were observed. SAS is now providing new opportunities to probe even moderately and more concentrated solutions to expand the derived knowledge.

Further, including the information of the structure factor, we know of the emergence of strong interactions in the probed solution. We can postulate the presence of large agglomerates, which are formed by a fine arrangement of nanoscale iodidoplumbate subunits. Note that this methodology can equally be applied to other compositions (and different solvents, e.g. for solvent engineering approaches).

As discussed, the relevance of the colloidal network's different characteristics in solution becomes apparent when considering the resulting crystallinity measured with X-ray diffraction of drop cast perovskite films using different concentrations of perovskite precursor solutions (**Figure S3.6**, 9.1).

3.5 Conclusion

To conclude, we demonstrated SAS as an analytical technique to reveal direct insights about the shape and size of colloidal subunits within halide perovskite precursor solutions. SAS overcomes the limitations of traditionally more employed methods, such as UV-vis or DLS, which are more challenging to implement at a typical concentration in use for halide perovskite. We can probe the arrangement of the colloidal subunits, which are expected to impact the early stage of the crystallization process significantly and thus the final absorber layer of the perovskite material. The consistency of the SAS analysis using X-ray photons and neutrons on samples under different testing conditions was verified. Moreover, we supported our data interpretation with [207]Pb NMR analysis. The current findings give reason to assume the existence of interacting, highly-valent iodidoplumbates in concentrations of the precursor solution close to application in nanoscale in case of MAPbI$_3$ in a solvent mixture of DMF and DMSO.

We proved SAS as a non-destructive technique for studying the colloidal chemistry in size, shape and arrangement of perovskite precursor solutions. Understanding mechanisms, such as those linked to the use of additives in solution that are not included in the resulting crystal structure and still show a significant influence on the device performance can be approached from an entirely new perspective.[177,178] Hence, SAS is convincing as a characterization technique that can help to unravel novel crystallization mechanisms in future research.

3.6 Summary & Outlook

By introducing the SAS technique as a suitable characterization methodology for perovskite precursor solutions, a higher-level dynamic arrangement (>1000 nm) consisting of nanoscale (roughly 1 nm) subunits has been detected for the concentrated MAPbI$_3$ perovskite precursor solution. The initial use of neutrons underlines the reliability and quality of the data obtained for this study, further supported by the overlapping scattering curves of several repetitive measurements of the same sample using X-ray photons. This serves as an essential parameter being a relevant starting point for the scientific discussion and placement of SAS in the perovskite research community.

Hence, we demonstrate that SAXS and SANS can directly characterize the colloidal nature of perovskite precursor solutions. In particular, we provide the model fit of form- and structure factor to obtain specific information about the NPs present in the perovskite precursor. In this scope, we investigate the size and shape of the colloidal subunits and their inter-particle forces. These prevailing forces result in the equilibration of an optimal mean distance between the subunits of about 2 nm. The recurring distance leads to the formation of superordinate structures, which are of the order of r = 2000 nm. This work thus provides the first insights into the basic colloidal properties, NP constitution and arrangement in the perovskite precursor solution.

Moreover, we highlight the advantages of SAS in addition to widely applied standard methods. The objective is to make the technique of SAS more accessible and to emphasize its application in the characterization of solutions directly used in the production of perovskite solar cells. Currently, SAXS/SANS are not one of the

frequently used methods for perovskite precursor characterization. This work aims to highlight the application and possibilities of SAS clearly and understandably and thus serves as a guiding force for the subsequent studies dealing with the characterization of basic solution properties of different perovskite precursors. With this milestone, we intend to provide accessibility to a larger user community.

This work is discussed in further detail in *Chapter 6*.

4 Colloidal stability - a Critical Factor Influencing the Perovskite Formation

This chapter is based on a manuscript submitted in October 2021 to *Chemistry of Materials* with the title "Insights into the Early Stages of Lead Halide Perovskite Formation in Dependence of the A-site Cation" by **Marion A. Flatken**, Eros Radicchi, Robert Wendt, Ana Guilherme Buzanich, Eneli Härk, Jorge Pascual, Florian Mathies, Oleksandra Shargaieva, Albert Prause, André Dallmann, Filippo De Angelis, Armin Hoell, Antonio Abate. (Status: in revision)

M. A. Flatken conceptualized and investigated the presented research question, performed the SAXS measurements and took care of the data processing, evaluation and interpretation and the evaluation and analysis of EXAFS, GIWAXS and NMR data. She was responsible for the general project administration and wrote the original draft. E. Radicchi and F. De Angelis performed the DFT data calculations. R. Wendt supported SAXS data interpretation. A. Buzanich gave experimental support as a beamline scientist at the BAMline at BESSYII, performing EXAFS measurements and helped with the data processing. E. Härk helped to record the SANS data as a beamline scientist of the V4 beamline at BERII. J. Pascual assisted in writing the original draft. F. Mathies performed contact angle measurements. O. Shargaieva supported with beamtime at the KMCII diffraction beamline at BESSYII and with GIWAXS data processing. A. Prause performed and evaluated the DLS data. A. Dallmann was responsible for recording the ^{207}Pb NMR spectroscopy data. A. Hoell is in charge of the ASAXS instrument from HZB used for SAXS experiments presented here. He supervised and reviewed the manuscript. A. Abate supervised, provided the resources, reviewed and edited the manuscript before submission.

4.1 Introduction

The demand for renewable energies is constantly increasing. Due to their compelling material features, metal halide perovskites (MHPs) offer one promising opportunity for cost-effective and renewable energy harvesting. Beyond photovoltaics MHPs a have led to a wide range of applications in photovoltaics and light-emitting diodes, nanowire lasers, or photo-detectors.[39,143,144] However, this unique nature of perovskite materials and solar cell devices implied new challenges, particularly in their reproducibility and stability.[179] These issues have been traditionally addressed through the broad versatility that perovskite materials offer, precisely their composition.[180,181] The MHP structure is described by an ABX_3 formation, where the A-site is commonly occupied by organic and inorganic cations such as methylammonium (MA), formamidinium (FA) or cesium (Cs), the B-site by bivalent lead (Pb) or tin (Sn) cations and X-site by halide anions such as iodide, bromide or chloride (I, Br or Cl). The choice of composition strongly affects the resulting device characteristics, such as reproducibility, long-term stability and power conversion efficiency.[182] Among other compositional engineering strategies, the substitution and mixing of the A-site cation has shown significant improvements in performance, in particular with a significantly longer lifetime of the respective PSCs.[17,18,79,183,184]

In recent years, alkali metal cations, mostly Cs^+, Rb^+ and K^+, have been used to effectively improve the thin film morphology in multi-cation perovskites for the case of pure $MAPbI_3$ perovskite resulting in higher reproducibility and enhanced stability.[17,83,84] The monovalent alkaline cations K^+ and Rb^+ are too small to be incorporated in the perovskite structure considering the Goldschmidt tolerance factor.[18] Contrary, Cs^+ was proven to be part of the perovskite structure in the crystalline thin film, thus having a more pronounced influence on the crystallization, morphology and solar cell performance.[177,185] Still, all named alkaline elements are known to impact the final PSC performance significantly.[186–189]

Previous studies demonstrate enhanced photovoltaic properties of perovskite solar cells (PSCs) due to A-site cation mixing or addition.[17,18,183] Nevertheless, there is a lack of understanding the underlying mechanisms that explain the observed improvements. Neither K^+ nor Rb^+ are part of the perovskite crystal structure itself but still influence the thin film crystallization. The early stages of perovskite formation, which are critical

for the resulting morphology, are set already in the precursor solution by the presence of strongly interacting iodidoplumbates.[8,133,145,147] Hence, alkali cations must affect the precursor solution properties and consequently the perovskite formation.

Currently, many researchers attempt to understand the chemistry behind perovskite precursor solutions better, as there is a direct link to the final PSC performance.[127,190–193] M. Abdelsamie *et al.* uncovered the influence of thiocyanate additives on the solution chemistry, which can be viewed as a follow-up from a previous work where extended X-ray absorption fine structure spectroscopy (EXAFS) was used to describe the chemical bonding between Pb and halides in the precursor solution.[15,16] Further, theoretical calculations revealed possible iodidoplumbate formations explaining absorption data of diluted precursor solutions.[147,194] For the first time, the significant influence of the A-site cation was demonstrated in molecular dynamics simulations by P. Ahlawat *et al.*, introducing a detailed nucleation mechanism for the perovskite formation.[195] Based on the physicochemical interaction between the solute and the solvents, the perovskite precursors in typical concentrations for PSC processing can be regarded as a colloidal dispersion rather than a chemical solution (homogeneous mixture).[196,197] Within such a system, colloidal stability is an essential elementary concept, which is indispensable for understanding the fundamental properties of the precursor state.[14,110,111] The tendency of the colloidal system to aggregate, agglomerate, or undergo coalescence determines its chemical stability.[118] Repulsive forces between the colloidal nanoparticles (NPs) stabilize the system. They can be influenced sterically by adsorption or binding of large molecules at the particle surface, or electrostatically by ion concentration and type.[110,118] Accordingly, understanding the A-site cation's direct impact and the fundamental concept of the A-site cation mixing (including the targeted use of additives) will bring the perovskite community an unprecedented step closer to the controlled stabilization of these systems and consequently to the design and fabrication of PSCs.

With this aim, we studied precursor chemistry, including the nucleation and growth processes of perovskites and how this is affected by alkali salts. To do this, we investigate the chemistry of the precursor dispersion on a nanostructural level. First, we prove the vital role of the MA^+ A-site cation in colloidal dispersion. In particular, we demonstrate that the NPs, usually constituted by iodidoplumbate complexes of different order and aggregation,[196] found in PbI_2 precursor solution differ in their chemical nature

compared to the MAPbI$_3$ precursor. Therefore, we perform EXAFS on an inter-atomic level and SAS concerning larger, superordinate structures. By adding monovalent alkali cations K$^+$, Rb$^+$ and Cs$^+$ to MAPbI$_3$ and FAPbI$_3$ precursor solutions, we explore the influence of the addition of alkali metal cations on the precursor chemistry, the nucleation and growth mechanisms. In all investigated precursor solutions, we discover the presence of a dynamic colloidal network of nanoscale subunits formed via oriented attachment (OA) (showing almost a pseudo-crystalline structure), which can be regarded as one first nucleation step. Using SAS in combination with nuclear magnetic resonance (NMR) spectroscopy, we further identify that this interaction, dominated by repulsive forces, starts in the perovskite precursor dispersion and differs according to the perovskite composition. Utilizing these techniques, we reveal a comprehensive image of the coordination chemistry of the perovskite precursor, which is then connected to the thin film crystallization and morphology of the perovskite by applying grazing incidence wide-angle scattering (GIWAXS) and scanning electron microscopy (SEM). The findings presented in this work provide a mechanism for crystal growth and explain morphology changes in the resulting perovskite thin films. The improved understanding of how monovalent cations as additives interact with the perovskite components in solution will allow more effective control of the perovskite morphology, improving the total reproducibility of stable and efficient PSCs.

4.2 Experimental Details

Sample Preparation

All chemicals used were of analytical grade and were used as received without any further purification. The MAPbI$_3$ perovskite precursor dispersion is mixed from PbI$_2$ (Tokyo Chemical Industry, > 98 %) and CH$_3$NH$_3$I (Dyenamo, > 99.99 %) 1:1 in mixed solvent *N,N*-dimethylformamide and dimethyl sulfoxide (DMF:DMSO (Sigma-Aldrich) prepared by volume/volume (v/v) ratio of 6:1 reaching a concentration of 1 mol L^{-1}. For the neutron scattering and NMR experiments, deuterated solvents DMF-d7 and DMSO-d6 (Sigma Aldrich, >= 99.5 atom %) are used. The resulting perovskite dispersion is shaken at 60 °C for 5 min to dissolve all components. For the plain PbI$_2$ precursor solution, PbI$_2$ is dissolved in the same solvent mixture of DMF:DMSO (6:1, v/v), reaching a concentration of 1 mol L^{-1}. Additives KI (Sigma Aldrich), RbI and CsI (abcr GmbH, 99.8 %) are dissolved in the same solvent mixture and added to the MAPbI$_3$ perovskite precursor dispersion with a relative content of 5 vol%, 10 vol% and 15 vol%, respectively.

Perovskite thin films were prepared on an ITO substrate spin-coated with 4000 rpm for 25 s. As an antisolvent, 450 µL of ethyl acetate (Sigma Aldrich) were dropped onto the perovskite after 20 s of spin-coating. Afterwards, the films are annealed on a hot plate for 1 h at 100 °C.

Nuclear Magnetic Resonance Spectroscopy, ^{207}Pb NMR

The spectra were acquired on a Bruker AVII 400 MHz or Bruker AVIII 500 MHz equipped with room temperature TBO or BBO-probe heads, respectively. Typically, a sweep width of 897 ppm was used, and 8192 points were acquired, resulting in a total acquisition time of 54.48 ms. The center frequency had to be adjusted from sample to sample to detect the desired signal; therefore, on new samples, a full scan of the possible shift range was acquired until the peak was detected. We used a 30° pulse to minimize the recycle delay to 200 ms (for samples with extensive peaks, acquisition time and recycle delay were adjusted to 50 ms). The number of scans thereby was 512 for the comparably concentrated samples (~1 mol L^{-1}). All spectra were measured with

standardized parameter sets from Bruker Topspin version 2.1 (AV400) and 3.0 (AV500).

Dynamic Light Scattering, DLS

DLS measurements were carried out with a 3DSpectrometer (LS Instruments, Switzerland). The setup uses a He-Ne laser with a wavelength of 632.8 nm and a goniometer to set the scattering angle 2θ between 15 and 145 °. The samples were measured from 20 ° to 135 ° in 5 ° steps with 30 s for each measurement. It must be noted that the measurement time is not sufficient for the slow relaxation rates observed in the correlation curves. However, the initial focus was set on the small particles in the solution. The temperature was set to 25 °C. Analysis of the obtained intensity correlation data represented as $g^{(2)}(\tau) - 1$, was performed with self-written python-based software. The intensity correlation function $g^{(2)}(\tau)$ is related to the field correlation function via the Siegert relation $g^{(2)}(\tau) = 1 + \beta \left(g^{(1)}(\tau) \right)^2$. The data were fitted with a bimodal exponential model; see the following equation.

$$g^{(2)}(\tau) - 1 = \beta(a_1 e^{-\Gamma_1 \tau} + a_2 e^{-\Gamma_2 \tau})^2 \text{ with } a_2 = 1 - a_1$$

where β is the instrument-specific coherence factor, τ the correlation time, and a_i and Γ_i the amplitude and decay rate for the corresponding species I, respectively. The collective diffusion coefficient D_{coll} was determined by a linear fit of Γ versus $q2$, where q is the magnitude of the scattering vector. From this fit, D_{coll} results from the slope according to $\Gamma = D \cdot q^2$. The hydrodynamic radius was finally calculated via the Stokes-Einstein equation, $R_h = \frac{k_B T}{6\pi\eta D}$, where k_B is the Boltzmann constant, T the absolute temperature and η the viscosity of the solvent.

Extended X-ray Absorption Fine Structure Spectroscopy, EXAFS

EXAFS (extended X-ray absorption fine structure) measurements were performed at the BAMline (BESSYII, Helmholtz-Zentrum Berlin, Germany).[198] The beam was monochromatized using a double-crystal monochromator (DCM) Si(111). The size of the beam spot was 4 mm × 1 mm. The measurements were performed at the Pb-L3 edge

(13.035 keV) in fluorescence geometry. The excitation energy was varied in 10 eV steps before the edge, 1 eV step in the near-edge region and 0.04 Å for the k-space in the EXAFS region.

The characteristic fluorescence radiation (Pb-Lα line) was measured with a custom made four-element SDD in backscatter geometry (LLA Instruments GmbH & Co. KG, Berlin, Germany). The single 30 mm^2 detector modules were supplied by Ketek (Munich, Germany). EXAFS data were processed by using ATHENA and ARTEMIS. These GUI programs belong to the main package, IFEFFIT[199]. The phases for PbI_2 (.cif-file of PbI_2DMSO_2)[191] and $MAPbI_3$ (.cif-file of $(CH_3NH_3)_2Pb_3I_8DMSO_2$)[191] were theoretically modelled and fitted to the measured spectra using ARTEMIS.

Small-Angle Neutron Scattering, SANS

SANS measurements were performed at the V4 beamline at the BERII reactor, HZB in Berlin.[156] The detector distance was 1 m with using a wavelength of 4.5 Å. Hence, a q-range of approx. 0.5 nm^{-1} to 8 nm^{-1} was covered (0.78 nm - 12.6 nm). The perovskite solutions for SANS measurements were measured inside quartz cuvettes Hellma® cuvette (Hellma Analytics, Germany) with a 1 mm optical path length. The quartz cuvettes filled with the perovskite solution were sealed with polytetrafluoroethylene (PTFE) caps and Parafilm® to inhibit the evaporation of deuterated solvent from the sample to prevent the adsorption of moisture from the outside environment. Each sample was measured with temperature control at 20 °C. An "Ultra-Cryomat" from Lauda was used to set and hold the temperature during the measurements. A cadmium aperture with a diameter of 13 mm was used directly in front of any cuvette filled with the perovskite solution. Scattering contribution from mixed solvent DMF-d7 and DMSO-d6 solution was measured separately. SANS curves of each sample were recorded every 5 min followed by a 20 s transmission scan. Of these, four repetitions were performed to increase the statistics for each condition. The measured SANS curves are in good agreement, coincide and are reproducible. Therefore, the four runs were merged for each condition respectively to achieve better statistics. The measured SANS patterns overlap, and no change in the measured transmission can be observed during the measurements, giving rise to the assumption that we do not observe any change in solution, e.g. no radiation damage.

Data processing (SANS): For data reduction and the radial averaging to the 1D scattering SANS pattern, the BerSANS software was used.[157] Normalization and background subtraction routines were performed using the scattering data from standard H_2O-filled cuvette, empty cuvette and cadmium plate used as neutron absorber, respectively. The corresponding transmission values for each sample were taken into account. Four 5 min scattering runs were merged to achieve better statistics. Based on the theoretical model presented in **Figure 16c**, a structure model that includes a spherical form factor and a hard-sphere structure factor was chosen to fit the scattering data for PbI_2 using the program SASfit[140]. To fit the $MAPbI_3$ scattering data, a cylindrical form factor combined with a hard-sphere structure factor gave the best model fit. The model fits and corresponding parameters are presented in **Figure S4.1**.

Small-Angle X-ray Scattering, SAXS

The reported SAXS data were measured using synchrotron radiation at the four crystal monochromator beamline in the laboratory of PTB (Physikalisch-Technische Bundesanstalt) at BESSYII.[158] The SAXS instrument of HZB contains an adjustable about 3.5 m long support structure with a long edge-welded bellow system to allow the possibility to vary the sample to detector distance without breaking the vacuum.[159] The two-dimensional scattering images were collected by a windowless DECTRIS 1M PILATUS2 in-vacuum hybrid-pixel detector. The measurements were carried out at two different distances (0.8 m and 3.7 m) at photon energies of 10 keV and 8 keV, respectively. Thus, a q-range from 0.05 nm^{-1} to 8.5 nm^{-1} was covered. For a sample-sensitive measurement, the solutions were measured with an exposure time of 600 s with three repetitions for the shorter distance and three for the long distance to achieve good quality data and to monitor unwanted but possible changes of the specimen over time (which can therefore be safely excluded). Due to the low transmittance of the lead-containing precursor solutions, especially thin (0.1 mm), rectangular borosilicate cuvettes (with a wall thickness of 0.1 mm) purchased from CM Scientific, (UK) were used.

By constraining the beam with a low-scatter pinhole of germanium 500 μm in diameter, the total flux on the sample could be determined for each energy. Accordingly, for the

long-distance (3.7 m) where 8 keV was used, we can indicate 4.8 $*10^9$ photons/s and 2.6 $* 10^9$ photons/s for the short distance (0.8 m) where 10 keV was used.

Data processing: For data reduction and radial averaging to the 1D scattering pattern, the BerSAS software was used, an advanced version of the BerSANS software applicable for SAXS and SANS.[157] All SAXS curves of the investigated samples were fitted with the program SASfit[140]. A cylindrical form factor and a hard-sphere structure factor was chosen to fit all recorded SAXS curves. The herein investigated particles were considered as hard spheres. These particles are assumed as incompressible, resulting in fixed radii for each particle and an infinite repulsive force at a specific interparticular separation. However, the hard spheres model neglects attractive forces and describes various colloids in organic solvents reasonably well. We used the monodisperse Percus-Yevick approximation for hard spheres to fit the interaction of the analyzed colloidal particles. For example, the model fits of the scattering data of $MAPbI_3$, $MAPbI_3$ x 5 % CsI and 10 % CsI are displayed in **Figure S4.6**.

In-situ Grazing Incidence Wide-Angle Scattering, GIWAXS

In-situ GIWAXS measurements were performed using synchrotron radiation at the KMC-2 Diffraction beamline[200] from BESSYII, HZB and the area detector Bruker AXS. We set the photon energy of 8048 eV ($\lambda = 0.154$ nm) and fixed the incident angle at 2 *deg*. The area detector covered the range between 4.8 ° and 15.6 ° 2θ to collect the scattering. An Anton Paar setup was used to control the substrate temperature, and the temperature ramp is kept at around 50 °C/min during measurement. The sample environment consisted of constant nitrogen gas flow (6 L/h) during the measurement, directly connected to the Anton Paar setup. For the measurement, the sample precursor liquid was blade-coated on a substrate and measured within 30 s between the deposition and the start of the measurement.

Scanning Electron Microscopy, SEM

SEM images were recorded using a Hitachi S4100 or ZEISS Auriga 60 at 2 kV acceleration voltage and 25k magnification. For processing the SEM images to derive the grain size distribution, we used the software ImageJ[201].

Contact Angle Measurements

Wettability measurements were performed with a KRÜSS Drop Shape Analyzer (DSA100) at ambient conditions (20 °C, fume hood). The contact angle on an ITO surface was measured by the static sessile drop method.

Density Functional Theory, DFT, calculations

DFT calculations on the alkali-solvent complexes were run using the Gaussian 09 software package.[202] Geometry optimization was done employing the B3LYP exchange-correlation functional[203,204] and Grimme's van der Waals dispersion interactions DFT-D3[205], simulating solvents with implicit solvation models (polarisable continuum model, PCM)[206] and with explicitly added molecules. Mixed basis sets were adopted, employing 6-31G* for the DMSO and DMF solvent molecules. At the same time, for the solute, we picked up LANL2DZ/LANL2 basis sets/pseudopotentials for the K, Rb and Cs atoms and D95V for MA (being the same basis sets employed in LANL2DZ for the first row elements).

The formation energy, E_{form}, is evaluated as:

$E_{form} = E_{tot} - E_{cation} - n * E_{solv}$

where E_{tot} is the total energy of the system, E_{cation} is the energy of the cation, E_{solv} and *n* are the energy and the number of coordinating molecules of the solvent, respectively.

4.3 Results & Discussion

To obtain first insights into the nature of colloidal substructures, we compare the solution properties of a simple PbI_2 solution with a stoichiometric $MAPbI_3$ precursor dispersion.
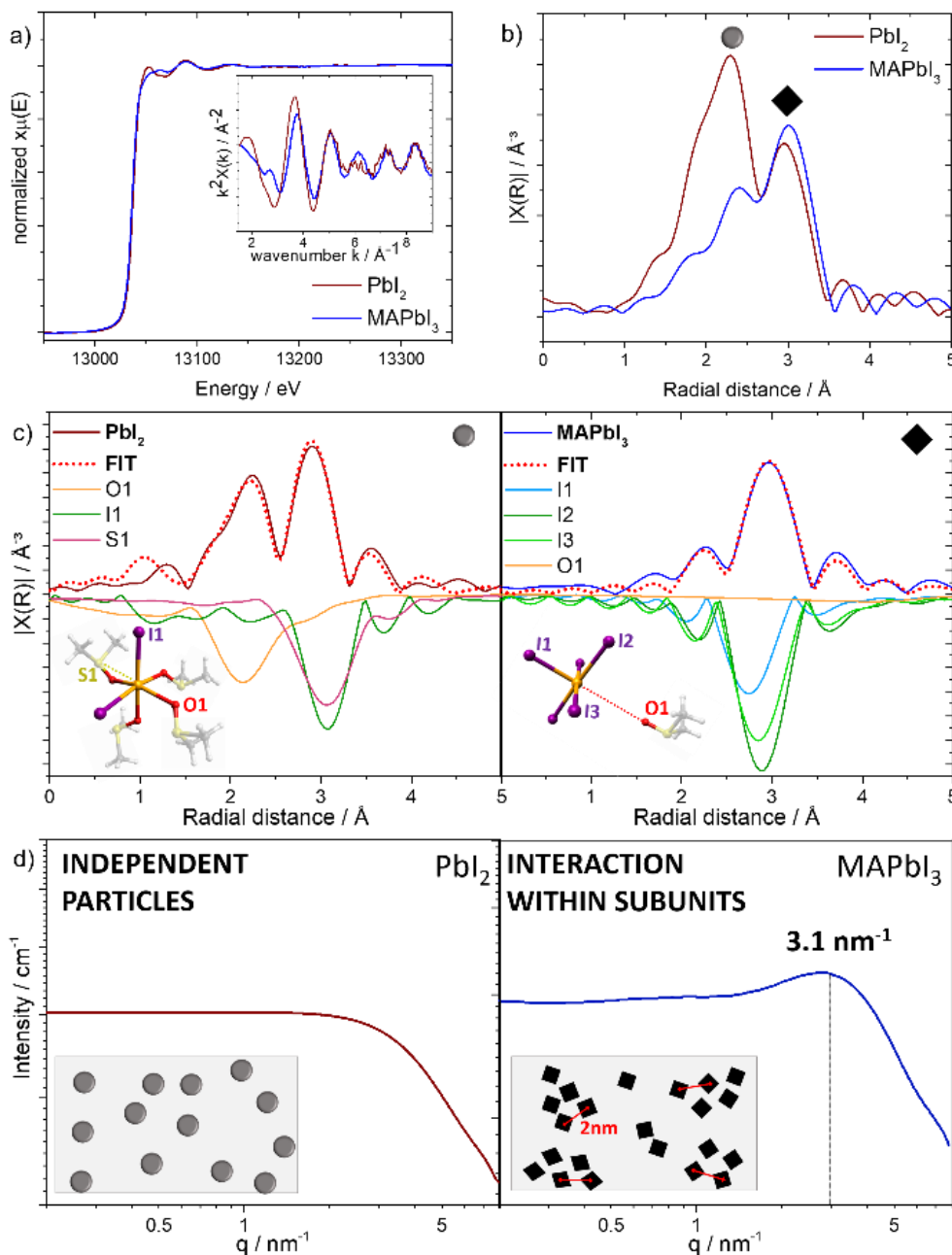
Figure 17. EXAFS and SANS of dissolved PbI_2 and $MAPbI_3$. a) X-ray absorption near edge structure (XANES) spectra of both samples presented with the corresponding k-space EXAFS spectrum given in the inset; b) magnitude of the Fourier transform of the k-space EXAFS data (k-weight: 2) ($|\chi(R)|$). Maxima of the amplitude show a clear difference in radial distance between PbI_2-like and Pero-like precursor formations. In c), the model fits with the scattering paths used are highlighted for PbI_2 (left) and $MAPbI_3$ (right). Ball and stick theoretical models based on these fits are reported as insets. SANS scattering curves of the respective samples are presented in d) with a schematic illustration of the colloidal interaction in an inset window of each graph.

Table 2. EXAFS fit parameters of MAPbI$_3$ and PbI$_2$ (reduced χ^2 of 129.7 and 74.41, respectively).

Sample	R-factor	Scattering Path	N	R_{model} /Å	R_{fit} /Å	R_{diff} /Å
MAPbI$_3$	0.007	Pb1 – I1	1	3.028	2.799	0.0525
		Pb1 – I2	2	3.177	2.948	0.0525
		Pb1 – I3	2	3.319	2.999	0.1023
		Pb1 – O1	1	4.985	4.989	0.0000
PbI$_2$	0.006	Pb1 – O1	4	2.490	2.497	0.0001
		Pb1 – I1	2	3.239	3.026	0.0454
		Pb1 – S1	8	3.724	3.539	0.0339

To date, MAPbI$_3$ is probably the most extensively studied composition of perovskites applied in photovoltaics.[61] We perform this comparison to systematically assess the influence of the MA$^+$ A-site cation. Both samples are prepared to employ a mixture of DMF:DMSO at a 6:1 ratio (v/v). EXAFS curves from the measurements performed at Pb L3-edge (13.039 keV) reveal that the lead coordination in the precursor differs significantly when comparing the plain PbI$_2$ to the MAPbI$_3$ specimen (**Figure 17a, b**). We further prove a strong dependency of the intrinsic formation and NP interaction on the A-site cation combined with SANS.

Figure 17a shows the comparison of their XANES spectra, highlighting differences in the near edge structure. The average distance to the most immediate neighboring electron density maximum can be seen in **Figure 17b**, given as well pronounced maxima, derived by the Fourier transform of the *k*-space EXAFS data presented in **Figure 17a**. By comparing the maximum amplitude of PbI$_2$ and MAPbI$_3$, we observe a clear difference, marked with a circle for PbI$_2$ and a square for MAPbI$_3$. A model fit of the data provides further information on the respective assignment of scattering paths to the data, for which we used Artemis from the software package IFEFFIT[199]. In the case of PbI$_2$, the first pronounced solid maximum at approx. 2.2 Å can be assigned to coordination to oxygen, available through the existing solvents (DMF or DMSO). Specifically, the Pb-S scattering signals we observe let us assign these oxygen atoms to the DMSO solvent, which is reasonable because of its higher coordinating power to lead compared to DMF. The following peak at a radial distance of approximately 3 Å belongs to the contribution of coordinating iodide (**Figure 17c**, left panel). We obtained the best fit for a coordination

number of 4 oxygen and 2 iodides (measured data and fit are presented in **Figure 17c**). The fit parameters and respective coordination number N are given in **Table 2**. In contrast, for the MAPbI$_3$ precursor, the first coordination sphere of Pb consists mainly of iodide, at radial distances similar to the ones observed for PbI$_2$ in solution. However, the oxygen from the solvent only coordinates in a subsequent neighboring sphere at higher radial distances. We used iodide coordination of 5 for the model fit represented in **Figure 17c** (see **Table 2**).

Consequently, the atomic environment of lead observed in the MAPbI$_3$ significantly differs from the one observed in PbI$_2$. Therefore, these cannot directly be equated, contradicting nucleation approaches and calculations proposed by previous research groups.[145,147] The current findings prove the importance and specific role of the A-site cation since it directly impacts the first NPs formed, introducing the perovskite crystallization process in the precursor dispersion. Based on the structural differences in solution, we use PbI$_2$-like (grey circles) and perovskite-like NPs (black squares) in the following to describe the different atomic arrangements (**Figure 17c**). To further investigate the diverse nature of the Pb-based precursor dispersions, we used a non-destructive neutron technique, SANS, especially suitable to investigate NPs and their interaction. **Figure 17d** presents the measured SANS scattering curves of PbI$_2$ and MAPbI$_3$, respectively, in the same solvent mixture of deuterated DMF:DMSO. The course of each scattering curve at high q-values indicates the presence of small structures in solution, which can be assigned to a form factor in the sub-nanometer scale (**Figure S4.1**, 9.2). Although the dimensions seem to be similar, the scattering curves show significant differences in their specific shape. In the case of the plain MAPbI$_3$ precursor (**Figure 17d**, right panel), a maximum emerges based on a dominant structure factor. A structure factor evolves due to strong repulsive particle interactions in a system.[133] As a result of the repulsion force, the scattering intensity of the single-particle contribution decreases, reduced to the benefit of an arising peak at a $q_{max}=2\pi/d$. Using the magnitude of q at the peak maximum the mean spacing d between the mass centers of the respective interacting particles can be determined.[133,139,207] Depending on the strength of the interactions, the maximum is differently pronounced, further revealing how often the specific distance d is repeatedly present in the specimen.[208]

By combining the information on an atomic level derived by EXAFS and the sub-nanoscale observations from SANS, we can confirm that particles are present in both

solutions. However, the corresponding NPs differ on the atomic scale and interact differently. The difference in interaction is displayed schematically in the insets of the respective SANS curves in **Figure 17d**. In the case of MAPbI$_3$, a significant influence of particle interaction can be observed with a mean d-spacing of approx. 2 nm, obtained using Bragg's law with $q_{max} = 3.1$ nm^{-1}. In the PbI$_2$ solution, the interactions are negligibly low, indicating that the A-site cation holds a highly relevant role in the formation process already in the precursor solution by promoting interactions between the formed NPs.
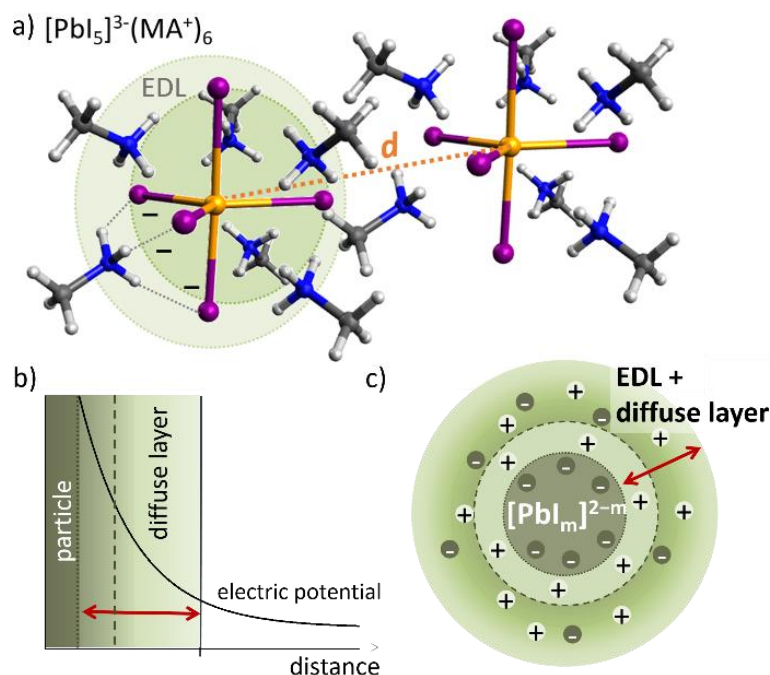
Figure 18. Illustration of the DLVO-theory applied to MAPbI$_3$. a) provides a possible formation of MAPbI$_3$ particles based on the EXAFS data fit (Table 2). The decrease of the electric potential concerning the distance from the particle surface is presented in b) and a) scheme of a charged NP with an EDL in c).

The repulsive interaction observed in SANS for the perovskite-like NPs can be assigned to a typical electrostatic interaction in colloidal dispersions.[110] Using the DLVO (Derjaguin, Landau, Verwey and Overbeek) theory, these interactions can be explained by the emergence of an electrical double layer (EDL) made of the respective counter ions surrounding the NP and a diffuse layer (**Figure 18c**).[118] In general colloid science, the mechanism of NP stabilization is considered one of the fundamental principles. A colloidal system is deemed unstable without the briefly described repulsive forces since van der Waals forces will attract the particles and agglomerate. NPs in a stable system carry a surface charge so that an EDL and a diffuse layer surround them to balance this charge. The originating Coulomb repulsion forces between individual NPs decrease

exponentially with respect to its distance (**Figure 18b**). If the repulsion is strong enough, this can prevent aggregation. Following the concept of colloidal stability, the activation energy (see total interaction potential (**Figure S4.2**, 9.2) to aggregate that two particles have to exceed when they collide can be influenced by the strengthening or weakening of the Coulomb repulsive forces.

Considering the results from EXAFS, we expect the PbI_2 solution to exhibit uniform dissolution properties, forming only weakly charged, isolated solvated complexes (coordination of 2 iodides and 4 oxygen). These cannot build strong repulsive forces amongst themselves, which further lowers the level of interaction. However, the perovskite-like NP can be assigned to highly coordinated lead and are hence negatively charged. They serve as subunits of a dynamic colloidal arrangement, where inter-particle forces result in a higher-level structure (superstructure), which most certainly serves as the initial basis for crystallization. In a pure $MAPbI_3$ dispersion of 1 mol L^{-1}, we claim that perovskite-like iodidoplumbates coexist and interact repulsively. Although specific colloidal stability is reached, we can observe a formation of large superstructures, which can be supported by slow relaxation times (in the sense of diffusive motions) measured in DLS, revealing the existence of large-size domains (**Figure S4.3**, 9.2). The negatively charged perovskite-like NPs are surrounded by the counter ion, here MA^+ and solvent. The emergence of a corresponding EDL and differences in the electric potential can explain the observed repulsive interactions, considering the differences in the atomic level between the PbI_2-like and the perovskite-like formations in solution. Since these NPs interact and result in a specific recurring distance d between the perovskite-like structures, we can also explain the formation of larger-scale (micrometre range) colloidal superstructure networks consisting of perovskite-like NPs as essential building blocks in the precursor dispersion. The existence of large colloids is consistent with results obtained by DLS in previous studies.[8,133,146,196,197,209] In **Figure 18a**, we report a hypothetical model, based on the EXAFS data fit, for the formation of the double layer in the case of perovskite-like NPs. Here, solvent molecules are not shown since they do not appear to stay within the first solvation shell.

Aiming to investigate further the contribution of A-site cation to the perovskite precursor dispersion, we focused on the electrostatically achieved repulsive forces and thus the effect on the colloidal stability. Therefore, we introduced monovalent cations to the perovskite precursor as additives, in particular the commonly used alkali cations (i.e.

K^+, Rb^+, Cs^+) in the form of iodide salts. Proven by D. J. Kubicki *et al.*, Cs^+ is the only element of the alkaline cations detected in the crystalline perovskite structure.[177] However, Rb^+ and K^+ also significantly influence the perovskite crystallization, as pointed out previously. Liquid state [207]Pb NMR spectroscopy of MAPbI₃, as well as FAPbI₃ precursor dispersions with 5 %, 10 % and 15 % addition of the respective alkaline cation (K^+, Rb^+, Cs^+), provides a clear trend only for the case of the Cs-addition, lowering the chemical shift with higher cation concentration (**Figure S4.4**, 9.2). Since pure CsPbI₃ gives a signal at a lower chemical shift than MAPbI₃ and FAPbI₃, the change in the signal might be related to the coexistence of already more CsPbI₃-like and MA/FAPbI₃-like precursors in the sample (**Figure S4.5**, 9.2). On the contrary, K^+ and Rb^+ only show signal fluctuations, with no discernible trend.
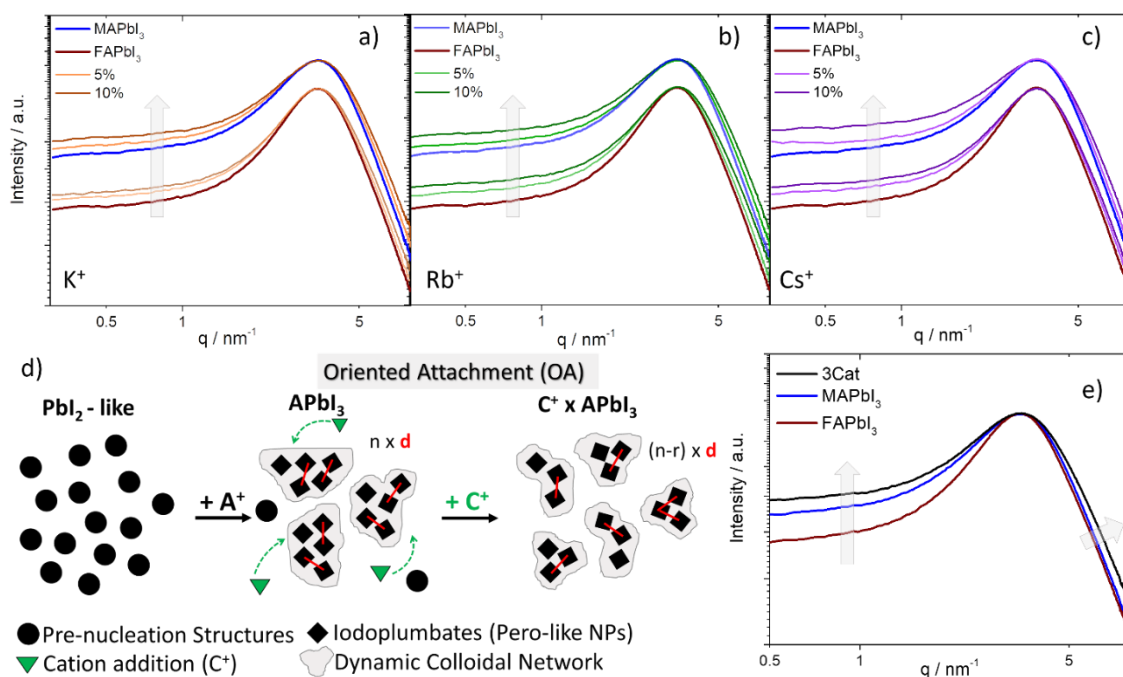
Figure 19. SAXS data measured on precursor dispersions. a) K^+ b) Rb^+ and in c) Cs^+-ions added to MAPbI₃ and FAPI precursor, respectively. e) Comparison of FAPbI₃, MAPbI₃ SAXS curve to triple cation. d) Schematically interpretation of SAXS data as proposed mechanism based on the non-classical nucleation theory regarding the formation of superstructures, including oriented attachment. A^+ refers to possible A-site cations being part of the ABX_3 perovskite-type structure (e.g. FA^+, MA^+) and C^+ represents additional cations, such as the monovalent alkali metal cations discussed in this work.

The data obtained by NMR needs to be combined with further analyses to reveal what the three alkali metals have in common and how they affect the perovskite formation, regarding the thin film growth on a substrate resulting in an improved morphology. We know from SANS measurements that the NP interactions play a crucial role in the precursor dispersion. Hence, we performed transmission SAXS on MAPbI₃ and FAPbI₃ dispersions in the same DMF:DMSO solvent mixture. We added 5 % and 10 % of the

alkali metals, K^+, Rb^+ and Cs^+ (**Figure 19a-c**, respectively) to each organic perovskite dispersion. In both cases ($MAPbI_3$ and $FAPbI_3$), the scattering intensity of the single-particle increases with increasing alkali metal content, showing a similar behavior for the three cations (for illustrative reasons, the scattering curves of **Figure 19a-c** were aligned at the maximum peak of the q value for both $MAPbI_3$ and $FAPbI_3$). As a result, the repulsion forces present are decreasing, and the structure factor maximum is less pronounced, becoming broader. The broader structure factor maximum indicates a less frequent occurrence of the specific distance d when compared to the plain perovskite precursor. The model fit of the scattering curves separated into the respective contribution of the structure and the form factor is displayed in **Figure S4.6**. The dimensions of the cylindrical form factor used for the model fit match the perovskite-like NP structure depicted in **Figure 17c**, thus implying a negatively charged NP surface.

The lower Coulomb repulsion by the NPs gave rise to assume that the addition of the alkali cation is changing the previously described surrounding layers of the NP (**Figure 18c**). The ion concentration, meaning especially the counter-ion (here: cation) concentration, strongly influences the repulsive term of the total interaction potential within the colloid. In the diffuse layer, the counter-ions are dominant. Therefore, the ion concentration directly affects the repulsive forces and is proportional to the decay of the electric potential (as displayed in **Figure 18b**). The exponential decay of the total interaction potential goes steeper as the ion concentration increases, especially the counter-ion concentration.[110] We, therefore, expect a reduced diffuse layer with a higher concentration of the cation.

Notably, adding the alkali salt, we added iodide as an already present part of the NP structure itself. Moreover, the high coordinative environment of the employed DMSO:DMF mixture does not facilitate iodide coordination (which is also added in a relatively small amount) to the lead. Therefore, we do not expect it to modify the NP structure substantially. This is confirmed by EXAFS (**Figure S4.7**, 9.2) and SAXS curves (**Figure 19**), which do not show significant differences in the shape-changing from one system to another. Consequently, we assume that the iodide, which is added to the system via the alkali salt, is insignificant in the change of the repulsive interaction. Thus, only the introduced counter-ion (in the form of the monovalent alkali cation) changes the cation concentration in the diffuse layer and relevantly influences the Coulomb repulsion forces, i.e. the stability of the NPs in the dispersion. We further performed

DFT calculations to simulate the interaction of each considered A-site cation with the solvent. Here we observed less interaction of the alkali cations *vs* MA^+, explicitly following the trend $MA^+ > K^+ > Rb^+ > Cs^+$, which additionally makes them more mobile in solution so that they can diffuse more freely and participate to a greater extent in the formation of the double layer (**Figure S4.8**, 9.2). This may also indicate slight compositional changes in the diffuse layer, affecting the profile of the electrical potential. Hence, we can explain the decrease of the repulsive interaction by a decreased layer formation, resulting in lower colloid stability. The above-described phenomenon is equally applicable to the widely used $Cs_{0.05}(FA_{0.85}MA_{0.15})_{0.95}Pb(I_{0.85}Br_{0.15})_3$ composition, also known as "triple cation" perovskite, which shows reduced repulsion forces in comparison to the plain $MAPbI_3$ and $FAPbI_3$ dispersions (**Figure 19e**). In addition, we measured the contact angles of these dispersions on indium tin oxide-coated substrates, supporting the trend in surface potential (**Figure S4.9**, 9.2). The given contact angle already provides the first link towards film formation considering a work from X. Xu *et al.* where a higher contact angle has been assigned to a dominant homogeneous nucleation process, meaning dominant prearrangement and nucleation in the dispersion compared to the heterogeneous nucleation.[210] In **Figure 19d**, we provide a schematic interpretation of a plausible working mechanism, including the impact of the additional cation (here: alkali cation, in the scheme represented as C^+) on the nucleation and growth process. The findings lead to the assumption that the primary influence can be assigned to the operation of OA. Considering homogeneously dissolved precursors, as seems to be the case for a simple PbI_2 solution, the addition of the A-site cation leads to the formation of perovskite-like NPs that interact and create a colloidal network via OA, as it can be typically found in non-classical nucleation theory.[13,109,211] However, introducing now additional counter ions to the system (e.g. alkali cations), we observe that the total occurrence of the recurrent distance d is lower (see SAXS **Figure 19a-c**: broader structure factor maximum), suggesting that the general size of the formed networks is smaller.[208] Smaller colloidal networks representing the starting point for the different nucleation and growth mechanism would explain the observed differences in morphology. A narrower grain size distribution with smaller dimensions can be observed by comparing $MAPbI_3$ to the respective thin films with alkali metal addition (**Figure S4.10**, 9.2).
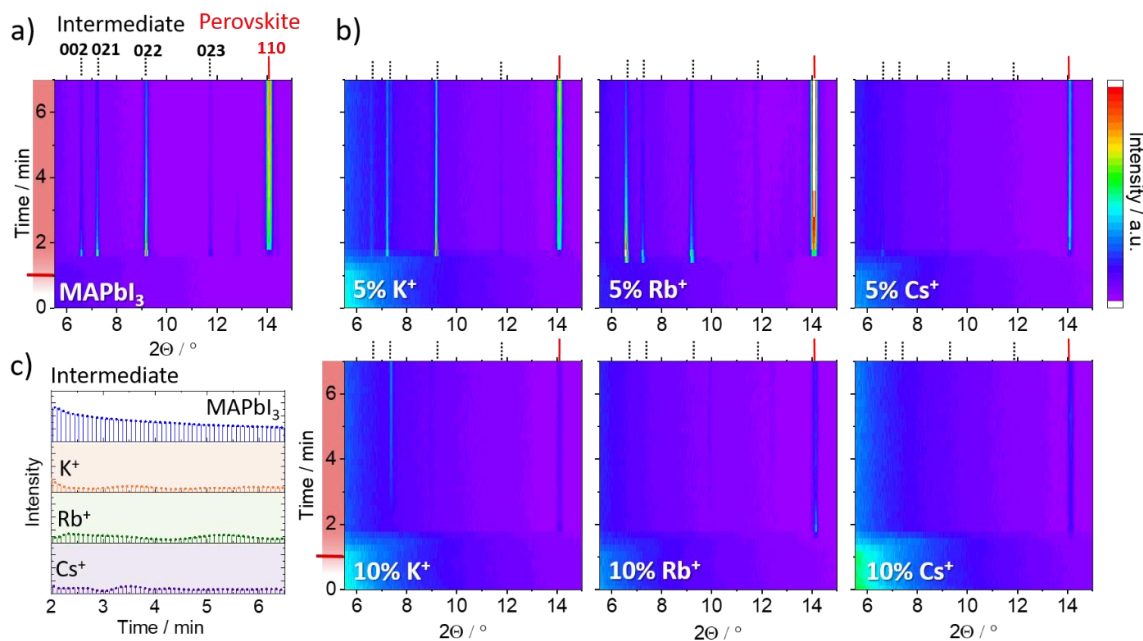
Figure 20. In-situ GIWAXS data during crystallization. Evolution of the thin film formation over time and temperature. The temperature control was applied after 1 min of measurement at RT, then ramping up to 100 °C. Using a heating rate of 50 °C/min as represented by the red bar on the x-axis with a mark for the start of the tempering process. a) MAPbI$_3$ showing both the intermediate[191] and the dominant perovskite diffraction peak given in black dots and red line, respectively. b) Provides the in-situ GIWAXS data of MAPbI$_3$ dispersions, including different percentages (5 % and 10 %) of K$^+$, Rb$^+$ and Cs$^+$. A comparison of the residual intensity of the intermediate phase, using the peak intensity of the (022) plane for the case of 10 % addition is presented in c).

To combine and apply the findings in more detail with the actual thin film formation and resulting morphology, we performed in-situ GIWAXS on the previously investigated MAPbI$_3$ dispersions, including the different percentages (5 % and 10 %) of the additional counter-ion. The dispersion was blade-coated on a glass substrate and measured right away, keeping the temperature at 25 °C for the first minute and then ramping the temperature up to 100 °C to investigate the thin film formation. As displayed in **Figure 20a**, the plain MAPbI$_3$ dispersion is directly forming perovskite, evident by the well pronounced (110) peak at 2θ = 14 ° (at 8 keV, 1.54 Å). However, another substantial contribution at the lower two theta values can be observed that can be assigned to a known intermediate phase (MA$_2$Pb$_3$I$_8$DMSO$_2$) formed in the presence of DMSO.[191] Comparing this to the 5 % addition of the alkali metals in **Figure 20b**, we observed that in the case of Cs$^+$, the peaks related to the intermediate do not appear, whereas, for K$^+$ and Rb$^+$, the intermediate peaks are still evident, although already less pronounced compared to the plain MAPbI$_3$ sample. To reach a more extreme scenario, we added 10 % of the alkali metal ions, observing that the peaks belonging to the intermediate phase become negligibly low in intensity even for the samples with K$^+$ and Rb$^+$ addition. As summed up in **Figure 20c**, only in the case of MAPbI$_3$ we observed the

existence of the intermediate that seemed to be stable over the whole time, whereas adding further counter-ions to the system makes the intermediate phase not extractable.
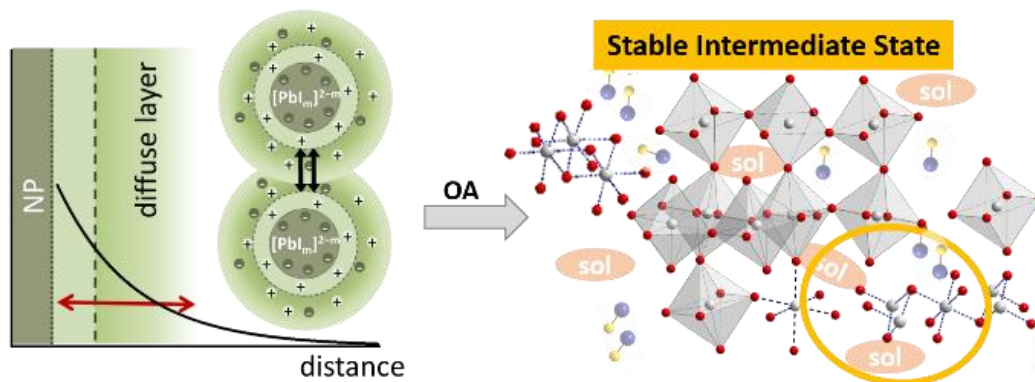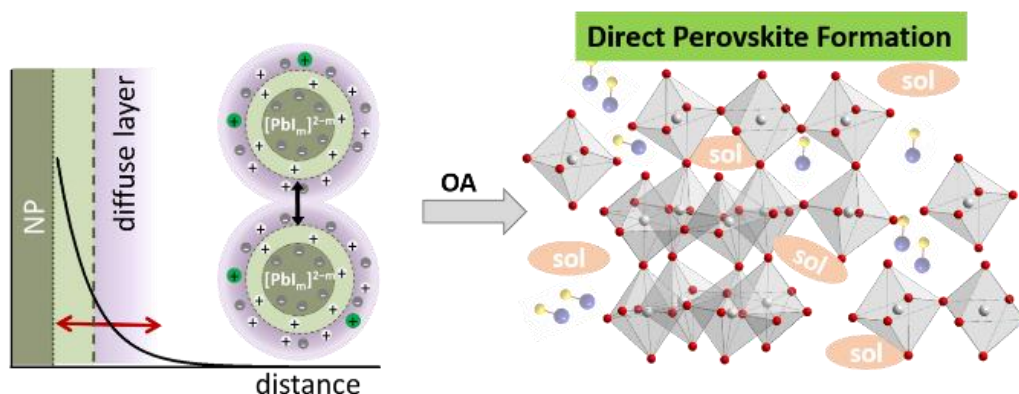
Figure 21. Influence of colloidal stability on the nucleation process. a) Well pronounced repulsion forces between particles enable to extraction of intermediate solvate phases during crystallization. Reducing the strength by an additional counter-ion in the EDL leads to a faster collapse of the solvated system and turns directly into the desired structure as shown in b).

Ultimately, the combination of GIWAXS and SAXS provides a comprehensive picture of the perovskite nucleation and its influence by alkali cations. The more vital repulsive forces in the plain perovskite dispersion (like $FAPbI_3$ and $MAPbI_3$) contribute to the stabilization of the NPs in the dispersion, leading to crystallization via solvent-based intermediates (**Figure 21**). This shows that the stabilized colloidal NPs in the dispersion can also be extracted and subsequently transformed into perovskite. Nevertheless, when this stability is affected, e.g. with further counter-ions, this might lead to less stable NPs in the dispersion.

Also, in this case, the approach of non-classical nucleation and growth can explain the phenomena based on the intrinsic colloid stability of NPs in the complex fluid. These

cannot be extracted, as they will convert into the perovskite-like structure much faster. The concept presented in this work to explain the fundamental influence of alkali metals on the mechanisms of perovskite formation offers the possibility of targeted manipulation of crystallization, even beyond the simple use of additives. The relevant layer formation (EDL and diffuse layer), which determines the speed and extent of the OA in the crystallization process via repulsive interactions, can equally be influenced by the solvent or sterically, e.g. by adding larger molecules to the system preventing colloidal NPs from aggregation (2D perovskites).

4.4 Conclusion

In this study, we provide a comprehensive picture of the structure of NPs existing in the perovskite precursor dispersion and a thorough explanation of the essential process of perovskite formation and how the addition of alkali cations influences it. EXAFS analysis provides insights into lead coordination, proving significant differences between dissolved PbI_2 and perovskite precursor NPs forming a dispersion. A model fit confirms that PbI_2-like NPs can be considered uncharged units, whereas perovskite-like NPs consist of charged, highly coordinated iodidoplumbates. SANS and DLS, in combination with the DLVO theory, further reveal essential differences caused by the structural composition of the NPs. Perovskite-like NPs compared to PbI_2-like ones tend to form dynamic colloidal networks driven by repulsive interactions among these charged subunits. This opens up an essential parameter about the comprehension of colloidal dispersions: colloidal stability, which gets mainly modulated by the repulsive interactions. In more detail, we show how the colloidal stability can be affected by known additives such as alkali cations and explain their role in the perovskite crystallization process. The combination of SAXS and in-situ GIWAXS allows us to present a detailed picture of the crystallization process by OA according to the non-classical nucleation and growth theory that can be directly applied to the perovskite formation affected by the addition of alkali salts. This work enables adjusting parameters already in the precursor dispersion to control the crystallization of the perovskite systematically. Thus, paths are opened up for transferring proven tools, such as alkali addition in organic-lead-based perovskites, to less explored compositions, like inorganic or tin-based perovskites. The rate and extent of the OA can be controlled by the colloidal stability as required by the fabrication process or composition of the perovskite. This can be done not only via additives as presented here and via the solvent or sterically by the addition of larger molecules.

4.5 Summary & Outlook

Whereas in *Chapter 3*, mainly SAS has been used to characterize the Perovskite precursor properties in the manuscript presented in *Chapter 4* we provide a comprehensive picture of the arrangements that we observe in the colloidal dispersions under investigation. Advanced X-ray techniques such as EXAFS, SAXS and GIWAXS in combination provide a broad picture of the crucial early stages in perovskite crystallization. Starting from a close view on an atomic scale using EXAFS, we present the constitution of the actual iodide coordination of lead in the MHP precursor. At the same time, SAXS provides a different perspective, including the particle interactions, while supporting the findings of EXAFS by matching sizes of the corresponding scattering form factor. Subsequently, in-situ GIWAXS links the observed precursor properties to the crystalline film and allows to directly assign the results to the perovskite thin film properties.

Since previously only $MAPbI_3$ has been investigated the knowledge has now been extended and applied to explain more common perovskite systems, addressing the addition of alkali cations. Highlighting the general mechanism behind cation addition, which is known to stabilize the perovskite absorber material in a PSC.[17,18]

The study highlights the specific role of the A-site cation since there are crucial differences in the constitution of the intermediates toward perovskite formation depending on the A-site addition. Given that the perovskite precursor solution is a colloidal system the DLVO theory including the colloidal stability, has been introduced to explain several effects observed in perovskite fabrication. The concept of colloidal stability within the non-classical nucleation theory provides the relevant parameters to influence the perovskite precursor systematically and thus the crystallization. However, today's literature is primarily refers to classical nucleation theories (e.g. LaMer) to explain the perovskite crystallization behavior.[212] Terms like oriented attachment, which are characteristic of the non-classical nucleation theory, appear mainly in context with perovskite crystal grain growth process.[13,213] Nevertheless, the presented data strongly indicates that in the case of the solution based perovskite processing we observe a crystallization mechanism following non-classical nucleation pathways going through the OA of agglomerates which is directly correlated to the colloidal stability, as presented in our study. Besides solvent engineering, the other parameter to

electrostatically influence the latter is given and discussed in this work by adding further ions (especially counter-ions) to the system. We thereby provide instruments for the perovskite research community to systematically influence and control the crystallization process, significantly reducing trial and error experiments and enhancing the targeted use of specific additives.

Using different solvents is another way to change the precursor chemistry, thereby changing the crystallization pathways. The binding strength of a solvent can be measured using the Gutmann Donor Number.[214] Considering this measure in a recent publication of D. Di Girolamo *et al.* underlined the relevance to study the effect of the solvent interaction with particular regard to tin-based perovskites.[23] Thus, understanding the mechanisms and concepts behind the perovskite formation process is crucial for further developing still less understood emerging materials. This includes tin-based perovskites, which are currently the most promising alternatives to the lead-containing counterparts and will be examined in greater detail hereafter.

This chapter will be discussed in further detail in *Chapter 6*.

5   The Impact of Fluoride Chemistry on Tin-based Perovskites

The work was published in Angewandte Chemie International Edition, 2021, 60, 21583-21591, with the title "Fluoride Chemistry in Tin Halide Perovskites" by Jorge Pascual, **Marion A. Flatken**, Roberto Félix, Guixiang Li, Silver-Hamill Turren-Cruz, Mahmoud H. Aldamasy, Claudia Hartmann, Meng Li, Diego Di Girolamo, Giuseppe Nasti, Elif Hüsam, Regan G. Wilks, André Dallmann, Marcus Bär, Armin Hoell and Antonio Abate served as the base for the following chapter of this thesis. Jorge Pascual and the author of this thesis contributed equally to this publication.

Figure 22. Cover illustration for Angewandte Chemie (Angew. Chem. 39/2021).

M. A. Flatken and J. Pascual conceptualized and investigated the presented research question, they shared the responsibility for the general project administration and wrote the original draft. M. Flatken performed the SAXS measurements and did the data evaluation and interpretation. J. Pascual evaluated, and A. Dallmann was responsible for recording the NMR spectroscopy data. C. Hartmann and E. Hüsam performed the HAXPES measurements and R. G. Wilks, M. Bär and R. Félix evaluated and visualized the data and R. Félix supported the original manuscript's writing. G. Li fabricated perovskite solar cells. M. H. Aldamasy measured and evaluated XRD. S.-H. Turren-Cruz measured and evaluated SEM. A. Hoell is in charge of the ASAXS instrument from HZB used to perform SAXS. A. Abate supervised, provided the resources, reviewed and edited the manuscript before to submission. All authors contributed to reviewing and editing the manuscript before to submission.

5.1 Introduction

Metal halide perovskite materials have shown enormous potential for the processing of efficient and stable photovoltaics.[215] However, the dominant type of perovskite solar cells (PSCs) are based on lead, a metal whose toxicity and environmental hazard can hinder its commercial application in numerous fields.[85] The lead threat pushed the scientific community to develop lead-free perovskite materials to maintain excellent photovoltaic performance while avoiding environmental risks. In this sense, tin halide perovskites are the best candidate to replace the dominant lead-based counterparts.[24,216] Nevertheless, these materials face some difficulties related to their inherent physicochemical characteristics.[217] The most important one is the ease with which Sn(II) oxidizes into Sn(IV) species, leading to the substantial decline in the performance through the undesirable formation of electron traps and p-doping of the material.[218] Previous studies have reported many origins of this oxidation, such as the solvent,[132,219] the processing conditions[220] or even spontaneously through disproportionation in tin-poor environments.[221] Stopping this oxidation is one of the requirements to achieve efficient and stable tin halide PSCs. For this reason, several trials have been made tackling the oxidation of Sn(II). These include the use of new solvent systems to avoid the oxidation by dimethyl sulfoxide (DMSO),[23] employing reducing agents to eliminate the content of Sn(IV), such as metallic Sn powder[131] or hypophosphorous acid[222] or introducing additives for alleviating the formation of Sn(IV), like the ever-present SnF_2.[19,218]
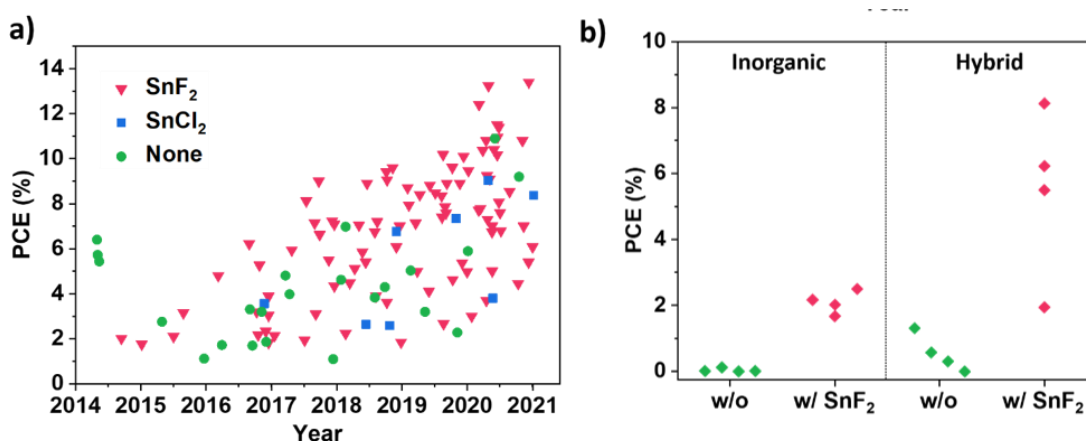
Figure 23. a) Highest PCE reported in tin halide perovskites literature containing solar cell data using SnF_2, $SnCl_2$, or none of them, ordered by date until Jan. 2021. b) Comparison of solar cell performance improvement in inorganic and hybrid tin halide perovskites before and after the addition of SnF_2, extracted from the studies in literature in which the comparison is made.

SnF_2 has achieved remarkable success as an additive in the tin halide perovskite field. Since its first use in PSCs by M. H. Kumar and co-workers,[223] it has been proven over time as an imperative to achieve good results (**Figure 23a**). There is barely any good cell performance report without SnF_2; exceptional cases use $SnCl_2$,[224,225] which may behave similarly to SnF_2, or 2D materials, which are another popular strategy for processing tin-based perovskites.[226–228] The appeal of SnF_2 in the community is such that the number of studies not using it (nor $SnCl_2$) quickly stagnated over the years, being in 2020 below 10 % of the total publications on tin halide perovskites in that year (**Figure S5.1**, 9.3). Its success lies mainly in the impossibility to obtain photovoltaic behavior in the solar cells fabricated without it. In **Figure 23b**, we collected data from studies in which solar cells were made with and without SnF_2.[124,223,229–234] The improvement in efficiency for both inorganic and hybrid tin halide perovskites is enormous, with negligible efficiency for the SnF_2-free cases. One of the most reported improvements is the better substrate coverage and film morphology obtained with SnF_2,[124,230,235] which implies that SnF_2 affects the film crystallization, a factor that remains unexplored. Nevertheless, its addition needs to be controlled, as a too-high content of SnF_2 is reported to induce phase separation.[124,230,235] Another reported effect is the ability of SnF_2 to reduce the formation of Sn(IV) and its related defects, with the reported benefits usually being reduced recombination[232] and a blue shift of the absorption onset.[232,236,237] Besides, K. J. Savill and co-workers found that even low amounts of SnF_2 are sufficient to positively impact mitigating Sn(IV) formation in tin/lead perovskites.[238] This effect on oxidation suppression could originate from introducing a Sn-rich environment, reducing Sn vacancies.[221] This interpretation has been proposed already in the first use of this additive by M. H. Kumar *et al.*[223] However, the question of what fluoride is doing and why we do not provide the Sn-rich environment simply with a higher SnI_2 ratio in respect to FAI remains unanswered. Related to this, other Sn(II) species that could provide the same beneficial effect were already discussed by T. Yokoyama *et al.*[239] Using SnI_2 excess also led to good results in one of the first studies on inorganic tin halide perovskites.[224]

Overall, reports in literature consistently lead to the same results: SnF_2 has a critical positive influence on the formation of high-quality $ASnX_3$ (where A = methylammonium (MA^+), formamidinium (FA^+) and Cs^+, and X = Cl^-, Br^- and I^-) films and holds a particular role in the stability of these materials against their oxidation to

Sn(IV). These two possibly related aspects are the key to SnF_2 being the predominant, most robust additive in the tin-based perovskite field. While there has been an extensive exploration of the impact and functioning of SnF_2 in these thin films, the chemical mechanism and influence in the processing are entirely unknown. Introducing an exact scheme of its working procedure remains a must in the field. This move would open the door to optimized application and help identify new additives in the future.

In this work, we explain the origin of the beneficial effects of SnF_2 in the processing and stability to oxidation of tin halide perovskites by studying the chemistry of fluoride in these solutions. Using a combination of complementary solution and film characterization techniques, we propose that the role of SnF_2 is not limited to the resulting thin film but also affects the precursor solution properties critically and hence their processing. The study of the solution chemistry of fluoride in formamidinium (FA)-based $FASnI_3$ precursor solutions by ^{119}Sn- and ^{1}H-NMR spectroscopy reveals a strongly predominant affinity of the fluoride anion for Sn(IV) over Sn(II). With the help of hard X-ray photoelectron spectroscopy (HAXPES) analysis, we show how SnF_2 increases the Sn(II) content in perovskite samples, an indication that Sn(IV) is partially prevented from being incorporated in the perovskite film. Meanwhile, small-angle X-ray scattering (SAXS) enables an understanding of how fluoride anion modifies perovskite subunits' interaction in solution, generating improved homogeneous crystal growth conditions. Furthermore, experiments with other fluoride species and $SnCl_2$ prove that these effects are not exclusive to SnF_2. Thus, the chemistry of a hard Lewis base like fluoride, combined with the Sn-rich environment, make SnF_2 a highly suitable additive for processing tin halide perovskites.

5.2 Experimental Details

Solution Preparation

1 M FASnI$_3$ perovskite precursor solutions were prepared by adding in 1:1 stoichiometry the corresponding volume to FAI powder from a stock 1.2 M solution of SnI$_2$ in DMSO and DMF. SnX$_2$-containing (X = F, Cl, Br, I) solutions were prepared by adding the corresponding volume of the 1 M FASnI$_3$ solution to the SnX$_2$ powder, according to its molar percentage (i.e. 5 %, 10 % and 20 % for F and 10 % for Cl, Br and I). Illustrative CsF- and NaF-containing 1 M FASnI$_3$ solutions in DMSO were prepared by saturating the precursor solution with the corresponding powder. The rest of the solutions were prepared by simply dissolving the powders in DMSO close to their saturation level (i.e. SnF$_2$, SnCl$_2$, SnBr$_2$, SnF$_4$, SnCl$_4$, SnBr$_4$ and SnI$_4$ at 0.5 M). SnF$_4$ solution was heated at 80 °C for 1 min to promote dissolution. If presenting precipitates, solutions were filtered before their characterization.

Thermal Ageing

The thermal stress of the solution was performed at 100 °C for 3 h. We took pictures before and after the ageing treatment.

Device fabrication

Patterned indium tin oxide (ITO) glass substrates (25x25 mm, resistivity = 15 Ω sq^{-1}, nominal ITO thickness = 150 nm, patterned by Automatic Research GmbH) were cleaned sequentially for 15 min with a 2 % Mucasol solution in water (Schülke), water, Acetone, and Isopropanol at ~ 40 °C in an ultrasonic bath. After the substrates were dried with N$_2$ flow, they were treated in a UV-ozone cleaner for 30 min. A PEDOT:PSS solution (180 μL) was spin-coated on FTO substrates at 4500 rpm for 45 s, followed by annealing at 150 °C for 10 min in air. Before use, PEDOT:PSS dispersion was filtered with 0.45 μm PVDF filter. The substrates were transferred into a N$_2$-filled glovebox, and from here the rest of the processing and measuring was carried out in inert conditions, avoiding all possible contact of the samples and devices with air. 100 μL of perovskite precursor were spin-coated on ITO/PEDOT:PSS substrates at 5000 rpm for 70 s with a

ramp of 1000 rpm s^{-1}. After 50 s, 200 μL of chlorobenzene as antisolvent were dripped onto the perovskite film. The substrates were quickly transferred to a hot plate with a program controller for 10 min at 100 °C. Finally, C_{60} (23 nm), BCP (8 nm) and Ag (100 nm) were thermally evaporated and deposited sequentially on ITO/PEDOT:PSS/perovskite layer in a MBRAUN ProVap 3G at a base pressure of 10^{-6} mbar. Ag was thermally evaporated through a shadow mask, where the overlap of the ITO with the Ag stripe defined an active area of 0.16 cm^2.

Current Density−Voltage Measurement

The J-V measurement is done with 1 sun equivalent illumination from an Oriel LCS100 class ABB solar simulator in an inert atmosphere without cooling. The lamp is calibrated with a Si 1 cm^2 diode certified by Fraunhofer ISE.

Scanning electron microscopy, SEM

SEM images were recorded using a Hitachi S4100 or ZEISS Auriga 60 at 5 kV acceleration voltage and 10k and 30k magnification.

Grazing Incident X-ray Diffraction, GIXRD

The measurements were conducted in the Bruker AXS D8 ADVANCE X-ray diffractometer (multipurpose diffractometer) and Bruker AXS DIFFRAC.SUITE software, using grazing incidence geometry. Samples were kept in nitrogen atmosphere using half-spherical domes to avoid air oxidation. XRD pattern is collected with a step size of 0.01 degree, for 2 seconds each step.

Small-Angle X-Ray Scattering, SAXS

The SAXS measurement was performed using synchrotron radiation at the four crystal monochromator X-ray beamline in the laboratory of PTB (Physikalisch-Technische Bundesanstalt) at BESSYII.[158] The SAXS instrument of HZB contains an adjustable about 3 m long support structure with a long edge-welded bellow system to enable the

changing of the sample to detector distance.[159] The 2D scattering images were collected by a windowless Dectris 1M PILATUS2 in-vacuum hybrid-pixel detector. The measurements were carried out at two different distances (0.8 m and 3.7 m) at photon energies of 10 keV and 8 keV, respectively. X-ray energies and sample to detector distances are chosen to get the maximum possible q-range, given the comparably low sample transmission. Thus, a q-range from 0.05 nm^{-1} to 8.5 nm^{-1} was covered (size range of 125.6 nm to 0.74 nm in real space). The precursor solutions were measured with an acquisition time of 600 s with three repetitions for the short distance and long distance to achieve good quality data and to monitor unwanted but possible changes of the specimen over time (which can therefore be safely excluded). Due to the low transmittance of the lead containing precursor solutions, especially thin (0.1 mm), rectangular borosilicate cuvettes (with a wall thickness of 0.1 mm) purchased from CM Scientific, UK were used. The total flux on the sample has been determined for each energy using a low-scatter pinhole of germanium 500 μm in diameter. For the long distance (3.7 m) at 8 keV, we indicated $4.8x10^9$ photons/s and $2.6x10^9$ photons/s for the short distance (0.8 m) at 10 keV.

Data processing: For data reduction and radial averaging to the 1D scattering pattern the BerSAS software was used, an advanced version of the BerSAS software[157] applicable for SAXS and SANS. All SAXS curves of the investigated samples were fitted with the program SASfit[140]. A structure model that includes a spherical form factor and a hard-sphere structure factor was chosen to fit all sample scattering curves to get a general idea of the order of magnitude. The herein investigated particles were considered as hard spheres. Thereby, these particles are assumed as incompressible, resulting in fixed radii for each particle and an infinite repulsive force at a specific interparticular separation. The hard spheres model neglects attractive forces but describes various colloids in organic solvents reasonably well.[163,164,240] We used the monodisperse Percus-Yevick approximation for hard spheres to fit the interaction of the analyzed colloidal particles.[165,240]

Hard X-ray Photoelectron Spectroscopy, HAXPES

HAXPES measurements were carried out at the HiKE endstation located at the BESSYII KMC-1 beamline at HZB.[10,11] The HiKE endstation is equipped with a Scienta R4000

electron analyzer, and excitation energies of 2003 eV (referred to as "2 keV") and 6009 eV (referred to as "6 keV") were employed, using the 1st and 3rd orders of the Si(111) crystal pair of the double crystal monochromator. To prevent beam damage effects on the samples, measurements were conducted with a beam-attenuating (100 μm) Be filter,[241] which reduces the photon flux of the 1st order light to 25 % of the original while transmitting >90 % of the 3rd order photons. The binding energy (BE) scales of the HAXPES measurements were calibrated by measuring the Au 4f energy region of a clean Au foil in electrical contact with the (grounded) sample and setting the BE of the Au $4f_{7/2}$ line to 84.0 eV. The pressure in the endstation's analysis chamber during the HAXPES measurements remained $<1 \times 10^{-8}$ mbar. To prevent/minimize exposure to ambient conditions, samples were mounted and sealed inside a N_2-filled glovebox for transport before introduction into the HiKE endstation system. The HAXPES probing depth is an exponential distribution governed by the inelastic mean free path (IMFP) of the probed photoelectrons. Regardless of excitation energy, the strongest spectral contribution comes from the sample's surface, and with 63 % (i.e., 1/e) of the signal coming from within the first IMFP. For the Sn 4d shallow core levels, measurements using 2 keV and 6 keV have inelastic mean free path (IMFP) values of ≈4 nm and ≈10 nm, respectively.[242,243] Probing the Sn 4d shallow core levels, which have a narrower line width than the more frequently investigated Sn 3d core levels, was preferred, as spectral contributions of Sn-related chemical species showing only minor differences in chemical shift can be better resolved.

Liquid-state Nuclear Magnetic Resonance, ^{119}Sn-NMR and ^{1}H-NMR

Liquid-state ^{119}Sn-NMR: The spectra were all acquired on a Bruker AVII 400 MHz or Bruker AVIII 500 MHz equipped with room-temperature TBO or BBO-probe heads, respectively. Typically, a sweep width of 504.3 ppm was used, and 64k points were acquired, resulting in a total acquisition time of 435.81 ms. The center frequency had to be adjusted from sample to sample in order to detect the desired signal. Therefore, a full scan of the possible shift range was acquired (1000 ppm to -3000 ppm) on new samples. We used a 30 ° pulse to minimize the recycle delay down to 2 s. The number of scans thus ranged from 128 for very concentrated samples to 16k scans for very dilute samples.

The spectra presented differences in the signal-to-noise ratio, thus the higher noise in some spectral baselines, particularly when zooming in to show the SnI_4 signal more clearly. All existing signals in all spectra were identified and pointed out.

Liquid-state ^{1}H-NMR: All other spectra were measured with standardized parameter sets from Bruker Topspin version 2.1 (AV400) and 3.0 (AV500). For non-deuterated solvents, a borosilicate capillary containing DMSO-d6 was introduced in the NMR tube to allow locking. The capillaries were 1.5 mm wide, 80 mm long and 0.01 mm wall-thick and were purchased from WJM-Glas/Müller GmbH.

5.3 Results & Discussion
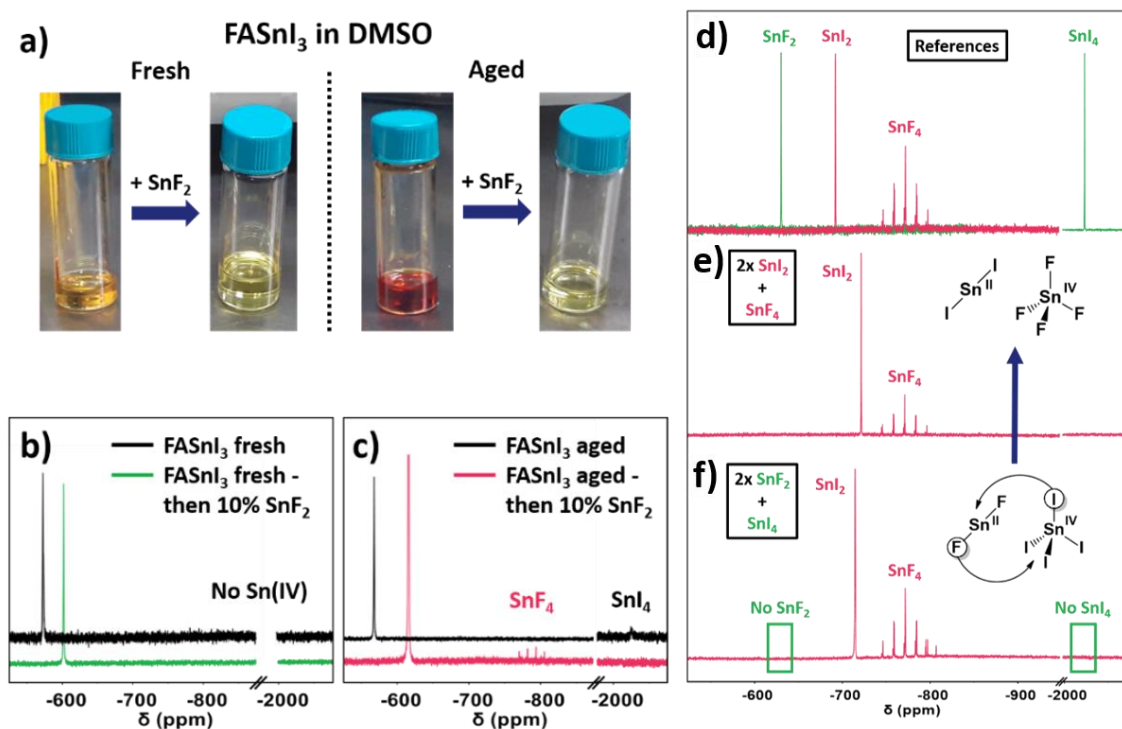
Figure 24. a) Pictures of fresh and aged FASnI$_3$ solutions in DMSO before and after the addition of SnF$_2$ in 10 mol%; the respective ^{119}Sn-NMR spectra of b) fresh and c) aged solutions; d) ^{119}Sn-NMR spectra of SnF$_2$, SnI$_2$, SnF$_4$ and SnI$_4$ in DMSO. Further information about solution preparation in Figure S5.3. ^{119}Sn-NMR spectra and solution pictures of the mixing of e) 2x SnI$_2$ and SnF$_4$ and f) 2x SnF$_2$ and SnI$_4$. The signal magnification was adapted accordingly for illustrative purposes.

Previous works concluded that SnF$_2$ could reduce the Sn(IV) content in solutions and films.[19,237] However, the redox activity cannot explain the multiple effects of SnF$_2$ in ASnX$_3$ perovskites entirely. Therefore, we postulated that SnF$_2$ must be involved in a different type of chemical reaction. In the early stages of tin halide perovskites development, it was thought that a yellow color for the solution implied the elimination of Sn(IV) through its reduction by SnF$_2$.[235] Using NMR spectroscopy, we uncover that Sn(IV) and SnF$_2$ do not undergo a redox reaction, but a simple ligand exchange reaction, producing colorless SnF$_4$ in solution. In this regard, we prepared FASnI$_3$ precursors solutions with and without SnF$_2$ and Sn(IV) to investigate their signature chemistry. ^{119}Sn-NMR is sensitive to Sn nuclei in different electronic environments, identifying of the Sn species in the solution, including other oxidation states of the same nucleus.

Figure 24a depicts the change in color from orange to the pale yellow of a 1M FASnI$_3$ solution in DMSO after the addition of SnF$_2$. Following the same method, we added SnF$_2$ to a Sn(IV)-containing solution after being aged by heating at 100 °C for 3 h.

80

M. I. Saidaminov *et al.* and we recently described that this thermal treatment promotes Sn(II) oxidation in DMSO solutions.[132,219] The color of the aged solution goes from an intense red to a pale yellow to that of the fresh sample. We know that certain content of Sn(IV) is present for the aged one, unlike the fresh solution. Still, the color after SnF_2 for the aged solution is the same as for the fresh solution, suggesting that the characteristics and species in the solution are changing, no matter the Sn(IV) content.

^{119}Sn-NMR of the fresh solution indicates neither elimination nor formation of Sn(IV), even though its color changes to pale yellow (**Figure 24b**). However, we observe the Sn(II) shielding resulting in a chemical shift change from -574 ppm to -604 ppm. Regarding the Sn(II) species (SnI_2 and SnF_2), they cannot be differentiated in solution, as they show up in a single signal belonging to the average electronic environment of Sn(II) in solution. In this sense, the addition of increasing amounts of SnF_2 shifts the Sn(II) peak to lower chemical shift values in a fairly linear manner, as we show in **Figure S5.2**. In contrast to the fresh solution, the aged $FASnI_3$ solution showed the expected SnI_4 signal at -2025 ppm. After adding SnF_2, this peak disappeared, and a new quintuplet rose at -770 ppm (**Figure 24c**). To identify the newly formed species, we measured solutions in DMSO of SnI_2, SnI_4, SnF_2 and SnF_4 by ^{119}Sn-NMR (**Figure 24d**), indicating that the species corresponds to SnF_4. This result, therefore, implies that SnF_2 cannot reduce Sn(IV) from an oxidized sample. Instead, it coordinates Sn(IV) via a ligand exchange reaction between the fluorides from Sn(II)F_2 and the iodides from oxidized Sn(IV)I_4:

$$Sn(IV)I_4 + 2\ Sn(II)F_2 \rightarrow Sn(IV)F_4 + 2\ Sn(II)I_2$$
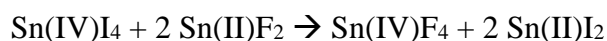
As shown in **Figure 24e**, a colorless solution comprising SnI_2 and SnF_4 presented both mixed species' signals in NMR. However, mixing SnF_2 and SnI_4, the resulting NMR species observed were SnI_2 and SnF_4. Consequently, the complexation selectivity of fluoride ions towards Sn(IV) is absolute (**Figure 24f**). This can be easily explained by the "hard and soft (Lewis) acids and bases" (*i.e.* HSAB theory) nature of the different solution species. Fluoride is a small, non-polarizable, electronegative anion that shows a stronger affinity for a cation of similar nature, *i.e.* Sn(IV), which is smaller and more electronegative than its reduced analogue Sn(II). This hard Lewis base character of fluoride anions was already applied in previous works on lead halide perovskites, owing to its ability to passivate vacancies due to their strong bonds with Pb(II).[244] In the present

case, we find that fluoride's role is connected to Sn(IV) complexation. Simultaneously, under-coordinated Sn(II) passivation in the thin film should not be excluded.

The only appearance so far of this species can be found in T. Nakamura and co-workers' work. The authors use an SnF_2-selective reducing agent to effectively generate Sn(0) nanoparticles to scavenge Sn(IV) from the solution.[245] Even though there is no particular discussion on the formation of SnF_4 and it does not affect their mechanism, the ^{119}Sn-NMR spectra provided in their work show the signal, also a multiplet, corresponding to SnF_4 at approximately -750 ppm when adding SnF_2 to a Sn(IV)-containing solution. This different multiplicity that the SnF_4 signal presents in ^{119}Sn-NMR compared to the rest of the Sn species can be explained by coupling between the Sn and halide nuclei. SnF_4 has four chemically equivalent ^{19}F-spins (each with spin 1/2) to couple with, which results in a perfect quintuplet as observed. In this sense, we would expect to observe a triplet for SnF_2. However, the four coordination sites are not saturated in SnF_2, and, thus, there is an exchange with other impurity-related compounds, such as water. T. Birchall and G. Dénès found the same behavior. They claimed that the missing coupling between ^{19}F and [119]Sn is due to the exchange between different hydrated species of SnF_2.[246] Our samples contain water since non-anhydrous DMSO-d6 was used as a solvent for the NMR spectroscopy experiments, therefore agreeing with the previously reported experiences. For other species, no splitting occurs since chloride, bromide, and iodide do not have NMR-active nuclei in significant amounts or with detectable line widths.

This affinity of fluorides towards Sn(IV) can have several important implications that may reduce Sn(IV) content in the final film. For instance, the strong preference for Sn(IV) means that fluorides could complex it as soon as it is generated, whether from O_2 in the environment or DMSO-driven oxidation.[23,132,219] In fact, one should think if SnF_2 would be as valuable for other solvents as in DMSO, as fluorides could be critical in sequestrating Sn(IV) as soon as it is oxidized by this solvent, making it less harmful. The conversion of SnI_4 into SnF_4 will also prevent the SnI_4-driven degradation pathways recently described by L. Lanzetta et al.[247] Furthermore, the selective complexation of Sn(IV) as SnF_4 may hinder its ability to form any perovskite-like complex in solution. It has been widely reported for SnF_2 that this material's excess tends to undergo phase separation.[124,230,235] Conclusively, if Sn(IV) is retained as SnF_4, it would be challenging to incorporate this form into the perovskite lattice. Instead, it would be displaced to grain boundaries or even removed from the film. As a result, the point defects resulting from

incorporated Sn(IV) in the perovskite lattice can be significantly reduced. To prove this, we compared the different Sn(IV) species' ability to coordinate with FAI by analyzing the ^{1}H-NMR of these solutions. **Figure S5.4** shows how all SnI$_2$ (FASnI$_3$), SnF$_4$ and SnI$_4$ cause the splitting of the FAI aminic protons, pointing out a certain degree of interaction between the species. However, the signals for the protons belonging to N and C are slightly shielded in the FASnI$_3$ solution (where the formation of perovskite adducts in solution occurs), whilst for the case of SnF$_4$, there is no shielding, suggesting that the interaction of SnF$_4$ species might have a lower affinity towards perovskite precursors. Moreover, the shift is very pronounced for SnI$_4$, which might imply strong coordination with FAI and an increased ability to get incorporated in the perovskite, resulting in adverse consequences for the photovoltaic properties of the films.
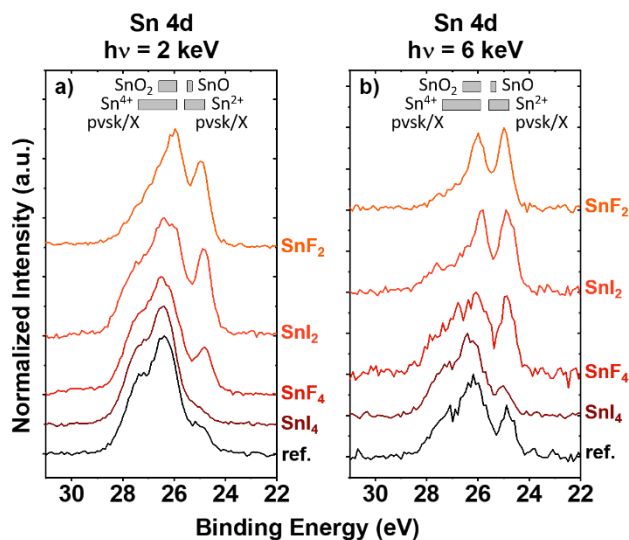
Figure 25. HAXPES spectra of Sn 4d core levels of FASnI$_3$ films prepared without ("ref.") and with 10 mol% of SnF$_2$, SnI$_2$ (excess), SnF$_4$ and SnI$_4$, measured using a) 2 keV and b) 6 keV excitation and normalized to maximum intensity (after background subtraction). The used additives are labelled next to the corresponding spectra. The grey-filled boxes denote the binding energy of Sn 4d$_{5/2}$ of Sn-based reference compounds reported in the literature.[237,248–250] "Sn^{2+} pvsk/X" stands for perovskite (tin halide salt) compounds with various ASnX$_3$ (SnX$_2$) compositions. "Sn^{4+} pvsk/X" stands for perovskite (organotin halide) compounds with various ASnX$_6$ (Ph$_3$SnX) compositions.

The impact of Sn(IV) complexation by fluoride in the preparation of FASnI$_3$ on the Sn chemical environment in the resulting films was investigated via HAXPES. 10 mol% of SnF$_2$, SnI$_2$, SnF$_4$ and SnI$_4$ was deliberately added to FASnI$_3$ perovskite precursor solutions. **Figure 25** presents HAXPES spectra of the Sn 4d energy region of FASnI3 samples prepared with and without various additives, measured with excitation energies of 2 keV and 6 keV, respectively. It is possible to vary the probing depths of the HAXPES measurements using different excitation energies, i.e. the 2 keV data is more surface-sensitive than the 6 keV data (see methods section). The spectra shown in

Figure 25 do not exhibit a line shape that resembles a single Sn $4d_{5/2} - 4d_{3/2}$ doublet peak (i.e., with a $3:2 = 4d_{5/2}:4d_{3/2}$ area ratio and a $4d_{5/2} - 4d_{3/2}$ spin-orbit separation of ≈ 1.1 eV);[237,251] this is a clear indication that spectral contributions from more than one Sn chemical species are detected. Overall, the Sn 4d spectra suggest substantial contributions in the binding energy (BE) regions (24.9 ± 0.1) eV and (26.2 ± 0.2) eV, corresponding to values reported in the literature for Sn $4d_{5/2}$ of Sn-based perovskite/halide and oxide reference compounds with Sn being in Sn^{2+} and Sn^{4+} environments, respectively.[237,248,250,252] Because the Sn 4d BE values of Sn^{2+} (SnO) and Sn^{4+} (SnO$_2$) oxide compounds are energetically overlapping with the respective Sn environments expected to be present in the sample set (i.e., FASnI$_3$ and the different Sn-based additives) and O-related lines were detected in the HAXPES measurements, the Sn 4d spectra in **Figure 25** likely contain Sn oxide derived spectral features and thus consist of more than two doublet peaks. Comparing the spectra in **Figure 25a** with the spectra in **Figure 25b** demonstrates that the high BE Sn^{4+}-related features are more prominent in the 2 keV measurements than in the 6 keV, which indicates an increased prevalence of the Sn^{4+} related species (in the form of SnO$_2$ or SnX$_4$) near the surface of samples than deeper within their bulk. However, significant differences in the line shape of the spectra for a given excitation set reveal pronounced changes in the Sn chemical environment of the investigated samples concerning the presence/absence and kind of additives during processing. The spectra of samples with additives containing Sn^{2+} or F$^-$ display a significant increase in the low BE Sn^{2+}-related signal. This finding seems to be in line with the NMR results described above, that capturing Sn(IV) in the form of fluorinated species prevents its incorporation in the films. However, the observed variability of properties at the surface of the samples associated with handling conditions of the Sn-based perovskite samples (as has been already reported,[237] and further discussed in 9.3, Supporting Information, see **Figure S5.5**) prevents the present interpretation of the HAXPES results from reaching further conclusions on the impact of individual additives with statistical certainty.

As depicted previously in **Figure 24a**, we attribute the color change of FASnI$_3$ in DMSO to the change in solution properties and not to the Sn(IV) content. Nevertheless, it is crucial to understand the underlying reasons for this change, as we expect it to exhibit a decisive influence on the crystallization dynamics.
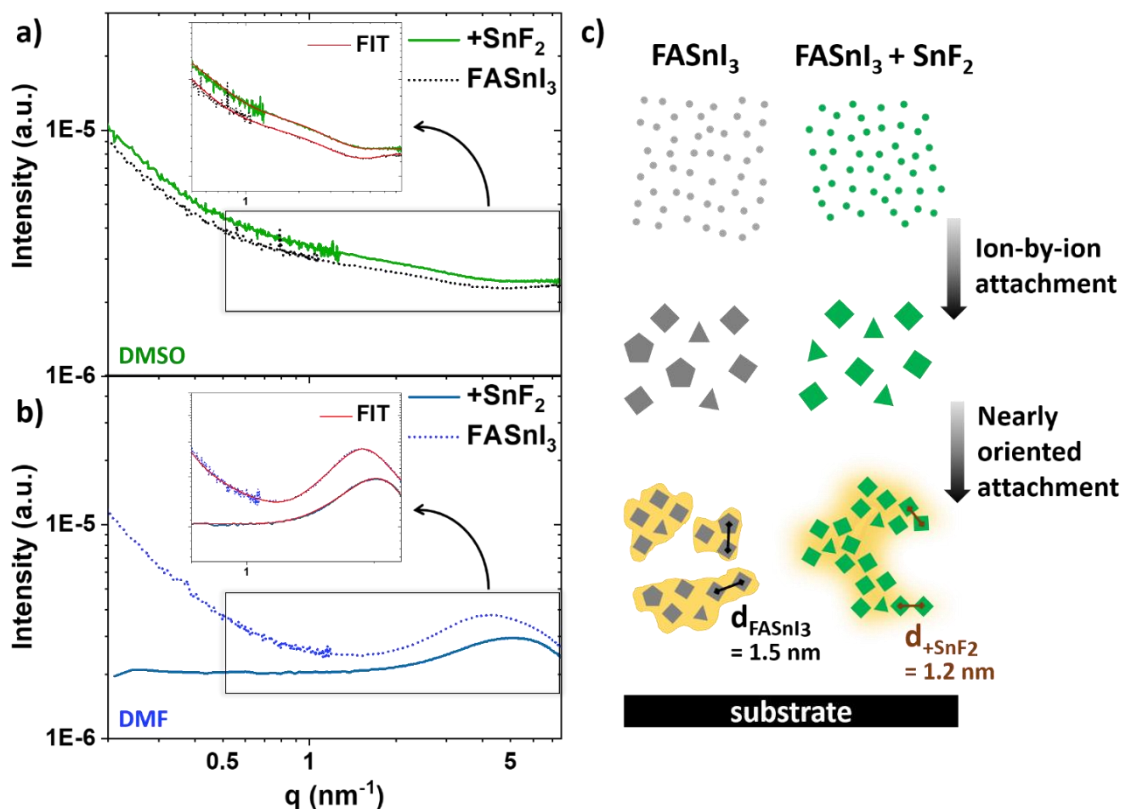
Figure 26. SAXS performed on different FASnI$_3$ precursor solutions. SAXS curves of FASnI$_3$ (dotted line) compared to FASnI$_3$ with SnF$_2$ addition (solid line) in a) DMSO and b) DMF, as well as the corresponding fit given in red in the magnified representations. c) Proposed nucleation and growth mechanism in FASnI$_3$ precursor solution affected by SnF$_2$ addition, where the different forms (triangle, quadrangle, pentagon) should schematically describe the potential variety of subunits.

Here, we perform transmission SAXS to reveal the effect of SnF$_2$ on the perovskite precursors in solution. A proposed nucleation mechanism indicates that SnF$_2$ promotes homogeneously distributed growth, yielding improvements in the overall crystal quality. Using the SAXS instrument at BESSYII at X-ray energies of 8 keV and 10 keV ($\Delta E/E = 2 \times 10^{-4}$), we cover a q-range from 0.05 nm^{-1} to 8.5 nm^{-1} (size range: 209.4 nm - 0.74 nm). **Figure 26a** compares the SAXS scattering curve of a plain FASnI$_3$ solution in DMSO with FASnI$_3$ containing SnF$_2$. At first sight, the comparison does not show significant variations.

Nevertheless, by applying a model fit using the software SASfit©,[140] which offers several different form and structure factors describing various shapes of particles and their interaction, small changes regarding the particle interplay in the high q-region can be observed. Here, however, interpretation requires particular precaution since we are already in the proximity of interatomic distances. The general behavior of the initial perovskite precursor stage is highly dependent on the specific solvent environment.

Literature shows that solvents with a lower donating number interact weakly, whereas stronger donating solvents interact strongly with the metal of a perovskite precursor solution.[253] Therefore, stronger donating solvents tend to hinder the iodide coordination of the metal. Since DMSO is known to be strongly donating and hence decelerates the perovskite crystallization process, we here include DMF with lower donating effect to investigate further the possible influence of SnF_2 on the early stages of crystallization. **Figure S5.6** shows the same effect on the color of SnF_2 in DMF as in DMSO, as proof that the same visual transformation occurred.

The evolution of a maximum in the SAXS scattering curve of $FASnI_3$ in DMF given in **Figure 26b** shows a clear difference compared to the scattering curve of pure $FASnI_3$ in DMSO. The maximum emerges based on a dominant structure factor, which evolves due to particle interaction. The mean spacing d between the mass centers of the individual interacting particles can be calculated as discussed by V. S. Raghuwanshi *et al.* using the magnitude of q at the peak maximum.[139] In the plain $FASnI_3$ solution in DMF, this results in a mean spacing d of approximately 1.5 nm. Adding SnF_2 to the solution leads to a shift of this peak maximum to higher q and, consequently, lower mean d spacing of 1.2 nm. Besides the shift of the maximum, also the slope at lower q-values disappears. The shallow negative slope for both DMF and DMSO solutions gives rise to the presence of larger structures with a broad size distribution (> 100 nm) in the solution. We propose that the larger sizes represent aggregates consisting of small interacting subunits formed by ion-to-ion attachment. We assign these subunits to particles or clusters in an average dimension of 0.4 nm observed in all scattering curves. In the DMF case, we assume that these aggregates form by nearly oriented attachment (OA), as described in the non-classical nucleation theory being pre-ordered arrangements (**Figure 26c**).[14,109,211] The well-pronounced structure factor peak can evidence this. It shows the recurring distance d between subunits, representing the average distance between the mass centers of the units and could be considered the tin-to-tin distance due to the high electron density of tin. A specific recurring distance d can also be noticed in the case of SnF_2 addition. However, there is no negative slope at low q-values assigned to larger higher-level structures. Therefore, we conclude that the total size distribution generally appears to be more homogeneous; the nearly OA with the recurring distance d of 1.2 nm might be considerably more extensive than in the plain $FASnI_3$ solution or

even of infinite size. Additionally, we performed several runs for every sample to prove no damage caused by the beam (**Figure S5.7**, 9.3).

Pre-ordered arrangements of subunits set the starting point for the further crystallization of a thin film on a substrate. The broad size distribution of comparable smaller aggregates might result in films including unordered pores or pinholes because solvent evaporation leaves holes between the pre-ordered totals. Instead, the more uniform size distribution due to a larger OA of the subunits supports homogeneously distributed crystal growth, a suitable substrate coverage and improved film morphology, precisely what is observed by SnF_2 addition in literature.[124,230,235] With the premise of the already advanced aggregation of elements in the DMF solvent, a similar mechanism during the late stages of enhanced crystallization may be expected for the case of DMSO. By applying pressure via spin-coating and solvent evaporation, the concentration of $FASnI_3$ in the solution increases. Following the evolution of SAXS scattering curves for $FASnI_3$ concentration series in DMF and DMSO, it suggests that a structure factor maximum is formed at higher concentrations in the case of DMSO comparable to the DMF solution (**Figure S5.8**, 9.3). In this sense, the observed behavior for DMF can be extrapolated to a more advanced stage of precursor formation for the DMSO precursor solution. Therefore, SnF_2 as an additive leads to an in total more homogeneous crystallization of the tin halide perovskite thin film, and, thus, a better morphology.

Regarding the change in solution color caused by SnF_2 addition, we speculate that fluoride modifies the coordination level of tin centers by iodide ions, hindering the formation of colorful, highly coordinated $[SnI_x]^{2-x}$ units. The fact that better morphology films are obtained through the pale yellow, SnF_2-containing solution points out that, with solution color as an indication, the properties of the existing formations in solution critically influence the crystallization dynamics of tin halide perovskites. This feature is currently underexplored for these materials and proves to be much more complex and sensitive than for their lead analogues due to its quite restricted processing conditions. Other SnX_2 (X= Cl, Br, I) and their influence on perovskite properties are also frequently discussed in the literature.[218,223,254] We further performed SAXS on $FASnI_3$ precursor solutions according to SnX_2 addition, given in **Figure S5.9**, to compare their respective functionality to the SnF_2 addition. Similar to the scattering curves shown in **Figure 26a**, no significant influence or difference between X can be noted. However, it should not be ruled out that they could have the same behavior difference as SnF_2 in other solvents

like DMSO and DMF. This confirms the need to investigate the strong dependence of additives and compositions used for tin halide perovskites. Finally, a scattering curve for the presence of Sn(IV) is given in the inset window in **Figure S5.9**, for which we measured an aged sample of FASnI$_3$. The effect of temperature-induced degradation of DMSO solutions on its properties seems relevant, confirming that we did not influence unexpected Sn(IV) content in FASnI$_3$ with or without SnX$_2$.

Although SAXS detected no difference for the different SnX$_2$ additives in DMSO solutions, they still caused a color change in a clear trend (**Figure 27a**). Both SnF$_2$ and SnCl$_2$ led to a similar yellow coloration of FASnI$_3$ solution, while SnBr$_2$ affected it more. This trend could mean that the colorful, highly coordinated $[SnI_x]^{2-x}$ iodidostannates were hindered more strongly as the halide X is a harder Lewis base. The fresh solutions were analyzed by ^{119}Sn-NMR (**Figure S5.10**, 9.3), although no notable difference was found except for the shielding effect from SnF$_2$, already discussed. In this sense, SnF$_2$ is the only SnX$_2$ additive shifting the FASnI$_3$ signal upfield, while SnCl$_2$ and SnBr$_2$ go slightly in the opposite direction. This effect correlates well with the chemical shifts in the different SnX$_2$-pure solutions in DMSO (**Figure S5.10**, 9.3), except for the SnI$_2$ case. Hence, the final Sn(II) signal position might be an average value of all Sn(II) species. After heating the solutions, we observed that the solution's darkening was negligible for chloride- and fluoride-containing solutions, which could be due to lower Sn(II) oxidation and more efficient Sn(IV) complexation by these anions. The heated solutions were measured by ^{119}Sn-NMR (**Figure 27a**), showing that the content of Sn(IV), all in the form of SnF$_4$, had been significantly reduced in comparison to SnF$_2$-free heated solution (**Figure 24a**). We hypothesize that fluoride could affect DMSO and Sn(II) environments, maybe through the modulation of $[SnI_x]^{2-x}$ adducts, making these two species less eager to undergo a redox reaction. Also, we observed that SnCl$_2$ addition had the same effect as SnF$_2$, leading to both reduction of the oxidation and the selective complexation of Sn(IV) through the formation of SnCl$_4$ (**Figure 27c**). These results prove that hard Lewis bases like chloride and fluoride can block the formation of Sn(IV) in the solution and their introduction into the perovskite film through two different mechanisms: complexation of Sn(IV) and antioxidative character. Our findings agree with previous reports on reducing Sn(IV) by adding SnF$_2$[231,235,237] SnCl$_2$[223] and suggest that many of the other additives employed in literature for tin halide perovskites may work in the same fashion.
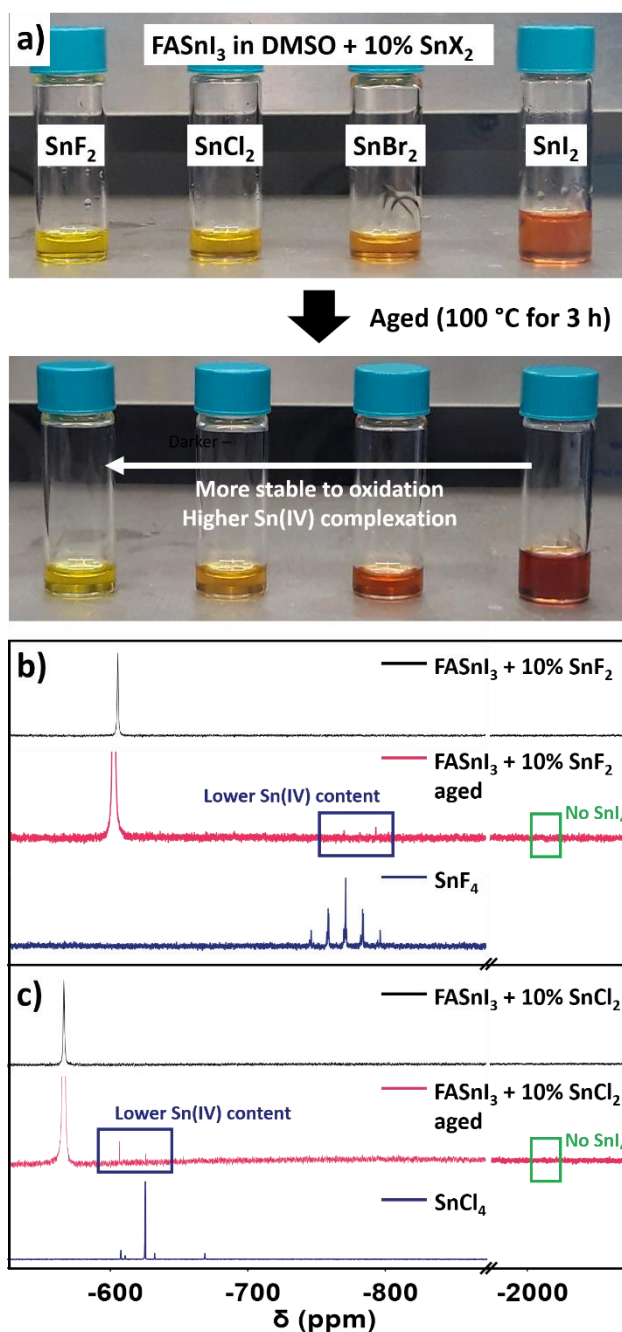
Figure 27. a) Fresh and aged solutions of FASnI$_3$ in DMSO with 10% SnF$_2$, SnCl$_2$, SnBr$_2$ and SnI$_2$. An arrow points out the difference in darkening as an effect of the ageing treatment. ^{119}Sn-NMR spectra of b) 10 % SnF$_2$- and c) 10 % SnCl$_2$-containing FASnI$_3$ solution before and after being aged. SnF$_4$ and SnCl$_4$ solutions spectra are added as indicative of the species formed under the ageing process.

To confirm that fluoride was responsible for these changes in solution, we prepared FASnI$_3$ solutions containing other fluoride-based compounds. Unfortunately, other common species (i.e. CsF and NaF) had limited solubility in common solvents. Therefore, we saturate the FASnI$_3$ solution below a 5 % molar ratio (**Figure S5.12**, 9.3). Even though the concentration was lower than for SnF$_2$, we observed the exact change in color from orange to pale yellow, potentially affecting perovskite subunits in solution

in the same fashion. Similarly, these solutions experienced no darkening of solutions aged at 100 °C for 3 h in different conditions, proving the complexation of Sn(IV) in the form of SnF_4. Even though these particular additives may not be directly implementable due to the strong influence that Cs^+ and Na^+ cations can have in the perovskite solar cells processing and performance, these results confirm the universality of the working principle for fluoride-based compounds. Furthermore, they suggest that SnF_2 additive may be eventually replaceable by other fluoride-based species if applied in the right conditions.

To complete the study, we wanted to investigate how these changes in perovskite solution properties affect the thin film formation and the corresponding solar cells performance. We fabricated pristine $FASnI_3$ films and $FASnI_3$ films with 10 % FAI excess, 10 % SnI_2, $SnBr_2$, $SnCl_2$ and SnF_2. The FAI excess was included as parameter to study both stoichiometry sides of $FASnI_3$. While there was no notable change in the X-ray diffraction patterns (**Figure S5.13**, 9.3), the scanning electron microscopy (SEM) results offered some differences among samples (**Figure S5.14**, 9.3). The sample with 10 % SnI_2 excess was the only one showing a high density of extensive pinholes. In contrast, the film with 10 % SnF_2 was the most homogeneous one, free of pinholes and other minor irregularities that are present in the rest of the films, agreeing with previous papers that used SnF_2 on its beneficial effect on morphology.[124,230,235]

There is an evident change in the resulting grain size with the changing halide element (**Figure S5.15**, 9.3). Fluoride led to the smallest average grain size (568 nm) compared to chloride (629 nm) and bromide (623 nm). These results are orthogonal to those reported previously, where fluoride[124] and chloride[225] were said to increase the perovskite crystals' grain size. However, tin halide perovskites' sensitive nature implies that significant changes can be expected from minor modifications in the perovskite composition or processing. Therefore, the effect of halides introduction can vary from study to study. Also, stoichiometry in pure $FASnI_3$ perovskite strongly affects the pinhole density and the average grain size. The largest size was found for equimolar $FASnI_3$ (695 nm), which went down when increasing or decreasing the SnI_2 ratio (647 nm and 568 nm, respectively). Moreover, SnF_2 addition impacts the size distribution, which is significantly narrowed to plain $FASnI_3$ thin film. These observations agree with the results by SAXS, assuming that a uniformly nearly OA in solution leads to a more homogeneous distribution of the grain sizes in the film.

We then used these films for solar cells to investigate any possible trends between additives and performance. In this sense, adding a small portion of tin halides to FASnI$_3$ solutions seems beneficial for the device performance, showing some positive trend when moving to lower size halides (**Figure S5.16**, 9.3). Though it appears that smaller halides – harder Lewis bases – work better by having a more decisive influence in the processing, chloride was the exception. Even though NMR and SAXS found SnCl$_2$ to have very similar behavior to SnF$_2$, the resulting devices yielded no efficiency, suggesting that chloride brings other factors into play. Previous works point out how chloride can be incorporated in the lattice and its tendency to form massive aggregates,[224,225] making its application not as trivial as SnF$_2$ and requiring a more careful optimization. We suspect SnCl$_2$ could mimic SnF$_2$ to some extent in these solutions if the processing conditions are adjusted accordingly. It is also worth noting the slight improvement in efficiency produced just by using a 1,1:1 SnI$_2$:FAI stoichiometry (i.e. 10 % SnI$_2$ excess), despite the content of irregularly sized pores (**Figure S5.14**, 9.3). This matches well with the results in previous works,[23,255] proving the importance of providing a Sn-rich environment in the film.

5.4 Conclusion

SnF$_2$ is a widely used additive for tin and lead/tin halide perovskites, systematically showing the same beneficial effects in all reported studies: perovskite films with lower Sn(IV) content and improved morphology. We uncovered the different roles of fluoride in SnF$_2$ on Sn(IV) complexation and colloidal arrangement in the precursor solution. By studying the fluoride chemistry in perovskite solutions and films with different complementary techniques, we demonstrated that the fluoride in SnF$_2$ has a critical role in reducing Sn(IV) content in the precursor solution and the final perovskite film. We showed by NMR the selective complexation of Sn(IV) in the form of SnF$_4$, which HAXPES revealed a lower tendency to get introduced in the film than SnI$_4$. Moreover, we showed how the introduction of SnF$_2$ in perovskite solutions increases their stability against the oxidation caused by DMSO. This antioxidative character was also found for SnCl$_2$, meaning that many other reported additives for tin halide perovskites may also block Sn(II) oxidation by simple tuning of solution properties. Apart from reducing Sn(IV) content in the thin film, SAXS measurements on the related precursor solutions evidenced that fluoride alters the essential formation of pre-organized perovskite clusters. We identified an advanced colloidal arrangement in DMF compared to the DMSO solutions that are notably influenced by the addition of SnF$_2$. We assigned this arrangement to an advanced nucleation process in DMF compared to DMSO. Finally, based on our findings, we proposed a nucleation mechanism that occurs in solution and is affected by the SnF$_2$ addition resulting in improved overall crystal quality. In this sense, the effect of SnF$_2$ on the film processing will be strongly determined by the environment in which it is applied (i.e. solvent, perovskite composition).

Consequently, there is an immediate need to fundamentally understand and optimize solution properties, their processing, and study the effect of additives. As we are doing in this study with the example of SnF$_2$ as pioneering work and an impulse for further research. Overall, we presented a complete comprehensive picture of the working mechanism of SnF$_2$ in tin halide perovskites processing and provided the community with the guidelines for finding new additives with specific chemical properties to complex Sn(IV) species and regulate the crystallization selectively.

5.5 Summary & Outlook

Tin based PSCs represent currently the most promising candidate for replacing the still common lead containing counterparts. Concerning this new emerging material, the fundamental understanding of processes is crucial to derive further insights to improve their properties systematically. Here, giving the example of SnF_2 addition, we have presented a widely spread approach used to engineer tin-based PSCs and push them to higher efficiency and better film morphology. We provide a concise image of the working mechanism highlighting the importance of a well comprehensive precursor solution characterization. Triggered by an evident observation of a change in color of the precursor solution, we uncover the selective mechanism of fluoride capturing $Sn(IV)$. The formation of SnF_4 prevents the incorporation of $Sn(IV)$ in the bulk of the perovskite thin film, which has been supported by HAXPES measurements proving the increase of $Sn(II)$ species in bulk as well as the higher probability of $Sn(IV)$ near the surface. Further characterization of the perovskite precursor solution reveal insights into the formation of the polycrystalline thin film via a nearly OA based on the non-classical nucleation theory. The addition of SnF_2 thereby initiates a narrower size distribution of formed dimensions in the solution, leading to more homogeneous crystal growth and thus better crystal quality.

Based on the findings presented in *Chapter 5*, we expect that the future development of tin halide perovskites will necessarily have to go through the fundamental understanding and optimization of solution properties. Processing and studying the effect of additives is mandatory for their targeted use, reflecting the study's fundamental approach within the example of SnF_2 as pioneering work and an impulse for future research. Overall, we presented a complete comprehensive picture of the working mechanism of SnF_2 in tin halide perovskites processing and provided the community with the guidelines for finding new additives with specific chemical properties to complex $Sn(IV)$ species and regulate the crystallization selectively.

This chapter will be discussed in further detail in *Chapter 6*.

6 Discussion & Perspective

The presented work highlights the importance of fundamental insights into the precursor chemistry of metal halide perovskites (MHP) initial solutions. Whereas in perovskite solar cell (PSC) research, the trial and error approach has traditionally led to a fast and successful evolution of their PV properties, it is becoming increasingly difficult to improve those effectively, especially concerning the PCE getting closer to the theoretical limits. Thus, we introduce a change of perspective to approach the further development differently. In doing so, we take a step back from the conventional PSC characterization towards the origins of the early stages of crystallization observable already in the precursor solution. We can provide detailed insights to explain mechanisms that result in particular MHP thin film properties. Knowing the mechanism behind those parameters can be used systematically to adapt the precursor properties to special needs, e.g. crystallization dependence on the fabrication process or unique photovoltaic (PV) properties controlled by compositional changes.

Thereby, within the scope of this thesis, we established the application of small-angle scattering (SAS) as a suitable characterization technique to analyze precursor solutions for the processing of PSCs. Especially in combination with other characterization techniques, we were able to provide a comprehensive picture of the MAPbI$_3$ perovskite precursor's chemistry. Beyond that, we applied the generated knowledge to more complex systems, including the addition of alkali cations and tin-based perovskites that can be considered as one future alternative MHP material to preserve a sustainable, lead-free environment. In the following, the major outcome of the individual studies is presented, followed by an overall discussion and perspective of the complete thesis.

Small-Angle Scattering Revealing Halide Perovskite Precursors

We present SAS as a direct nanostructural technique to characterize the colloidal nature in perovskite precursor dispersions. The existence of a dynamic colloidal network is proven, influencing the initial stages of crystallization. Based on prevailing forces in the solution (attractive and repulsive), we demonstrate the ordering of an optimal recurrent

distance of about 2 nm between colloidal particles. Those nanoparticles (NPs) of approximately 1 nm size are arranged to form superordinate quantities of about r = 2 μm.

The temperature dependency provided in **Figure 15** shows the reversible character of the actual dynamic colloidal arrangement and offers further information about the interactions between the NP subunits. In the case of the specimen under investigation, we observe that these arrangements already break down with comparably low energetic effort. In conclusion, the NPs of the superordinate formations must be connected via relatively weak forces, such as van der Waals forces or simple physical entanglement.[91] In 2019, S. Pratap *et al.* report the aggregate formation as one interpretation of their findings.[196] However, following the respective ISO definition (ISO/TS 80004-2:2008.), in the case of the $MAPbI_3$ precursor solution, we can instead assume to have dynamically formed agglomerates present with weakly bound subunits consisting of high-valent iodidoplumbates. This fact underlines the need to study fundamental interactions in solution since these determine the nucleation and growth mechanism of the material. In addition, external factors, such as changes in temperature and concentration critically affect the reproducibility of PSC fabrication. Therefore, we need to understand the underlying mechanism and effect of these factors in MHP precursor solutions, in order to address tailor-made needs of customers in the future. The work presented in *Chapter 3* serves as an initial fundament for rethinking the traditional research style in MHPs, proposing deeper understanding as a more effective method to gain better control on the system.

Colloidal stability - a Critical Factor Influencing the Perovskite Formation

Reproducibility and stability as crucial factors concerning the PSCs fabrication have been commonly addressed through compositional engineering of simple perovskite compositions like $MAPbI_3$ or $FAPbI_3$.[11,256,257] In this context, there has been an increased focus in recent years on the addition of alkali metal salts into the precursor solution of perovskites to enhance the stability and reproducibility of PSCs by achieving higher crystal quality of the thin film absorber.[17,18,257] In *Chapter 4* we elucidate this phenomena from the precursor perspective. We apply a well-established concept from colloid science, colloidal stability, and use it to the perovskite precursor systems. Covering a broad range of techniques, involving synchrotron radiation, we reveal the structural

formation of the colloidal subunits first addressed in *Chapter 3*. Supported by in-situ GIWAXS and SAXS, we can go beyond and explain the underlying working mechanism of the use of additional alkali cations towards thin film formation. The model of colloidal stability thereby provides the relevant parameter that defines why some precursor compositions form via a solvent-intermediate state, whereas this is suppressed when adding alkali cations.

The addition of alkali salts is just one proof of the applicability of the concept of colloidal stability. Moreover, the model provides further parameters to influence the respective forces acting in the precursor solution. Thus, it serves as an impulse to better develop and understand a diversity of mechanisms, such as solvent engineering[21,258] or the addition of larger molecules[259,260], which can slow down the crystallization process. We state that, especially when looking for suitable compositions for industrial PSC production in the future, it is essential to create knowledge on the working mechanism behind processes that are already applied but not well understood. Regarding future applications, mechanisms could also be pre-designed with a specific target to reduce trial and error and implement changes more effectively.

The Impact of Fluoride Chemistry on Tin-based Perovskites

Fluoride chemistry strongly improves the polycrystalline thin film formation process of tin halide perovskites through the addition of SnF_2. In *Chapter 5*, we evidenced that the fluoride anions selectively coordinate and remove detrimental Sn(IV), while positively influencing the colloidal properties in solution. The presented study describes the working mechanism of SnF_2 and highlights the importance of solution chemistry for controlling crystallization and Sn(II) oxidation in tin halide perovskites.

Considering the environmental and toxicological implications of lead, PSCs need to become lead-free to be considered as genuinely sustainable technology.[216] Tin-based perovskites are currently the frontrunners in the race to replace it, based on their close-to-ideal bandgap and reduced toxicity.[24,86,216] However, since the first reported values in 2014, those PSCs lag far behind their expectations. Besides, the PCE reached a plateau around 10-15 %, and lab-to-lab reproducibility remains the primary concern.[24,218] One promising way to tackle these challenges is to enhance the crystal quality and surface coverage of the absorber layer by controlling the fast crystallization of tin-based

perovskite systems.[218] In this sense, SnF$_2$ has shown substantial benefits in improving the morphology and crystal quality.[230]Previous studies confirm that a controlled crystallization process is the key to reach a good surface coverage.[8,9] The lab-to-lab reproducibility of the application of SnF$_2$ benefits made it the most widely employed additive for this kind of PSCs. Previous works provided insights into the characteristics of SnF$_2$-containing thin films, trying to shed light on its working mechanism.[238] However, the effect of SnF$_2$ on the precursor solution and hence the processing was missing.

In *Chapter 5*, we hence apply the knowledge gained from the precious studies to study the chemical nature of the tin-based perovskite precursor solution. Identifying the working mechanism of SnF$_2$ will promote the targeted application of additives, especially concerning newly emerging materials. In addition, the knowledge gained from the previous chapters will apply to SnF$_2$ and tin perovskite solutions, uncovering specific environmental implications like solvent and perovskite composition. Thus, this work is pioneering as it addresses the fundamental understanding of solution processes to optimize PSC fabrication. *Chapter 5* provides a comprehensive picture of the working mechanism of SnF$_2$, highlighting the solution chemistry and beyond. Based on this study, we offered initial guidelines to find further additives to systematically regulate the crystallization and handle the difficulty posed by Sn(IV).

Perspective

The remarkable progress in the fast-growing research field of PSCs has led to a constant striving for ever-improving efficiencies and PV properties. The increase of PCE within record time is unique. However, the research community is now experiencing a transformation to understand processes and mechanisms fundamentally. The PCE of lead-based PSCs is about to approach its theoretical limit, surpassing the 25 % mark already.[36,261,262] Based on this already fantastic value, other crucial factors towards future-oriented commercialization receive increasing attention. It moreover remains challenging to reproduce and implement the results on a large scale. Along with the potential for scalability of PSCs, the toxicity of lead and thus its replacement is of societal interest. To tackle the reproducibility of these high efficiencies and further

develop alternative materials without the toxic metal lead, such as tin-based perovskites, can only be achieved through a deeper understanding of the material's chemical nature.

Thus, using this thesis, we provide a comprehensive picture of the complex system of precursor chemistry and relevant parameters for process control, such as (I) environment impact based on concentration and temperature (II) the addition of counter ions to reduce the diffuse layer surrounding the NPs and (III) the targeted use of additives to selectively eliminate unwanted components to ensure a more homogeneous crystal growth.

All these parameters (I) to (III) (addressed in *Chapter 3* to *5*, respectively) can help to influence the crystallization process for future application selectively. Additionally, we expect to encourage the scientific community to think out of the box to find new processes according to the customer needs.
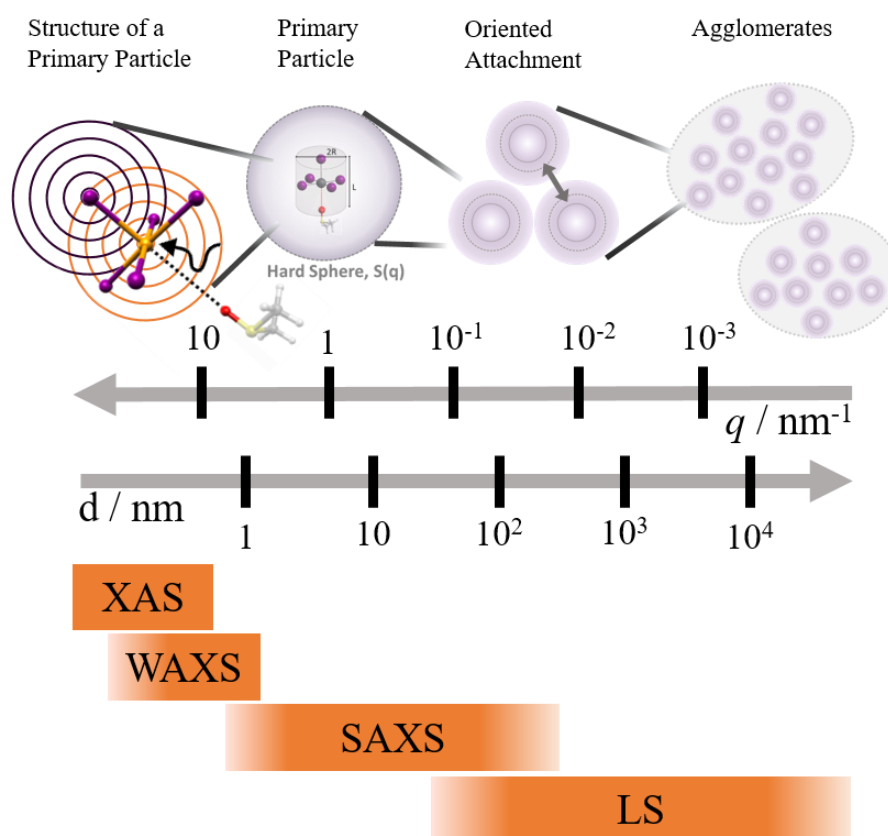
Figure 28. The interplay of complementary methodologies to provide a comprehensive picture of the complex precursor chemistry of MHP.

We have studied MHP precursors concerning the various influences across a various dimensions, combining complementary methodologies as depicted in **Figure 28**. We can provide structural insights on an atomic level about the crucial differences between simply dissolved PbI_2 solution and the actual $MAPbI_3$ precursor dispersion. Those NPs

interact strongly, due to the decay of electric potential, which the surrounding EDL and diffuse layer influence. Forming large islands in solution that can be considered as dynamically-formed agglomerates based on their comparably weak inter-particle interactions that are in the range of several micrometers in the case of MAPbI$_3$.

Further fundamental insights about the MAPbI$_3$ precursor systems could be achieved by a deeper analysis of the whole concentration range of the respective precursor mixture. To complete the understanding provided in this thesis focusing on concentrations used for direct PSC application, we extended the series presented in *Chapter 3* by measuring SAXS from particularly low concentrations. The preliminary data is provided in **Figure S6.1**. Interestingly we observe a negative slope evolving for concentrations below 0.1 mol L^{-1}. This might serve as an exciting starting point to further improve fundamental insights of the nuclei formation in MAPbI$_3$ precursor solution. However, further research and analytical methods would be needed to investigate the structures even before the actual formation of the NPs addressed within the scope of this work.

Furthermore, in a recently submitted concept paper, we point out the emerging need of replacing the solvent DMSO for tin-based PSCs since it results in the oxidation of Sn(II) to Sn(IV). Here we also see the need to apply the knowledge provided within the scope of this thesis to systematically search for alternatives that can still result in good morphology and surface coverage. Preliminary data of SAXS measured on tin-based precursor solutions on the base of different solvents is shown in **Figure S6.2**. It already provides insights into the strong impact of solvents and their donor ability on the colloidal chemistry of the precursor. However, further complementary data are needed to be able to make stronger statements.

In conclusion, we believe that this work identifies parameters and a new perspective required to meet the various challenges that lie ahead on the road towards the commercialization of PSCs. The effectiveness of the work is reflected by the numerous possibilities for application in subsequent projects.

7 Summary

Climate change leads to an urgency to promote alternative renewable energies and raise their accessibility to society. Solar energy generation represents a particular spotlight in this regard. In terms of advanced materials for solar cell applications, metal halide perovskite solar cells (PSCs) are at present an indispensable part of research for the future. Metal halide perovskites (MHPs) are crystalline semiconductors gaining increasing attention as low-cost, high-performance materials for optoelectronics. Their processing from solution at low temperature is compatible with the fast manufacturing of thin film devices, including solar cells and light-emitting diodes or photodetectors. Therefore, understanding the coordination chemistry in MHP precursor solutions would allow the vision of controlling the thin films crystallization, their material properties and final device performance. This thesis presents a change of perspective towards a fundamental understanding of the perovskite precursor solutions used for solar cell production. We elaborate on main parameters to systematically influence the precursor solution for long-term process control.

One main focus lies in applying a direct nanostructural technique to characterize the colloidal structure of perovskite in precursor solutions. Small-angle scattering is particularly adept at measuring nanoparticles in solution. We can apply this technique to perovskite precursor solutions in standard processing concentrations while avoiding beam damage and further sample treatment. We provide insights into the precursor's chemical nature while covering several perovskite compositions. We uncover structural insights about the precursor in the most common system of methylammonium lead iodide (MAPbI$_3$) and then expand the knowledge towards more complex applications, thereby addressing the influence of nanocompositional engineering using the example of alkali cation addition. We propose a detailed working mechanism on how the alkali cations act to suppress the formation of intermediate solvate phases and improve the quality of the thin film crystallization.

Furthermore, this work elucidates the crystallization process of a tin-based perovskite composition (FASnI$_3$) influenced by fluoride chemistry. The commonly added tin fluoride (SnF$_2$) captures selectively undesired oxidized Sn(IV) already in the precursor state in solution, which prevents its incorporation into the bulk crystal and reduces the

defect density of the material. In addition, SnF_2 leads to a more homogeneous crystal growing process, resulting in a better crystal quality of the thin film material.

Consequently, this study offers a detailed characterization of the complex system of the perovskite precursor chemistry and provides parameters relevant for process control. Hence, the knowledge presented serves as a basic building block with the potential to pave the way for the industrial implementation of perovskite photovoltaics.

8 References

1   H. C. de Coninck, *IPCC Special Report Global warming of 1.5°C*, 2018, vol. 291.

2   IRENA, Renewable Energy: A key climate solution,
     https://www.irena.org/climatechange/Renewable-Energy-Key-climate-solution.

3   O. Edenhofer, R. Pichs-Madruga, Y. Sokona, J. Minx, E. Farahani, S. Kadner, K. Seyboth,
     A. Adler, I. Baum, S. Brunner, P. Eickemeier, B. Kriemann, J. Savolainen, S. Schlömer, C.
     von Stechov and T. Zwickel, *Climate Change 2014: Mitigation of Climate Change*,
     Cambridge University Press, 2015, vol. 3.

4   L. Milliken, T. White and M. A. Fisher, Countering Climate Change With Renewable
     Energy Technologies, https://fas.org/blogs/sciencepolicy/countering-climate-change-
     with-renewable-energy-technologies/.

5   G. W. Crabtree and N. S. Lewis, *Phys. Today*, 2007, **60**, 37–42.

6   M. Thirugnanasambandam, S. Iniyan and R. Goic, *Renew. Sustain. Energy Rev.*, 2010,
     14, 312–322.

7   Y. Li, S. Witharana, H. Cao, M. Lasfargues, Y. Huang and Y. Ding, *Particuology*, 2014, **15**,
     39–44.

8   J. Kim, B. W. Park, J. Baek, J. S. Yun, H. W. Kwon, J. Seidel, H. Min, S. Coelho, S. Lim, S.
     Huang, K. Gaus, M. A. Green, T. J. Shin, A. W. Y. Ho-Baillie, M. G. Kim and S. Il Seok, *J.
     Am. Chem. Soc.*, 2020, **142**, 6251–6260.

9   J. Wang, Z. Gao, J. Yang, M. Lv, H. Chen, D. Xue, X. Meng and S. Yang, *Adv. Energy
     Mater.*, 2021, 2102131.

10   B. Phuong Nguyen, S. Dongguen, H. Ri Jung, J. Kim, T. Thi Thu Nguyen, S. Yoon, Y. Yi
     and W. Jo, *Sol. Energy*, 2019, **186**, 136–144.

11   L. Li, Y. Chen, Z. Liu, Q. Chen, X. Wang and H. Zhou, *Adv. Mater.*, 2016, **28**, 9862–9868.

12   G. S. Shin, S. Kim, Y. Zhang and N. Park, *Small*, 2019, **4**, 1900398.

13   Y. Zhou, O. S. Game, S. Pang and N. P. Padture, *J. Phys. Chem. Lett.*, 2015, **6**, 4827–
     4839.

14   J. J. De Yoreo, P. U. P. A. Gilbert, N. A. J. M. Sommerdijk, R. L. Penn, S. Whitelam, D.
     Joester, H. Zhang, J. D. Rimer, A. Navrotsky, J. F. Banfield, A. F. Wallace, F. M. Michel,
     F. C. Meldrum, H. Cölfen and P. M. Dove, *Science.*, 2015, **349**, aaa6760.

15   K. H. Stone, A. Gold-Parker, V. L. Pool, E. L. Unger, A. R. Bowring, M. D. McGehee, M. F.
     Toney and C. J. Tassone, *Nat. Commun.*, 2018, **9**, 3458.

16   M. Abdelsamie, T. Li, F. Babbe, J. Xu, Q. Han, V. Blum, C. M. Sutter-fella, D. B. Mitzi and
     M. F. Toney, *ACS Appl. Mater. Interfaces*, 2021, **13**, 13212–13225.

17   M. Saliba, M. Taisuke, S. Ji-Youn, D. Konrad, J.-P. Correa-Baena, K. N. Mohammad, S.
     M. Zakeeruddin, T. Wolfgang, A. Antonio, A. Hagfeldtd and G. Michael, *Energy Environ.*

Sci., 2016, **9**, 1853–2160.

18   M. Saliba, T. Matsui, K. Domanski, J.-Y. Seo, A. Ummadisingu, S. M. Zakeeruddin, J.-P. Correa-Baena, W. R. Tress, A. Abate, A. Hagfeldt and M. Grätzel, *Science.*, 2016, **354**, 206–210.

19   S. Gupta, D. Cahen and G. Hodes, *J. Phys. Chem. C*, 2018, **122**, 13926–13936.

20   P. K. Nayak, D. T. Moore, B. Wenger, S. Nayak, A. A. Haghighirad, A. Fineberg, N. K. Noel, O. G. Reid, G. Rumbles, P. Kukura, K. A. Vincent and H. J. Snaith, *Nat. Commun.*, 2016, **7**, 13303.

21   N. J. Jeon, J. H. Noh, Y. C. Kim, W. S. Yang, S. Ryu and S. Il Seok, *Nat. Mater.*, 2014, **13**, 897–903.

22   M. Qin, K. Tse, T. K. Lau, Y. Li, C. J. Su, G. Yang, J. Chen, J. Zhu, U. S. Jeng, G. Li, H. Chen and X. Lu, *Adv. Mater.*, 2019, **31**, 1901284.

23   D. Di Girolamo, J. Pascual, M. H. Aldamasy, Z. Iqbal, G. Li, E. Radicchi, M. Li, S.-H. Turren-Cruz, G. Nasti, A. Dallmann, F. De Angelis and A. Abate, *ACS Energy Lett.*, 2021, **6**, 959–968.

24   X. Jiang, Z. Zang, Y. Zhou, H. Li, Q. Wei and Z. Ning, *Accounts Mater. Res.*, 2021, **2**, 210–219.

25   H. S. Kim, A. Hagfeldt and N. G. Park, *Chem. Commun.*, 2019, **55**, 1192–1200.

26   N. Wang, Y. Zhou, M. Ju, H. F. Garces, T. Ding, S. Pang, X. C. Zeng, N. P. Padture and X. W. Sun, *Adv. Energy Mater.*, 2016, **6**, 1601130.

27   C. R. Kagan, D. B. Mitzi and C. D. Dimitrakopoulos, *Science.*, 1999, **286**, 945–947.

28   M. Era, T. Tsutsui and S. Saito, *Appl. Phys. Lett.*, 1995, **67**, 2436.

29   K. Chondroudis and D. B. Mitzi, *Chem. Mater.*, 1999, **11**, 3028–3030.

30   D. Mitzi, C. Feild, W. Harrison and A. Guloy, *Nature*, 1994, **369,** 467.

31   V. M. Goldschmidt, *Naturwissenschaften*, 1926, **14**, 477–485.

32   E. L. Da Silva, J. M. Skelton, S. C. Parker and A. Walsh, *Phys. Rev. B - Condens. Matter Mater. Phys.*, 2015, **91**, 144107.

33   S. S. Jerpoth, J. Iannello, E. A. Aboagye and K. M. Yenkie, *Clean Technol. Environ. Policy*, 2020, **22**, 1187–1198.

34   A. Kojima, K. Teshima, Y. Shirai and T. Miyasaka, *J. Am. Chem. Soc.*, 2009, **131**, 6050–6051.

35   M. M. Lee, J. Teuscher, T. Miyasaka, T. N. Murakami and H. J. Snaith, *Science.*, 2012, **338**, 643–648.

36   NREL, Best Research-Cell Efficiencies, https://www.nrel.gov/pv/cell-efficiency.html.

37   P. Roy, N. Kumar Sinha, S. Tiwari and A. Khare, *Sol. Energy*, 2020, **198**, 665–688.

38   I. Mathews, S. Sofia, E. Ma, J. Jean, H. S. Laine, S. C. Siah, T. Buonassisi and I. M. Peters, *Joule*, 2020, **4**, 822–839.

39   Y. Zhou, J. Chen, O. M. Bakr and H. T. Sun, *Chem. Mater.*, 2018, **30**, 6589–6613.

40   T. Umebayashi and K. Asai, *Phys. Rev. B*, 2003, **67**, 155405.

41   S. Olthof, *APL Mater.*, 2016, **4**, 091502.

42   E. L. Unger, L. Kegelmann, K. Suchan, D. Sörell, L. Korte and S. Albrecht, *J. Mater. Chem. A*, 2017, **5**, 11401–11409.

43   M. Jost, A. Al-Ashouri, B. Lipovsek, T. Bertram, R. Schlatmann, C. A. Kaufmann, M. Topic and S. Albrecht, in *2020 47th IEEE Photovoltaic Specialists Conference (PVSC)*, 2020, pp. 0763–0766.

44   A. Al-Ashouri, E. Köhnen, B. Li, A. Magomedov, H. Hempel, P. Caprioglio, J. A. Márquez, A. B. M. Vilches, E. Kasparavicius, J. A. Smith, N. Phung, D. Menzel, M. Grischek, L. Kegelmann, D. Skroblin, C. Gollwitzer, T. Malinauskas, M. Jošt, G. Matič, B. Rech, R. Schlatmann, M. Topič, L. Korte, A. Abate, B. Stannowski, D. Neher, M. Stolterfoht, T. Unold, V. Getautis and S. Albrecht, *Science.*, 2020, **370**, 1300–1309.

45   G. Zheng, C. Zhu, J. Ma, X. Zhang, G. Tang, R. Li, Y. Chen, L. Li, J. Hu, J. Hong, Q. Chen, X. Gao and H. Zhou, *Nat. Commun.*, 2018, **9**, 2793.

46   J. Schlipf and P. Müller-Buschbaum, *Adv. Energy Mater.*, 2017, **7**, 1700131.

47   S. Chen, X. Xiao, B. Chen, L. L. Kelly, J. Zhao, Y. Lin, M. F. Toney and J. Huang, *Sci. Adv.*, 2021, **7**, 26–29.

48   L. Meng, J. You and Y. Yang, *Nat. Commun.*, 2018, **9**, 5265.

49   Y. Rong, Y. Hu, A. Mei, H. Tan, M. I. Saidaminov, S. Il Seok, M. D. McGehee, E. H. Sargent and H. Han, *Science.*, 2018, **361**, eaat8235.

50   J. Jeong, M. Kim, J. Seo, H. Lu, P. Ahlawat, A. Mishra, Y. Yang, M. A. Hope, F. T. Eickemeyer, M. Kim, Y. J. Yoon, I. W. Choi, B. P. Darwich, S. J. Choi, Y. Jo, J. H. Lee, B. Walker, S. M. Zakeeruddin, L. Emsley, U. Rothlisberger, A. Hagfeldt, D. S. Kim, M. Grätzel and J. Y. Kim, *Nature*, 2021, **592**, 381–385.

51   E. Cohen and E. J. Lightfoot, in *Kirk-Othmer Encyclopedia of Chemical Technology*, American Cancer Society, 2011, pp. 1–68.

52   M. Saliba, J. P. Correa-Baena, C. M. Wolff, M. Stolterfoht, N. Phung, S. Albrecht, D. Neher and A. Abate, *Chem. Mater.*, 2018, **30**, 4193–4201.

53   S. Paek, P. Schouwink, E. N. Athanasopoulou, K. T. Cho, G. Grancini, Y. Lee, Y. Zhang, F. Stellacci, M. K. Nazeeruddin and P. Gao, *Chem. Mater.*, 2017, **29**, 3490–3498.

54   A. D. Taylor, Q. Sun, K. P. Goetz, Q. An, T. Schramm, Y. Hofstetter, M. Litterst, F. Paulus and Y. Vaynzof, *Nat. Commun.*, 2021, **12**, 1878.

55   W. Q. Wu, Q. Wang, Y. Fang, Y. Shao, S. Tang, Y. Deng, H. Lu, Y. Liu, T. Li, Z. Yang, A. Gruverman and J. Huang, *Nat. Commun.*, 2018, **9**, 1625.

56   J. Li, J. Dagar, O. Shargaieva, M. A. Flatken, H. Köbler, M. Fenske, C. Schultz, B. Stegemann, J. Just, D. M. Többens, A. Abate, R. Munir and E. Unger, *Adv. Energy Mater.*, 2021, **11**, 2003460.

57   J. B. Whitaker, D. H. Kim, B. W. Larson, F. Zhang, J. J. Berry, M. F. A. M. Van Hest and K. Zhu, *Sustain. Energy Fuels*, 2018, **2**, 2442–2449.

58   F. Mathies, E. J. W. List-Kratochvil and E. L. Unger, *Energy Technol.*, 2020, **8**, 1900991.

59   C. Liang, P. Li, H. Gu, Y. Zhang, F. Li, Y. Song, G. Shao, N. Mathews and G. Xing, *Sol. RRL*, 2018, **2**, 1700217.

60   F. Wang, Y. Cao, C. Chen, Q. Chen, X. Wu, X. Li, T. Qin and W. Huang, *Adv. Funct. Mater.*, 2018, **28**, 1803753.

61   T. Miyasaka, A. Kojima, K. Teshima and Y. Shirai, *J. Am. Chem. Soc.*, 2009, **131**, 6050–6051.

62   M. T. Weller, O. J. Weber, P. F. Henry, M. Di Pumpo and T. C. Hansen, *Chem. Commun.*, 2015, **51**, 4180–4183.

63   T. Baikie, Y. Fang, J. M. Kadro, M. Schreyer, F. Wei, S. G. Mhaisalkar, M. Graetzel and T. J. White, *J. Mater. Chem. A*, 2013, **1**, 5628–5641.

64   A. Franz, D. M. Többens and S. Schorr, *Cryst. Res. Technol.*, 2016, **51**, 534–540.

65   W. Geng, L. Zhang, Y. Zhang, W. Lau and L. Liu, *J. Phys. Chem. C*, 2014, **118**, 19565–19571.

66   Z. Shi, Y. Zhang, C. Cui, B. Li, W. Zhou, Z. Ning and Q. Mi, *Adv. Mater.*, 2017, **29**, 1701656.

67   M. W. Lufaso and P. M. Woodward, *Acta Crystallogr. Sect. B Struct. Sci.*, 2004, **60**, 10–20.

68   T. Oku, in *Solar Cells - New Approaches and Reviews*, 2015, pp. 77–101.

69   O. Bock and U. Müller, *Acta Crystallogr. Sect. B Struct. Sci.*, 2002, **58**, 594–606.

70   A. Alberti, I. Deretzis, G. Pellegrino, C. Bongiorno, E. Smecca, G. Mannino, F. Giannazzo, G. G. Condorelli, N. Sakai, T. Miyasaka, C. Spinella and A. La Magna, *ChemPhysChem*, 2015, **16**, 3064–3071.

71   P. Pistor, A. Ruiz, A. Cabot and V. Izquierdo-Roca, *Sci. Rep.*, 2016, **6**, 35973.

72   A. Mishra, Z. Ahmad, F. Touati, R. A. Shakoor and M. K. Nazeeruddin, *RSC Adv.*, 2019, **9**, 11589–11594.

73   M. Li, B. Li, G. Cao and J. Tian, *J. Mater. Chem. A*, 2017, **5**, 21313–21319.

74   B. Parida, S. Yoon, J. Ryu, S. Hayase, S. M. Jeong and D. W. Kang, *ACS Appl. Mater. Interfaces*, 2020, **12**, 22958–22970.

75   Y. Cui, S. Wang, C. Li, A. Wang, J. Ren, C. Yang, B. Chen, Z. Wang and F. Hao, *Green Chem.*, 2021, **23**, 3633–3641.

76   C. Li, J. Hu, S. Wang, J. Ren, B. Chen, T. Pan, X. Niu and F. Hao, *J. Phys. Chem. Lett.*, 2021, **12**, 4569–4575.

77   S. H. Turren-Cruz, A. Hagfeldt and M. Saliba, *Science.*, 2018, **362**, 449–453.

78   B. Conings, J. Drijkoningen, N. Gauquelin, A. Babayigit, J. D'Haen, L. D'Olieslaeger, A. Ethirajan, J. Verbeeck, J. Manca, E. Mosconi, F. De Angelis and H.-G. Boyen, *Adv. Energy Mater.*, 2015, **5**, 1500477.

79   J. W. Lee, D. H. Kim, H. S. Kim, S. W. Seo, S. M. Cho and N. G. Park, *Adv. Energy Mater.*, 2015, **5**, 1501310.

80   E. Smecca, Y. Numata, I. Deretzis, G. Pellegrino, S. Boninelli, T. Miyasaka, A. La Magna

and A. Alberti, *Phys. Chem. Chem. Phys.*, 2016, **18**, 13413–13422.

81 V. L. Pool, B. Dou, D. G. Van Campen, T. R. Klein-Stockert, F. S. Barnes, S. E. Shaheen, M. I. Ahmad, M. F. A. M. Van Hest and M. F. Toney, *Nat. Commun.*, 2017, **8**, 14075.

82 Y. Wang, T. Mahmoudi and Y. B. Hahn, *Adv. Energy Mater.*, 2020, **10**, 2000967.

83 X.-C. Zhao, D.-X. Wu, L.-J. Yang, J. Tang, G.-Z. Yue and P. Yang, *J. Nanosci. Nanotechnol.*, 2019, **20**, 1008–1012.

84 M. Imran, A. Saleem, N. A. Khan and A. H. Kamboh, *Phys. B Condens. Matter*, 2019, **572**, 011007.

85 J. Li, H.-L. Cao, W.-B. Jiao, Q. Wang, M. Wei, I. Cantone, J. Lü and A. Abate, *Nat. Commun.*, 2020, **11**, 310.

86 N. K. Noel, S. D. Stranks, A. Abate, C. Wehrenfennig, S. Guarnera, A. Haghighirad, A. Sadhanala, G. E. Eperon, S. K. Pathak, M. B. Johnston, A. Petrozza, M. Herz and H. J. Snaith, *Energy Environ. Sci.*, 2014, **7**, 3061–3068.

87 B. Bin Yu, Z. Chen, Y. Zhu, Y. Wang, B. Han, G. Chen, X. Zhang, Z. Du and Z. He, *Adv. Mater.*, 2021, **33**, 2102055.

88 P. C. Hiemenz and R. Rajagopalan, *Principles of Colloid and Surface Chemistry, revised and expanded*, CRC press, 2016.

89 J. Jeevanandam, A. Barhoum, Y. S. Chan, A. Dufresne and M. K. Danquah, *Beilstein J. Nanotechnol.*, 2018, **9**, 1050–1074.

90 BSI, *PAS 71:2011*, London, United Kingdom, 2011.

91 D. R. Boverhof, C. M. Bramante, J. H. Butala, S. F. Clancy, W. M. Lafranconi, J. West and S. C. Gordon, *Regul. Toxicol. Pharmacol.*, 2015, **73**, 137–150.

92 *ISO/TS 80004-2:2015*, 2015.

93 W. G. Kreyling, M. Semmler-Behnke and Q. Chaudhry, *Nano Today*, 2010, **5**, 165–168.

94 P. W. Atkins and J. De Paula, *Atkins' Physical chemistry*, 2006, vol. 94.

95 E. C. H. Ng, Y. K. Koh and C. C. Wong, in *Contemporary Physics*, 2012, vol. 24, pp. 25–73.

96 X. Liu, R. E. DeVor, S. G. Kapoor and K. F. Ehmann, *J. Manuf. Sci. Eng.*, 2004, **126**, 666–678.

97 C. A. Gray and H. Muranko, *J. Occup. Environ. Med.*, 2006, **48**, 1279–1290.

98 P. W. Voorhees, *J. Stat. Phys.*, 1985, **38**, 231–252.

99 I. M. Lifshitz and V. V. Slyozov, *J. Phys. Chem. Solids*, 1961, **19**, 35–50.

100 W. Ostwald, *Zeitschrift für Phys. Chemie*, 1900, **34U**, 495–503.

101 C. Wagner, *Z. Elektrochem.*, 1961, **65**, 581–591.

102 T. E. of E. Britannica, Nucleation, https://www.britannica.com/science/nucleation.

103 M. Volmer and A. Weber, *Zeitschrift für Phys. Chemie*, 1926, **119U**, 277–301.

104 D. Kashchiev, *Nucleation*, Elsevier, 2000.

105   V. G. Dubrovskii, *Nucleation theory and growth of nanostructures*, Springer, 2014.

106   R. Becker and W. Döring, *Natl. Advis. Comm. Astronaut. (NACA TM 1374)*, 1935, **24**, 719.

107   C. B. Whitehead, S. Özkar and R. G. Finke, *Chem. Mater.*, 2019, **31**, 7116–7132.

108   V. K. LaMer and R. H. Dinegar, *South. Med. J.*, 1950, **72**, 4847–4854.

109   M. Niederberger and H. Cölfen, *Phys. Chem. Chem. Phys.*, 2006, **8**, 3271–3287.

110   J. Polte, *CrystEngComm*, 2015, **17**, 6809–6830.

111   E. D. Bøjesen and B. B. Iversen, *CrystEngComm*, 2016, **18**, 8332–8353.

112   F. Wang, V. N. Richards, S. P. Shields and W. E. Buhro, *Chem. Mater.*, 2014, **26**, 5–21.

113   D. Tatchev, A. Hoell, M. Eichelbaum and K. Rademann, *Phys. Rev. Lett.*, 2011, **106**, 085702.

114   D. Gebauer and H. Cölfen, *Nano Today*, 2011, **6**, 564–584.

115   J. De Yoreo, *Nat. Mater.*, 2013, **12**, 284–285.

116   T. Palberg, *Curr. Opin. Colloid Interface Sci.*, 1997, **2**, 607–614.

117   D. Segets, R. Marczak, S. Schäfer, C. Paula, J. F. Gnichwitz, A. Hirsch and W. Peukert, *ACS Nano*, 2011, **5**, 4658–4669.

118   E. J. W. Verwey and J. T. G. Overbeek, *J. Colloid Sci.*, 1955, **10**, 224–225.

119   A. K. SenGupta and K. D. Papadopoulos, *J. Colloid Interface Sci.*, 1998, **203**, 345–353.

120   D. Schwahn, Y. Ma and H. Cölfen, *J. Phys. Chem. C*, 2007, **111**, 3224–3227.

121   M. Li, H. Schnablegger and S. Mann, *Nature*, 1999, **402**, 393–395.

122   H. X. Dang, K. Wang, M. Ghasemi, M. C. Tang, M. De Bastiani, E. Aydin, E. Dauzon, D. Barrit, J. Peng, D. M. Smilgies, S. De Wolf and A. Amassian, *Joule*, 2019, **3**, 1746–1764.

123   S. Pratap, F. Babbe, N. S. Barchi, Z. Yuan, T. Luong, Z. Haber, T. Bin Song, J. L. Slack, C. V. Stan, N. Tamura, C. M. Sutter-Fella and P. Müller-Buschbaum, *Nat. Commun.*, 2021, **12**, 5624.

124   Z. Zhao, F. Gu, Y. Li, W. Sun, S. Ye, H. Rao, Z. Liu, Z. Bian and C. Huang, *Adv. Sci.*, 2017, **4**, 1700204.

125   C. Ran, W. Gao, J. Li, J. Xi, L. Li, J. Dai, Y. Yang, X. Gao, H. Dong, B. Jiao, I. Spanopoulos, C. D. Malliakas, X. Hou, M. G. Kanatzidis and Z. Wu, *Joule*, 2019, **3**, 3072–3087.

126   T. Wu, D. Cui, X. Liu, X. Meng, Y. Wang, T. Noda, H. Segawa, X. Yang, Y. Zhang and L. Han, *Sol. RRL*, 2020, **4**, 2000240.

127   J. Y. Seo, T. Matsui, J. Luo, J. P. Correa-Baena, F. Giordano, M. Saliba, K. Schenk, A. Ummadisingu, K. Domanski, M. Hadadian, A. Hagfeldt, S. M. Zakeeruddin, U. Steiner, M. Grätzel and A. Abate, *Adv. Energy Mater.*, 2016, **6**, 1600767.

128   W. S. Yang, J. H. Noh, N. J. Jeon, Y. C. Kim, S. Ryu, J. Seo and S. Il Seok, *Science.*, 2015, **348**, 1234–1237.

129   S. Ito, S. Tanaka and H. Nishino, *J. Phys. Chem. Lett.*, 2015, **6**, 881–886.

130   W. Gao, C. Ran, J. Li, H. Dong and B. Jiao, *J. Phys. Chem. Lett.*, 2018, **9**, 6999–7006.

131   F. Gu, S. Ye, Z. Zhao, H. Rao, Z. Liu, Z. Bian and C. Huang, *Sol. RRL*, 2018, **2**, 1870217.

132   J. Pascual, G. Nasti, M. H. Aldamasy, J. A. Smith, M. Flatken, N. Phung, D. Di Girolamo, S.-H. Turren-Cruz, M. Li, A. Dallmann, R. Avolio and A. Abate, *Mater. Adv.*, 2020, **1**, 1066–1070.

133   M. Flatken, A. Hoell, R. Wendt, E. Härk, A. Dallmann, A. Prause, J. Pascual, E. Unger and A. Abate, *J. Mater. Chem. A*, 2021, **9**, 13477–13482.

134   O. Glatter and O. Kratky, *Small angle X-ray scattering*, Academic press, 1982.

135   B. O. Glatter and R. May, in *International Tables of Crystallography*, 2006, vol. C, pp. 89–112.

136   J. S. Higgins and H. C. Benoit, *Polymers and neutron scattering*, Clarendon Press, Oxford (United Kingdom), 8th edn., 1994, vol. 28.

137   M. Kerker, *The scattering of light and other electromagnetic radiation: physical chemistry: a series of monographs*, Academic press, 2013, vol. 16.

138   H. Schnablegger and Y. Singh, *The SAXS Guide*, Anton Paar GmbH, 2013.

139   V. S. Raghuwanshi, M. Ochmann, A. Hoell, F. Polzer and K. Rademann, *Langmuir*, 2014, **30**, 6038.

140   I. Breßler, J. Kohlbrecher and A. F. Thünemann, *J. Appl. Crystallogr.*, 2015, **48**, 1587–1598.

141   E. Di Cola, I. Grillo and S. Ristori, *Pharmaceutics*, 2016, **8**, 1–16.

142   J. Bergenholtz, J. Ulama and M. Zackrisson Oskolkova, *J. Appl. Cryst.*, 2016, **49**, 47–54.

143   Q. Van Le, J. B. Kim, S. Y. Kim, B. Lee and D. R. Lee, *J. Phys. Chem. Lett.*, 2017, **8**, 4140–4147.

144   S. Zhang, C. Yi, N. Wang, Y. Sun, W. Zou, Y. Wei, Y. Cao, Y. Miao, R. Li, Y. Yin, N. Zhao, J. Wang and W. Huang, *Adv. Mater.*, 2017, **29**, 1606600.

145   O. Shargaieva, L. Kuske, J. Rappich, E. L. Unger and N. H. Nickel, *Phys. Chem. Chem. Phys.*, 2020, **21**, 2327–2333.

146   N. K. Noel, M. Congiu, A. J. Ramadan, S. Fearn, D. P. McMeekin, J. B. Patel, M. B. Johnston, B. Wenger and H. J. Snaith, *Joule*, 2017, **1**, 328–343.

147   E. Radicchi, E. Mosconi, F. Elisei, F. Nunzi and F. De Angelis, *ACS Appl. Energy Mater.*, 2019, **2**, 3400–3409.

148   C. J. Dahlman, N. R. Venkatesan, P. T. Corona, R. M. Kennard, L. Mao, N. C. Smith, J. Zhang, R. Seshadri, M. E. Helgeson and M. L. Chabinyc, *ACS Nano*, 2020, **14**, 11294–11308.

149   B. Li, D. Binks, G. Cao and J. Tian, *Small*, 2019, **15**, 1903613.

150   N. Dutta, N. Noel and C. Arnold, *J. Phys. Chem. Lett.*, 2020, **11**, 5980–5986.

151   F. Qin, Z. Wang and Z. L. Wang, *ACS Nano*, 2016, **10**, 9787–9793.

152   P. A. Hassan, S. Rana and G. Verma, *Langmuir*, 2015, **31**, 3–12.

153   J. Stetefeld, S. A. McKenna and T. R. Patel, *Biophys. Rev.*, 2016, **8**, 409–427.

154   B. Li, M. Li, C. Fei, G. Cao and J. Tian, *J. Mater. Chem. A*, 2017, **5**, 24168–24177.

155   I. Drulyte, R. M. Johnson, E. L. Hesketh, D. L. Hurdiss, C. A. Scarff, S. A. Porav, N. A. Ranson, S. P. Muench and R. F. Thompson, *Acta Crystallogr. Sect. D Struct. Biol.*, 2018, **74**, 560–571.

156   U. Keiderling and A. Wiedenmann, *Phys. B Phys. Condens. Matter*, 1995, **213**–**214**, 895–897.

157   U. Keiderling, *Appl. Phys. A*, 2002, **74**, 1455–1457.

158   M. Krumrey and G. Ulm, *Nucl. Instruments Methods Phys. Res. Sect. A Accel. Spectrometers, Detect. Assoc. Equip.*, 2001, **467**, 1175–1178.

159   DE102006029449, 2007.

160   O. Kratky and G. Porod, *Acta Phys. Austriaca*, 1948, **2**, 133–147.

161   G. Porod, *Zeitschrift fur Naturforsch. A*, 1949, **4**, 401–414.

162   A. Vrij, J. W. Jansen, J. K. G. Dhont, C. Pathmamanoharan, M. M. Kops-Werkhoven and H. M. Fijnaut, *Faraday Discuss. Chem. Soc.*, 1983, **76**, 19–35.

163   D. Orsi, A. Fluerasu, A. Moussaïd, F. Zontone, L. Cristofolini and A. Madsen, *Phys. Rev. E 85*, 2012, **85**, 011402.

164   D. Frenkel and S. Auer, *Nature*, 2001, **409**, 1020–1023.

165   J. K. Percus and G. J. Yevick, *Phys. Rev.*, 1958, **110**, 1–13.

166   A. Vrij, *J. Chem. Phys.*, 1979, **3267**, 3267–3270.

167   L. A. Feigin and D. I. Svergun, *Structure analysis by small-angle X-ray and neutron scattering*, Springer, 1987, vol. 1.

168   R. Botet, S. Kwok and B. Cabane, *J. Appl. Crystallogr.*, 2020, **53**, 1570–1582.

169   B. Park and S. Il Seok, *Adv. Mater.*, 2019, **31**, 1805337.

170   N. Klein-Kedem, D. Cahen and G. Hodes, *Acc. Chem. Res.*, 2016, **49**, 347–354.

171   X. Hao, M. Chen, L. Wang, Z. Cao, Y. Li, S. Han, M. Zhang, K. Yu and J. Zeng, *Chem. Commun.*, 2020, **56**, 2031–2034.

172   A. J. Neukirch, I. I. Abate, L. Zhou, W. Nie, H. Tsai, L. Pedesseau, J. Even, J. J. Crochet, A. D. Mohite, C. Katan and S. Tretiak, *J. Phys. Chem. Lett.*, 2018, **9**, 7130–7136.

173   L. Zhou, C. Katan, W. Nie, H. Tsai, L. Pedesseau, J. J. Crochet, J. Even, A. D. Mohite, S. Tretiak and A. J. Neukirch, *J. Phys. Chem. Lett.*, 2019, **10**, 3516–3524.

174   R. F. Moral, L. G. Bonato, J. C. Germino, W. X. Coelho Oliveira, R. Kamat, J. Xu, C. J. Tassone, S. D. Stranks, M. F. Toney and A. F. Nogueira, *Chem. Mater.*, 2019, **31**, 9472–9479.

175   A. Sharenko, C. Mackeen, L. Jewell, F. Bridges and M. F. Toney, *Chem. Mater.*, 2017, **29**, 1315–1320.

176   E. Radicchi, A. Kachmar, E. Mosconi, B. Bizzarri, F. Nunzi and F. De Angelis, *J. Phys. Chem. Lett.*, 2020, **11**, 6139–6145.

177   D. J. Kubicki, D. Prochowicz, A. Hofstetter, S. M. Zakeeruddin, M. Grätzel and L. Emsley, *J. Am. Chem. Soc.*, 2017, **139**, 14173–14180.

178   M. Abdi-Jalebi, Z. Andaji-Garmaroudi, A. J. Pearson, G. Divitini, S. Cacovich, B. Philippe, H. Rensmo, C. Ducati, R. H. Friend and S. D. Stranks, *ACS Energy Lett.*, 2018, **3**, 2671–2678.

179   N. Park, M. Grätzel, T. Miyasaka, K. Zhu and K. Emery, *Nat. Energy*, 2016, **1**, 1–8.

180   M. I. Saidaminov, K. Williams, M. Wei, A. Johnston, R. Quintero-Bermudez, M. Vafaie, J. M. Pina, A. H. Proppe, Y. Hou, G. Walters, S. O. Kelley, W. A. Tisdale and E. H. Sargent, *Nat. Mater.*, 2020, **19**, 412–418.

181   N. Rolston, A. D. Printz, J. M. Tracy, H. C. Weerasinghe, D. Vak, L. J. Haur, A. Priyadarshi, N. Mathews, D. J. Slotcavage, M. D. McGehee, R. E. Kalan, K. Zielinski, R. L. Grimm, H. Tsai, W. Nie, A. D. Mohite, S. Gholipour, M. Saliba, M. Grätzel and R. H. Dauskardt, *Adv. Energy Mater.*, 2018, **8**, 1702116.

182   N. J. Jeon, J. H. Noh, W. S. Yang, Y. C. Kim, S. Ryu, J. Seo and S. Il Seok, *Nature*, 2015, **517**, 476–480.

183   D. Bi, W. Tress, M. I. Dar, P. Gao, J. Luo, C. Renevier, K. Schenk, A. Abate, F. Giordano, J. C. Baena, J. Decoppet, S. M. Zakeeruddin, M. K. Nazeeruddin, M. Grätzel and A. Hagfeldt, *Sci. Adv.*, 2016, **2**, e1501170.

184   R. G. Niemann, L. Gouda, J. Hu, S. Tirosh, R. Gottesman, P. J. Cameron and A. Zaban, *J. Mater. Chem. A*, 2016, **4**, 17819–17827.

185   M. Qin, H. Xue, H. Zhang, H. Hu, K. Liu, Y. Li, Z. Qin, J. Ma, H. Zhu, K. Yan, G. Fang, G. Li, U. S. Jeng, G. Brocks, S. Tao and X. Lu, *Adv. Mater.*, 2020, **32**, 2004630.

186   K. M. Boopathi, R. Mohan, T. Y. Huang, W. Budiawan, M. Y. Lin, C. H. Lee, K. C. Ho and C. W. Chu, *J. Mater. Chem. A*, 2016, **4**, 1591–1597.

187   T. Duong, H. K. Mulmudi, H. Shen, Y. L. Wu, C. Barugkin, Y. O. Mayon, H. T. Nguyen, D. Macdonald, J. Peng, M. Lockrey, W. Li, Y. B. Cheng, T. P. White, K. Weber and K. Catchpole, *Nano Energy*, 2016, **30**, 330–340.

188   Y. Hu, M. F. Aygüler, M. L. Petrus, T. Bein and P. Docampo, *ACS Energy Lett.*, 2017, **2**, 2212–2218.

189   P. Wang, J. Wang, X. Zhang, H. Wang, X. Cui, S. Yuan, H. Lu, L. Tu, Y. Zhan and L. Zheng, *J. Mater. Chem. A*, 2018, **6**, 15853–15858.

190   F. Hao, C. C. Stoumpos, Z. Liu, R. P. H. Chang and M. G. Kanatzidis, *J. Am. Chem. Soc.*, 2014, **136**, 16411–16419.

191   Y. Guo, K. Shoyama, W. Sato, Y. Matsuo, Y. Guo, K. Shoyama, W. Sato, Y. Matsuo, K. Inoue, K. Harano, C. Liu, H. Tanaka and E. Nakamura, *J. Am. Chem. Soc.*, 2015, **137**, 15907–15914.

192   W. Li, J. Fan, J. Li, Y. Mai and L. Wang, *J. Am. Chem. Soc.*, 2015, **137**, 10399–10405.

193   A. A. Petrov, I. P. Sokolova, N. A. Belich, G. S. Peters, P. V. Dorovatovskii, Y. V. Zubavichus, V. N. Khrustalev, A. V. Petrov, M. Grätzel, E. A. Goodilin and A. B. Tarasov, *J. Phys. Chem. C*, 2017, **121**, 20739–20743.

194   O. Romiluyi, Y. Eatmon, R. Ni, B. P. Rand and P. Clancy, *J. Mater. Chem. A*, 2021, **9**, 13087–13099.

195   P. Ahlawat, M. I. Dar, P. Piaggi, M. Grätzel, M. Parrinello and U. Rothlisberger, *Chem. Mater.*, 2020, **32**, 529–536.

196   S. Pratap, E. Keller and P. Müller-Buschbaum, *Nanoscale*, 2019, **11**, 3495–3499.

197   K. Yan, M. Long, T. Zhang, Z. Wei, H. Chen, S. Yang and J. Xu, *J. Am. Chem. Soc.*, 2015, **137**, 4460–4468.

198   H. Riesemeier, K. Ecker, W. Görner, B. R. Müller, M. Radtke and M. Krumrey, *X-Ray Spectrom.*, 2005, **34**, 160–163.

199   B. Ravel and M. Newville, *J. Synchrotron Radiat.*, 2005, **12**, 537–541.

200   D. M. Többens and S. Zander, *J. Large-Scale Res. Facil. JLSRF*, 2016, **2**, 49.

201   C. A. Schneider, W. S. Rasband and K. W. Eliceiri, *Nat. Methods*, 2012, **9**, 671–675.

202   M. J. Frisch, G. W. Trucks, H. B. Schlegel, G. E. Scuseria, M. A. Robb, J. R. Cheeseman, G. Scalmani, V. Barone, G. A. Petersson, H. Nakatsuji, M. Caricato, A. Marenich, J. Bloino, B. G. Janesko, R. Gomperts, B. Mennucci, H. P. Hratchian, J. V. Ortiz, D. Izmaylov, A. F. Sonnenberg, J. L.; Williams-Young, F. Ding, F. Lipparini, F. Egidi, J. Goings, B. Peng, A. Petrone, T. Henderson, D. Ranasinghe, V. G. Zakrzewski, J. Gao, N. Rega, G. Zheng, W. Liang, M. Hada, M. Ehara, K. Toyota, R. Fukuda, J. Hasegawa, M. Ishida, T. Nakajima, Y. Honda, O. Kitao, H. Nakai, T. Vreven, K. Throssell, J. A. Montgomery, Jr., J. E. Peralta, F. Ogliaro, M. Bearpark, J. J. Heyd, E. Brothers, K. N. Kudin, V. N. Staroverov, T. Keith, R. Kobayashi, J. Normand, K. Raghavachari, A. Rendell, J. C. Burant, S. S. Iyengar, J. Tomasi, M. Cossi, J. M. Millam, M. Klene, C. Adamo, R. Cammi, J. W. Ochterski, R. L. Martin, K. Morokuma, O. Farkas, J. B. Foresman and D. J. Fox, 2016, D. J. Gaussian 09, Revision D. 01.

203   A. D. Becke, *J. Chem. Phys.*, 1993, **98**, 5648–5652.

204   P. J. Stephens, F. J. Devlin, C. F. Chabalowski and M. J. Frisch, *J. Phys. Chem.*, 1994, **98**, 11623–11627.

205   S. Grimme, J. Antony, S. Ehrlich and H. Krieg, *J. Chem. Phys.*, 2010, **132**, 154104.

206   M. Cossi, N. Rega, G. Scalmani and V. Barone, *J. Comput. Chem.*, 2003, **24**, 669–681.

207   J. Pascual, M. Flatken, R. Félix, G. Li, S. Turren-Cruz, M. H. Aldamasy, C. Hartmann, M. Li, D. Di Girolamo, G. Nasti, E. Hüsam, R. G. Wilks, A. Dallmann, M. Bär, A. Hoell and A. Abate, *Angew. Chemie*, 2021, **133**, 21753–21762.

208   M. Teubner and R. Strey, *J. Chem. Phys.*, 1987, **87**, 3195–3200.

209   M. Jung, S. Ji, G. Kim and S. Il Seok, *Chem. Soc. Rev.*, 2019, **48**, 2011–2038.

210   X. Xu, Y. Sun, D. He, Z. Liang, G. Liu, S. Xu, Z. Li, L. Zhu and X. Pan, *J. Mater. Chem. C*, 2021, **9**, 208–213.

211   Y. Liu, H. Geng, X. Qin, Y. Yang, Z. Zeng, S. Chen, Y. Lin, H. Xin, C. Song, X. Zhu, D. Li, J. Zhang, L. Song, Z. Dai and Y. Kawazoe, *Matter*, 2019, **1**, 690–704.

212   J. W. Lee, D. K. Lee, D. N. Jeong and N. G. Park, *Adv. Funct. Mater.*, 2019, **29**, 1807047.

213   D. H. Kim, J. Park, Z. Li, M. Yang, J. S. Park, I. J. Park, J. Y. Kim, J. J. Berry, G. Rumbles and K. Zhu, *Adv. Mater.*, 2017, **29**, 1606831.

214   M. Schmeisser, P. Illner, R. Puchta, A. Zahl and R. Van Eldik, *Chem. - A Eur. J.*, 2012, **18**,

10969–10982.

215   J. Y. Kim, J. W. Lee, H. S. Jung, H. Shin and N. G. Park, *Chem. Rev.*, 2020, **120**, 7867–7918.

216   A. Abate, *Joule*, 2017, **1**, 887.

217   G. Nasti and A. Abate, *Adv. Energy Mater.*, 2020, **10**, 1902467.

218   M. Konstantakou and T. Stergiopoulos, *J. Mater. Chem. A*, 2017, **5**, 11518–11549.

219   M. I. Saidaminov, I. Spanopoulos, J. Abed, W. Ke, J. Wicks, M. G. Kanatzidis and E. H. Sargent, *ACS Energy Lett.*, 2020, **5**, 1153–1155.

220   X. He, T. Wu, X. Liu, Y. Wang, X. Meng, J. Wu, T. Noda, X. Yang, Y. Moritomo, H. Segawa and L. Han, *J. Mater. Chem. A*, 2020, **8**, 2760–2768.

221   D. Ricciarelli, D. Meggiolaro, F. Ambrosio and F. De Angelis, *ACS Energy Lett.*, 2020, **5**, 2787–2795.

222   W. Li, J. Li, J. Li, J. Fan, Y. Mai and L. Wang, *J. Mater. Chem. A*, 2016, **4**, 17104–17110.

223   M. H. Kumar, S. Dharani, W. L. Leong, P. P. Boix, R. R. Prabhakar, T. Baikie, C. Shi, H. Ding, R. Ramesh, M. Asta, M. Graetzel, S. G. Mhaisalkar and N. Mathews, *Adv. Mater.*, 2014, **26**, 7122–7127.

224   K. P. Marshall, M. Walker, R. I. Walton and R. A. Hatton, *Nat. Energy*, 2016, **1**, 16178.

225   Q. Tai, X. Guo, G. Tang, P. You, T.-W. Ng, D. Shen, J. Cao, C.-K. Liu, N. Wang, Y. Zhu, C.-S. Lee and F. Yan, *Angew. Chem. Int. Ed. Engl.*, 2019, **58**, 806–810.

226   Y. Liao, H. Liu, W. Zhou, D. Yang, Y. Shang, Z. Shi, B. Li, X. Jiang, L. Zhang, L. N. Quan, R. Quintero-Bermudez, B. R. Sutherland, Q. Mi, E. H. Sargent and Z. Ning, *J. Am. Chem. Soc.*, 2017, **139**, 6693–6699.

227   S. Shao, J. Liu, G. Portale, H. H. Fang, G. R. Blake, G. H. ten Brink, L. J. A. Koster and M. A. Loi, *Adv. Energy Mater.*, 2018, **8**, 1702019.

228   M. Li, W.-W. Zuo, Y.-G. Yang, M. H. Aldamasy, Q. Wang, S. H. T. Cruz, S.-L. Feng, M. Saliba, Z.-K. Wang and A. Abate, *ACS Energy Lett.*, 2020, **5**, 1923–1929.

229   D. Sabba, H. K. Mulmudi, R. R. Prabhakar, T. Krishnamoorthy, T. Baikie, P. P. Boix, S. Mhaisalkar and N. Mathews, *J. Phys. Chem. C*, 2015, **119**, 1763–1767.

230   W. Liao, D. Zhao, Y. Yu, C. R. Grice, C. Wang, A. J. Cimaroli, P. Schulz, W. Meng, K. Zhu, R.-G. Xiong and Y. Yan, *Adv. Mater.*, 2016, **28**, 9333–9340.

231   S. Gupta, T. Bendikov, G. Hodes and D. Cahen, *ACS Energy Lett.*, 2016, **1**, 1028–1033.

232   T. Handa, T. Yamada, H. Kubota, S. Ise, Y. Miyamoto and Y. Kanemitsu, *J. Phys. Chem. C*, 2017, **121**, 16158–16165.

233   S. J. Lee, S. S. Shin, J. Im, T. K. Ahn, J. H. Noh, N. J. Jeon, S. Il Seok and J. Seo, *ACS Energy Lett.*, 2018, **3**, 46–53.

234   S. Gupta and G. Hodes, *Appl. Sci.*, 2019, **1**, 6.

235   T. M. Koh, T. Krishnamoorthy, N. Yantara, C. Shi, W. L. Leong, P. P. Boix, A. C. Grimsdale, S. G. Mhaisalkar and N. Mathews, *J. Mater. Chem. A*, 2015, **3**, 14996–15000.

236   R. L. Milot, M. T. Klug, C. L. Davies, Z. Wang, H. Kraus, H. J. Snaith, M. B. Johnston and L. M. Herz, *Adv. Mater.*, 2018, **30**, e1804506.

237   C. Hartmann, S. Gupta, T. Bendikov, X. Kozina, T. Kunze, R. Félix, G. Hodes, R. G. Wilks, D. Cahen and M. Bär, *ACS Appl. Mater. Interfaces*, 2020, **12**, 12353–12361.

238   K. J. Savill, A. M. Ulatowski, M. D. Farrar, M. B. Johnston, H. J. Snaith and L. M. Herz, *Adv. Funct. Mater.*, 2020, **30**, 2005594.

239   T. Yokoyama, T.-B. Song, D. H. Cao, C. C. Stoumpos, S. Aramaki and M. G. Kanatzidis, *ACS Energy Lett.*, 2017, **2**, 22–28.

240   A. Vrij, *J. Chem. Phys.*, 1979, **71**, 3267–3270.

241   F. Schaefers, M. Mertin and M. Gorgoi, *Rev. Sci. Instrum.*, 2007, **78**, 123102.

242   S. Tougaard, *Quases-Tougaard Inc*, 2002, 21.

243   S. Tanuma, C. J. Powell and D. R. Penn, *Surf. Interface Anal.*, 1994, 21.

244   N. Li, S. Tao, Y. Chen, X. Niu, C. K. Onwudinanti, C. Hu, Z. Qiu, Z. Xu, G. Zheng, L. Wang, Y. Zhang, L. Li, H. Liu, Y. Lun, J. Hong, X. Wang, Y. Liu, H. Xie, Y. Gao, Y. Bai, S. Yang, G. Brocks, Q. Chen and H. Zhou, *Nat. Energy*, 2019, **4**, 408–415.

245   T. Nakamura, S. Yakumaru, M. A. Truong, K. Kim, J. Liu, S. Hu, K. Otsuka, R. Hashimoto, R. Murdey, T. Sasamori, H. Do Kim, H. Ohkita, T. Handa, Y. Kanemitsu and A. Wakamiya, *Nat. Commun.*, 2020, **11**, 3008.

246   T. Birchall and G. Dénès, *Can. J. Chem.*, 1984, **62**, 591–595.

247   L. Lanzetta, T. Webb, N. Zibouche, X. Liang, D. Ding, G. Min, R. J. E. Westbrook, B. Gaggio, T. J. Macdonald, M. S. Islam and S. A. Haque, *Nat. Commun.*, 2021, **12**, 2853.

248   M. A. Stranick and A. Moskwa, *Surf. Sci. Spectra*, 1993, **2**, 45–49.

249   S. Hoste, H. Willemen, D. Van de Vondel and G. P. Van der Kelen, *J. Electron Spectros. Relat. Phenomena*, 1974, **5**, 227–235.

250   M. M. S. Karim, A. M. Ganose, L. Pieters, W. W. Winnie Leung, J. Wade, L. Zhang, D. O. Scanlon and R. G. Palgrave, *Chem. Mater.*, 2019, **31**, 9430–9444.

251   P. De Padova, M. Fanfoni, R. Larciprete, M. Mangiantini, S. Priori and P. Perfetti, *Surf. Sci.*, 1994, **313**, 379–391.

252   S. Hoste, D. F. Van De Vondel and G. P. Van Der Kelen, *J. Electron Spectros. Relat. Phenomena*, 1979, **17**, 191–195.

253   J. C. Hamill, J. Schwartz and Y. L. Loo, *ACS Energy Lett.*, 2018, **3**, 92–97.

254   J. H. Heo, J. Kim, H. Kim, S. H. Moon, S. H. Im and K. H. Hong, *J. Phys. Chem. Lett.*, 2018, **9**, 6024–6031.

255   K. P. Marshall, R. I. Walton and R. A. Hatton, *J. Mater. Chem. A*, 2015, **3**, 11631–11640.

256   A. Suzuki and T. Oku, *Appl. Surf. Sci.*, 2019, **483**, 912–921.

257   C. Li, A. Wang, L. Xie, X. Deng, K. Liao, J. A. Yang, T. Li and F. Hao, *J. Mater. Chem. A*, 2019, **7**, 24150–24163.

258   Y. Rong, Z. Tang, Y. Zhao, X. Zhong, S. Venkatesan, H. Graham, M. Patton, Y. Jing, A. M. Guloy and Y. Yao, *Nanoscale*, 2015, **7**, 10595–10599.

259   X. Zhang, G. Wu, W. Fu, M. Qin, W. Yang, J. Yan, Z. Zhang, X. Lu and H. Chen, *Adv. Energy Mater.*, 2018, **8**, 1702498.

260   W. Fu, H. Liu, X. Shi, L. Zuo, X. Li and A. K. Y. Jen, *Adv. Funct. Mater.*, 2019, **29**, 1900221.

261   J. J. Yoo, G. Seo, M. R. Chua, T. G. Park, Y. Lu, F. Rotermund, Y. K. Kim, C. S. Moon, N. J. Jeon, J. P. Correa-Baena, V. Bulović, S. S. Shin, M. G. Bawendi and J. Seo, *Nature*, 2021, **590**, 587–593.

262   G.-H. Kim and D. S. Kim, *Joule*, 2021, **5**, 1033–1035.

9 Appendix

9.1 Supporting Information to Chapter 3
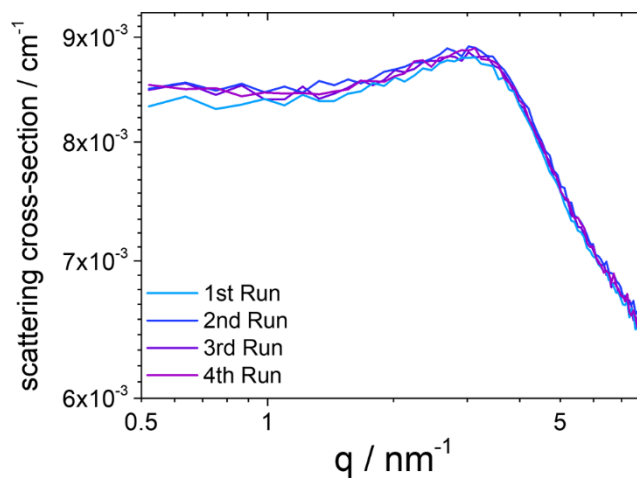
Figure S3.1. Recorded SANS curves (Run1, 2, 3 and 4) of a MAPbI$_3$ perovskite solution (1.3 mol L^{-1}) at 20 °C.
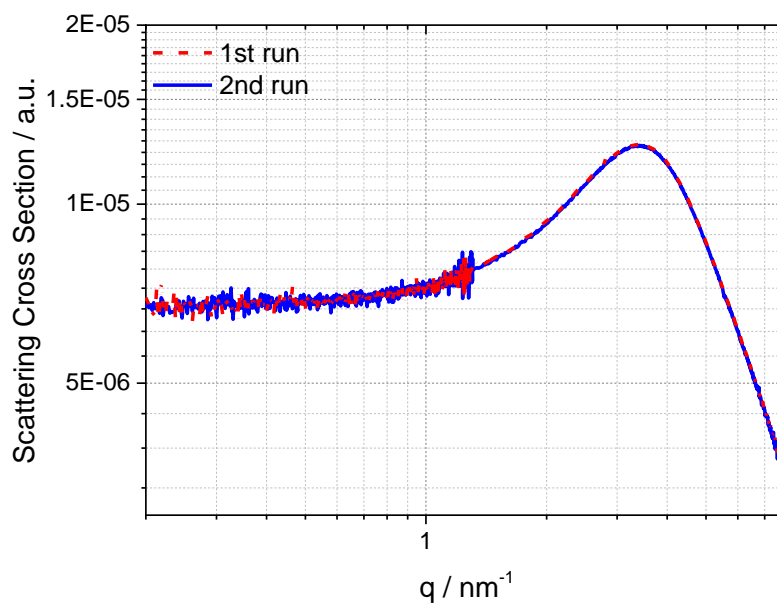
Figure S3.2. Recorded SAXS curves of a MAPbI$_3$ perovskite solution (1 mol L^{-1}). The 1st and 2nd run were measured with a time difference of 4.5 h.
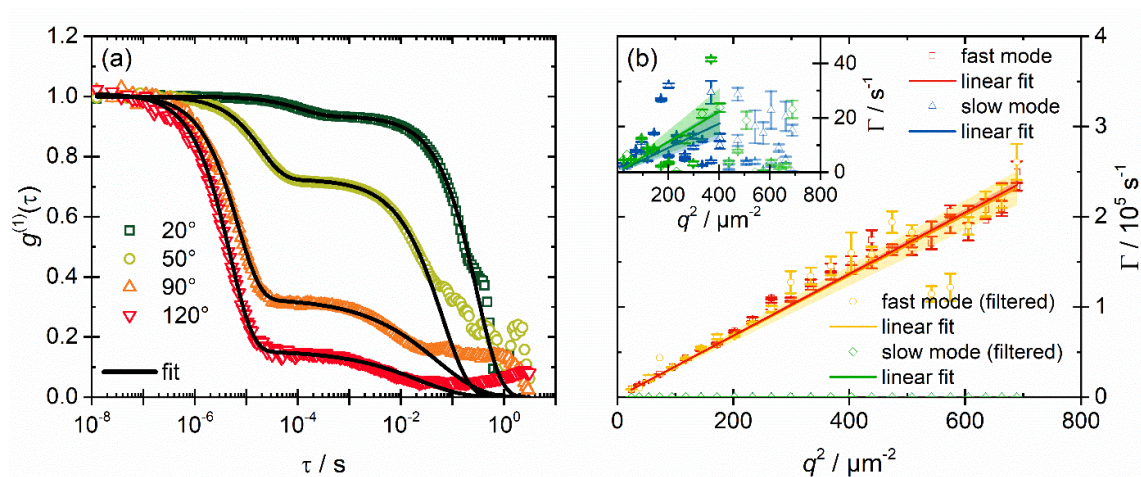
Figure S3.3 DLS on MAPbI$_3$ perovskite precursor solution (1 mol L^{-1}). A selection of fitted correlation curves for different angles is demonstrated in (a). In (b) the resulting Γ versus q^2 plots with the corresponding fits are shown for MAPbI$_3$ and filtered MAPbI$_3$.

Table S3.1. Estimated collective diffusion coefficients and hydrodynamic radii.

Sample	D_{coll} / µm^2/s		R_h / nm	
	Slow	fast	Slow	fast
MAPbI$_3$	0.091(9)	318(3)	2300(300)	0.67(3)
MAPbI$_3$ (filtered)	0.109(20)	327(8)	2000(400)	0.65(3)

In the scope of this work, the focus is set on the fast mode, which is why a measurement time of 30 s / angle was chosen (especially suitable for the size of interest). However, that time is not sufficient to completely cover the observed slow mode. Thus, fluctuations occur in the linear fit given in the inset of **Figure S3.3b**. To fully measure the slow mode several hours measurement time would be needed, which is not in the scope of the current work. The numbers given in Table S1 for the slow mode should be taken as rough estimations based on the chosen fitting model, assuming a Fickian behavior.
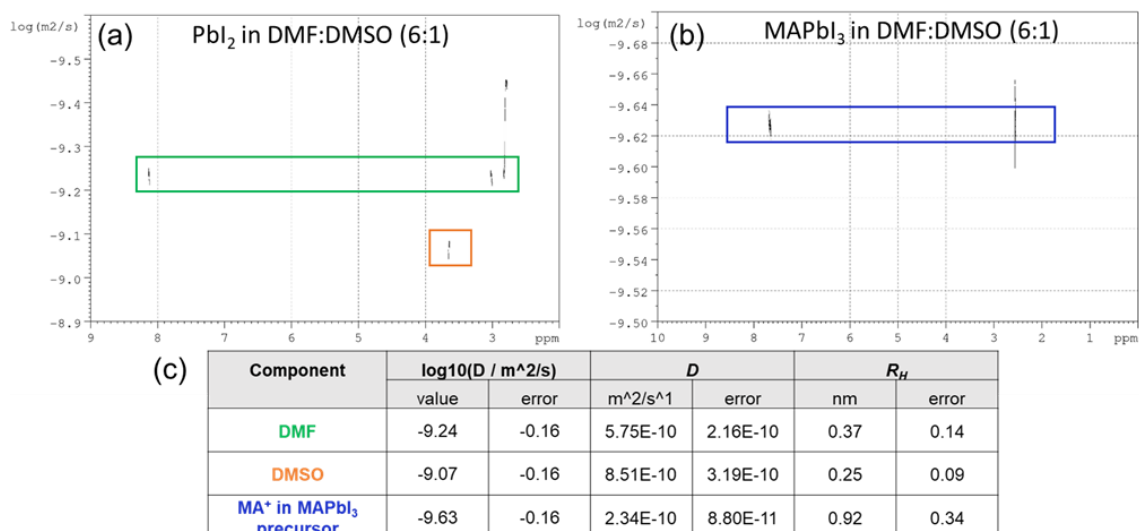
Figure S3.4. DOSY on PbI$_2$ (a) and MAPbI$_3$ (b) precursor solutions, whereby in the case of PbI$_2$ the diffusivity of the solvents become evident and in (b) the diffusivity of MAPbI$_3$. The theoretically expected particle size is derived from the diffusion constant according to the Stokes-Einstein equation, tabulated in (c).

Diffusion Ordered Spectroscopy (DOSY) reports diffusion coefficients for individual resonances in a ^{1}H NMR spectrum. Given in **Figure S3.4** we can directly correlate the ^{1}H-NMR peaks with their diffusion and thus provide related information about the respective molecule.

Using the Stokes-Einstein equation (depicted below) the hydrodynamic radius of a particle can be derived. In addition to the signals that can be clearly identified, we observe a signal corresponding to the chemical shift of the methyl groups of DMF, which has a different diffusivity compared to the other signals associated with DMF. We assume that this occurs as some of the solvent molecules coordinate with PbI$_2$ in solution and therefore show a different diffusivity. However, to explain this in more detail, further measurements would be necessary and would exceed the scope of this paper.
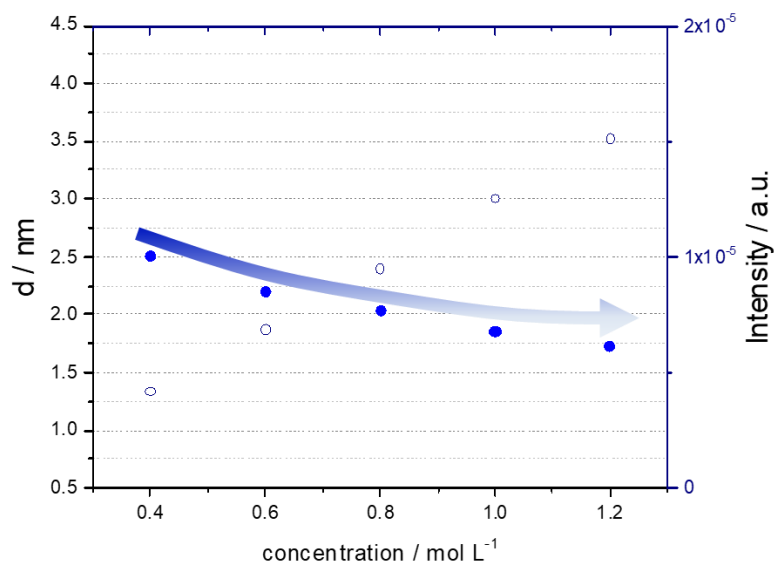
Figure S3.1. Increasing Intensity and decreasing mean d-spacing of Perovskite Precursor solution depending on the concentration.
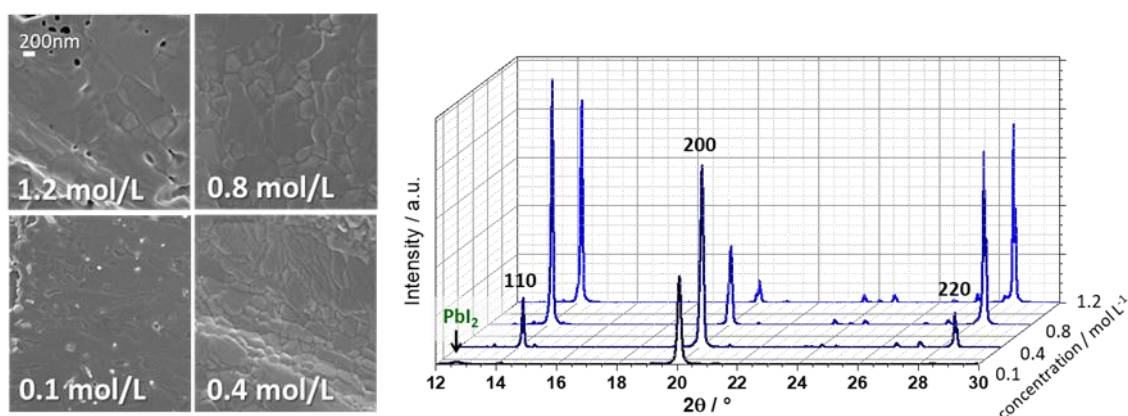
Figure S3.2. Thin film characterization of drop-casted MAPbI$_3$ films. (a) SEM pictures and (b) XRD pattern of crystalline films drop casted using precursor solutions in concentrations of (0.1, 0.4, 0.8 and 1.2) mol L^{-1}.

The SEM images show that with a concentration of 0.1 mol L^{-1} no obvious grain structure can be observed whereas the size of the grains evolving at 0.4 mol L^{-1} seems to increase with increasing concentration. The increasing grain size with concentration goes in line with the observation of stronger inter-particle repulsive interaction in solution, measured with SAXS (**Figure 16**, main text). The XRD pattern of the drop-casted thin films demonstrates that in case of 0.8 and 1.2 mol L^{-1} the (110) and (220) planes are most predominant in the polycrystalline thin film, which is common for the spin-coated thin films used for device preparation. Instead, at lower concentrations from 0.4 towards 0.1 mol L^{-1}, the (110) and (220) planes almost disappear in favor of the diffraction peak of the (200) plane, which becomes predominant for the 0.1 mol L^{-1} case. Furthermore, only the sample of 0.1 mol L^{-1} shows the presence of a peak at $2\theta = 12.6°$

corresponding to the (001) diffraction peak of PbI_2, whereas in all other concentrations no formation of PbI_2 can be observed.

9.2 Supporting Information to Chapter 4

	F(q) Parameters			S(q) Parameters		Variance FIT$_{total}$
sample	s	R/nm	L/nm	R$_{HS}$/nm	F$_p$	σ²
PbI$_2$	0.022	0.407	n.a.	0.68	0.030	4.4 x 10^{-9}
MAPbI$_3$	0.012	0.145	0.64	0.77	0.037	1.7 x 10^{-10}
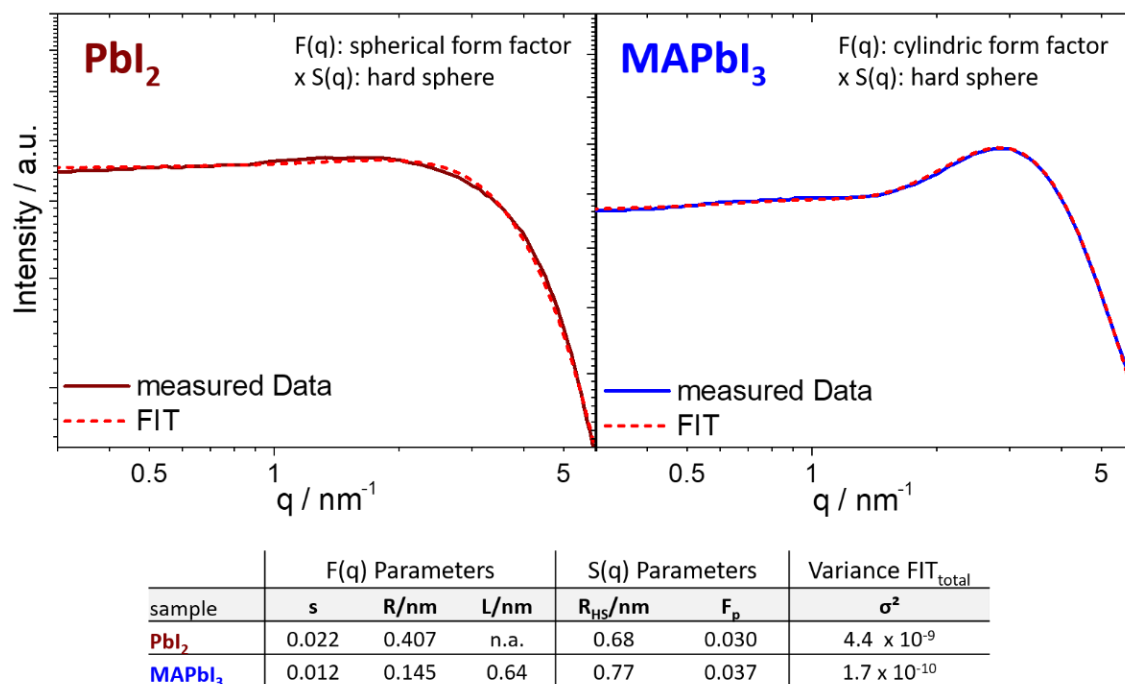
Figure S4.1. Model fit of neutron scattering curves of PbI$_2$ and MAPbI$_3$ precursors. Model fits were performed using SASfit software[140]. The fit parameters for each sample are provided below. For the form factor the width parameter s, the radius R and the length of the cylindrical form factor L are tabulated and for the structure factor the hard-sphere interaction radius R$_{HS}$ and the volume fraction f$_p$ as well as the overall variance of the fit σ².
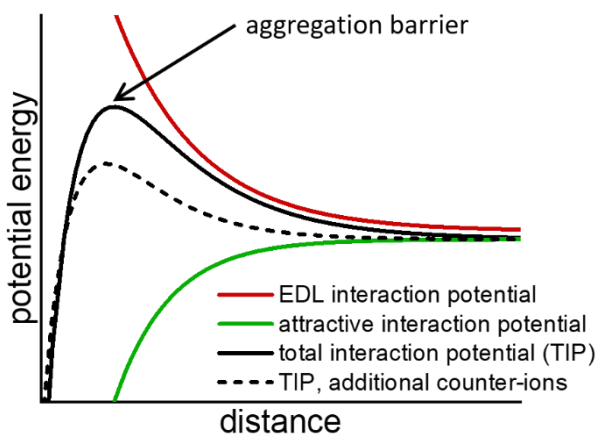
Figure S4.2. Total interaction potential (TIP) as sum of the attraction potential and the repulsion potential (EDL). Change of the TIP as a consequence of counter-ion addition is presented by the dashed black line.
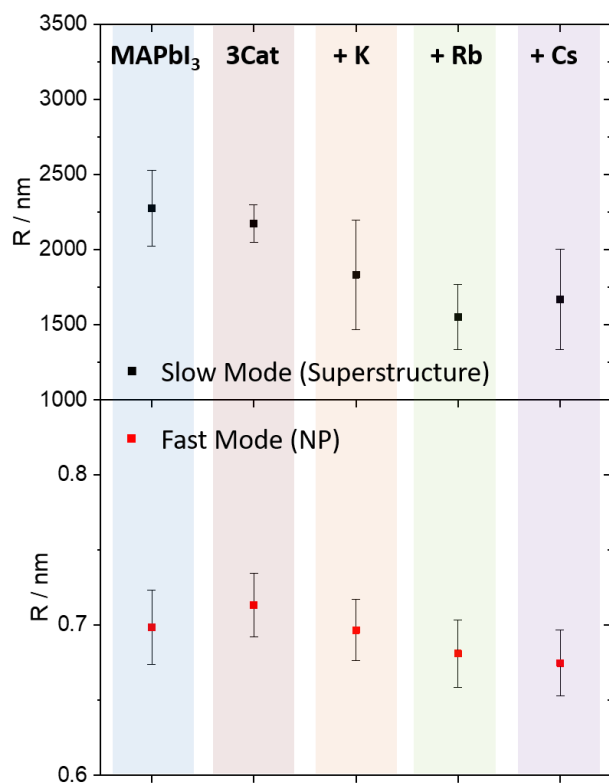
Figure S4.3. Average sizes determined by DLS.
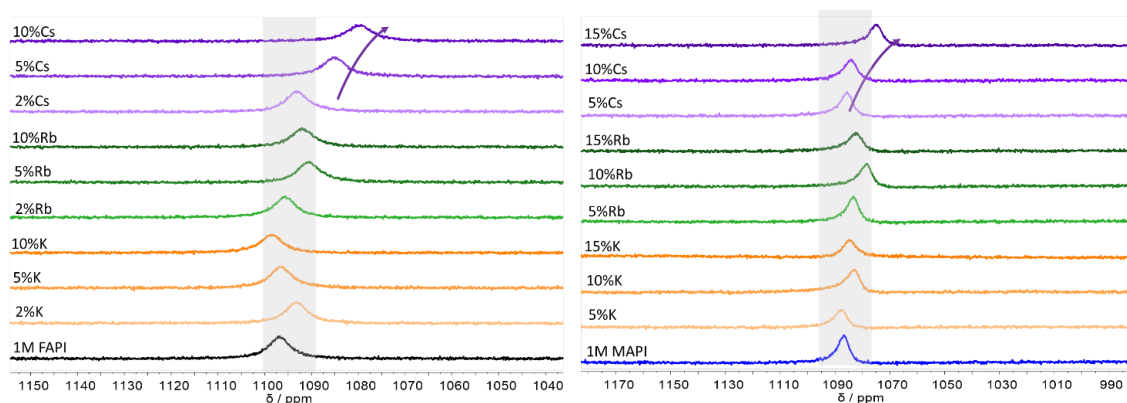
Figure S4.4. [207]Pb-NMR on precursor solutions. FAPbI$_3$ and MAPbI$_3$ solution with the addition of different percentages of alkali metal addition.
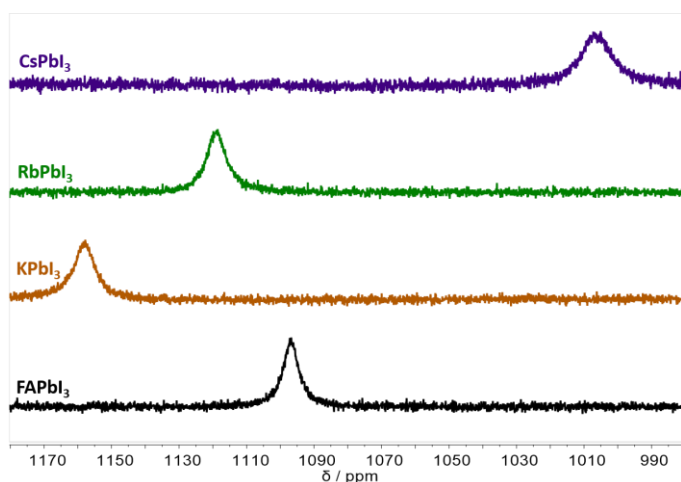
Figure S4.5. ^{207}Pb NMR on precursor solutions. FAPbI$_3$ in comparison to complete substitution of the A-site cation by an alkali metal.

	S(q) Parameters				F(q) Parameters			Variance FIT$_{total}$
sample	R$_{HS}$/nm	f$_p$		sample	s	R/nm	L/nm	σ²
MAPbI$_3$	0.74	0.116		MAPbI$_3$	0.02	0.247	0.745	2.4 x 10^{-12}
+ 5% Cs	0.73	0.109		+ 5% Cs	0.01	0.242	0.720	1.9 x 10^{-12}
+ 10% Cs	0.725	0.09		+ 10% Cs	0.02	0.227	0.700	4.4 x 10^{-12}
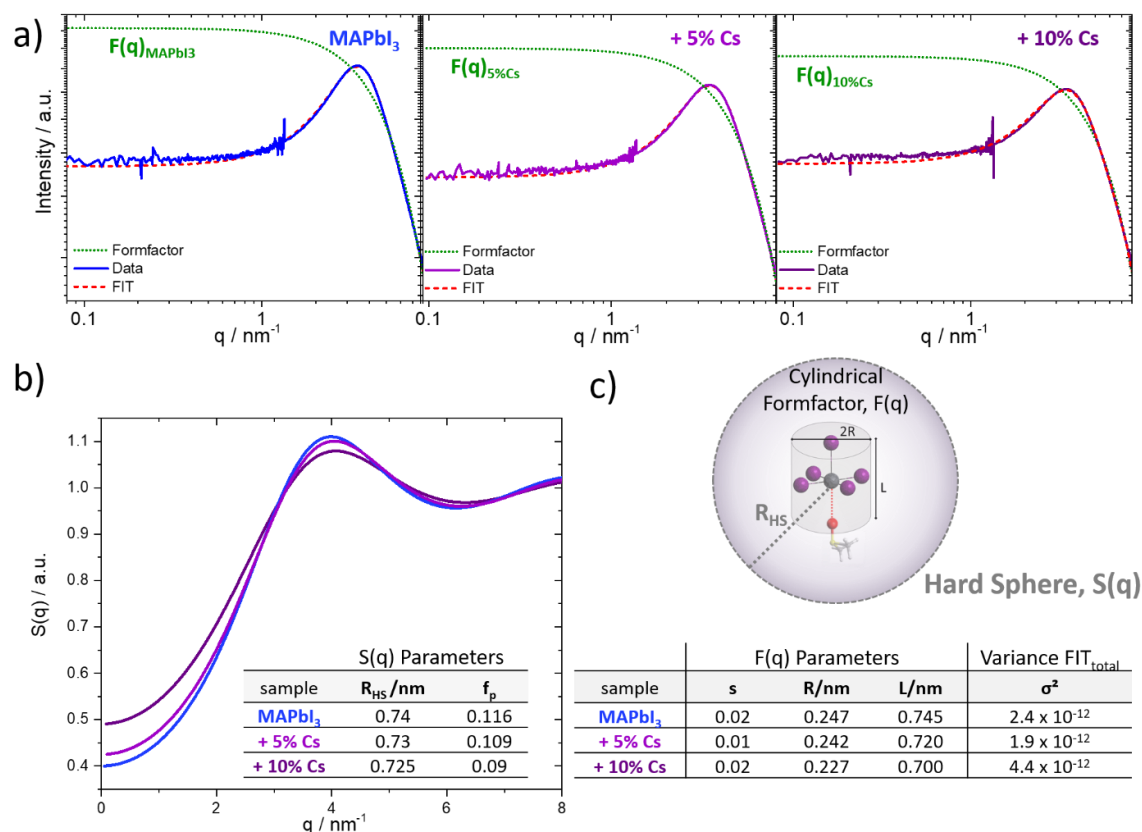
Figure S4.6. Model Fit of SAXS Scattering curves. Model Fits were performed using SASfit software[140]. a) Dotted line shows the model Fit using a cylindrical form factor (F(q)) and hard sphere structure factor (S(q))). The Form factor contribution is shown in green, the measured data of MAPbI$_3$, MAPbI$_3$ with 5 vol% CsI and 10 vol% CsI are presented as solid line (from left to right). A comparison of the structure factor contribution of each sample is displayed in b) as well as the respective parameters in an inset: the hard-sphere interaction radius R$_{HS}$, and the volume fraction f$_p$. c) provides schematically the chosen form and structure factor based on the lead coordination as shown in Figure 17 (main text). The scheme is accompanied by a table containing further fit parameters, such as the width parameter s, the radius R, the length of the cylinder L and the variance of the fit σ².
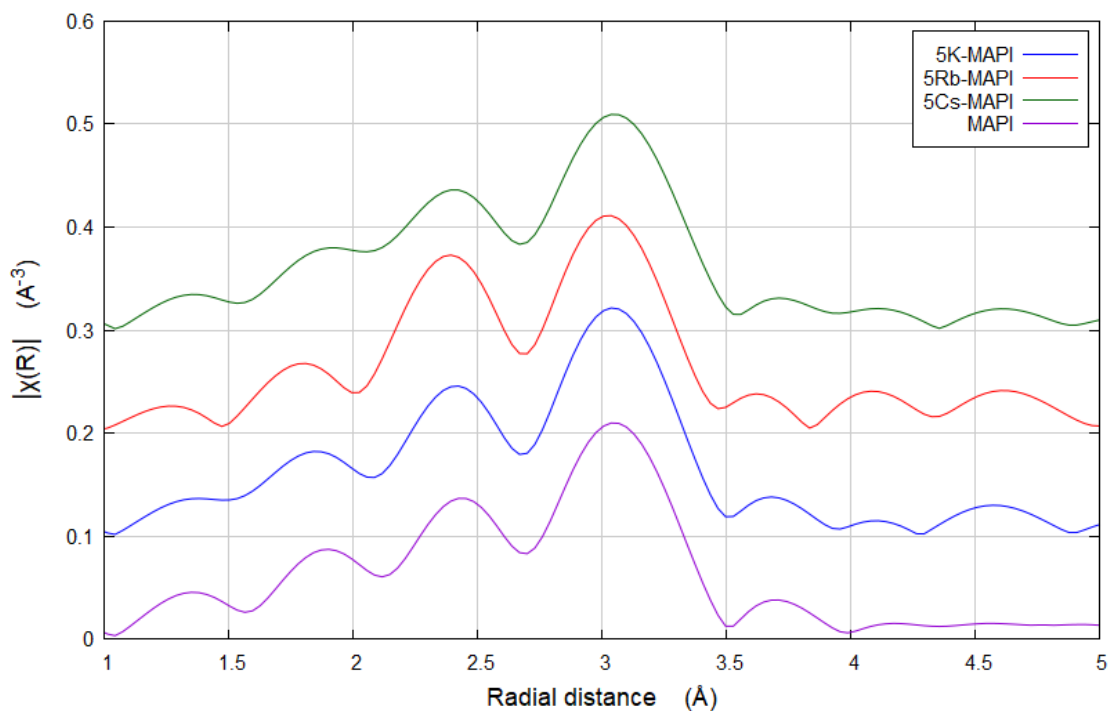
Figure S4.7. EXAFS of perovskite precursor dispersions. $MAPbI_3$ compared to $MAPbI_3$, including 5% addition of alkaline salts, KI, RbI and CsI. For clarity the respective curves are shifted in y-scale.
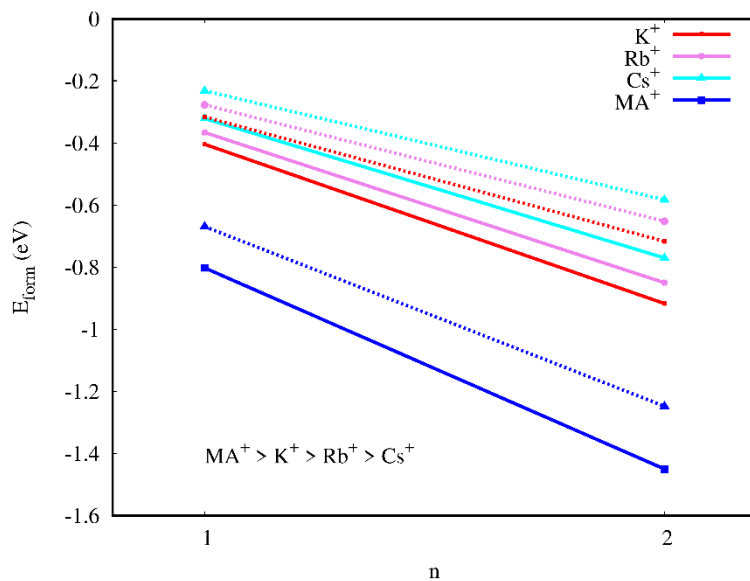
Figure S4.8. DFT calculations of $A^+(solv)_n$ complex formation energy. E_{form}, as a measure of the solvent-cation interaction, evaluated for A = K, Rb, Cs, MA; n = 1 and 2; solv = DMSO (straight line) and DMF (dotted line). Overall MA^+ shows the highest affinity to be coordinated by solvents and Cs^+ the lowest.
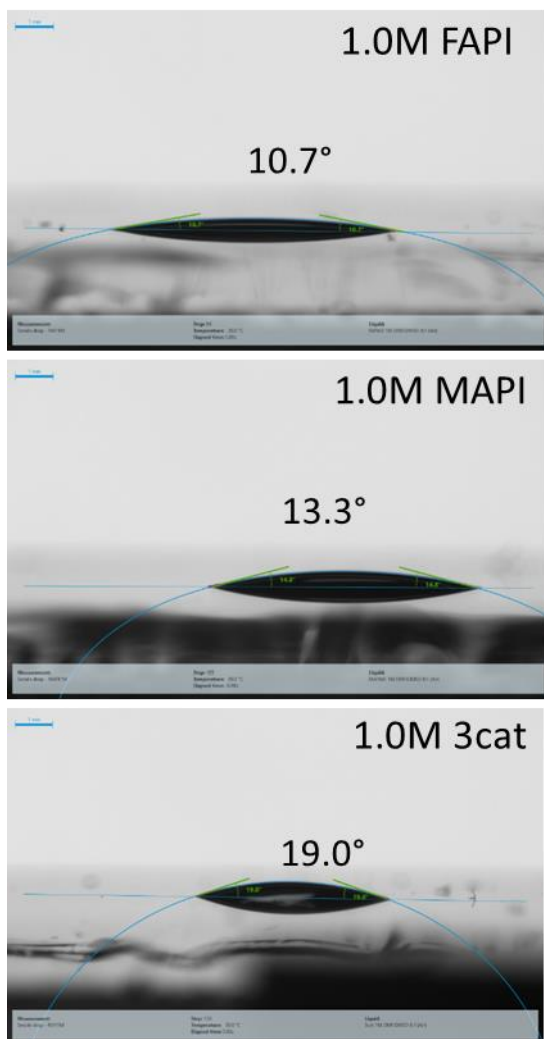
Figure S4.9. Results of contact angle measurement of FAPbI$_3$, MAPbI$_3$ and triple cation perovskite solution all in a concentration of 1 mol L^{-1}.
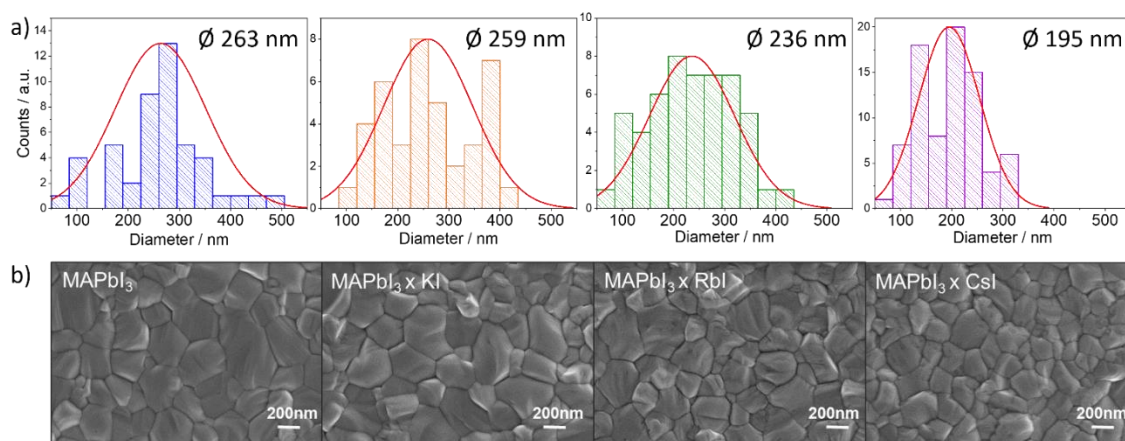
Figure S4.10. Evolution of the grain size distribution with alkali addition. A comparison of plain MAPbI$_3$ thin film to MAPbI$_3$ with the addition of 5% KI, RbI and CsI, respectively, where a) shows the overall size distribution presented by the calculated diameter of a grain area (determined using the software ImageJ[201]), assuming a circular shape of the grains. The mean diameter is given on the top right of each graph. The corresponding SEM images are depicted in b).

9.3 Supporting Information to Chapter 5
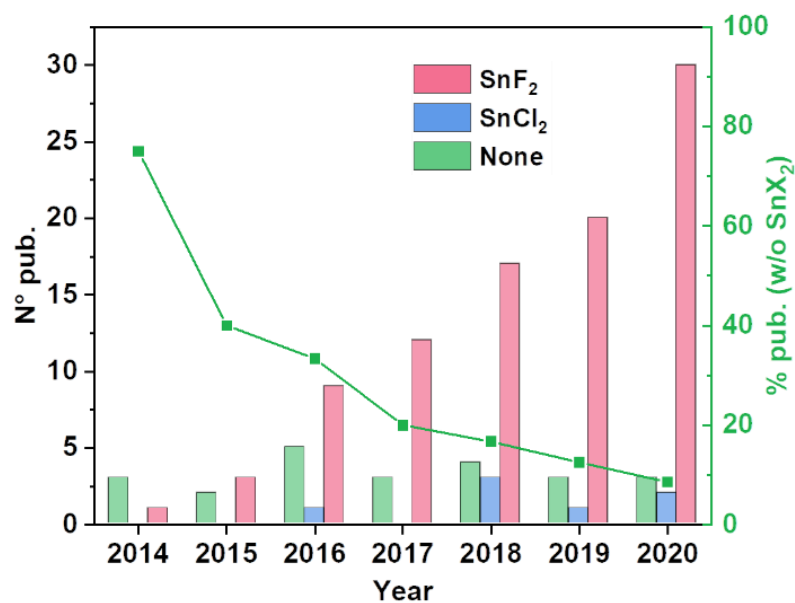
Figure S5.1. Number of scientific publications per year using SnF_2, $SnCl_2$ or none of them. The green line, linked to the right-side vertical axis, illustrates the decline in the relative number of studies based on strategies that avoid the use of SnF_2 or $SnCl_2$.
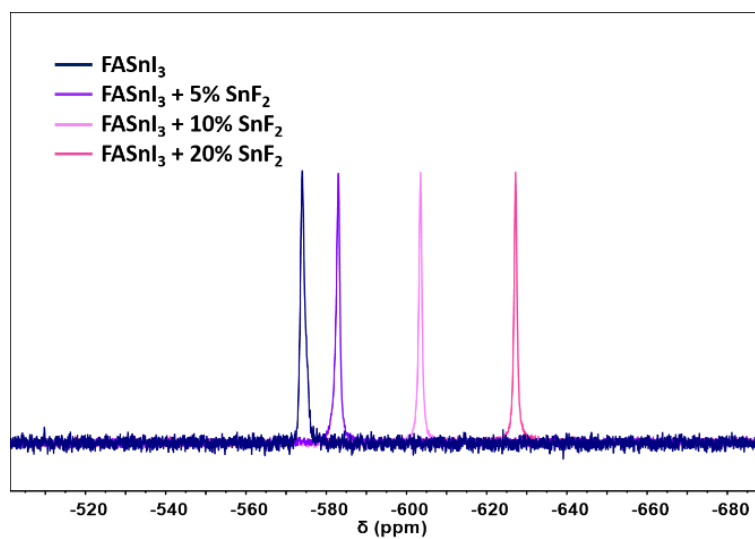
Figure S5.2. ^{119}Sn-NMR of 1 M $FASnI_3$ perovskite precursor solution in DMSO and with different molar concentrations of SnF_2.
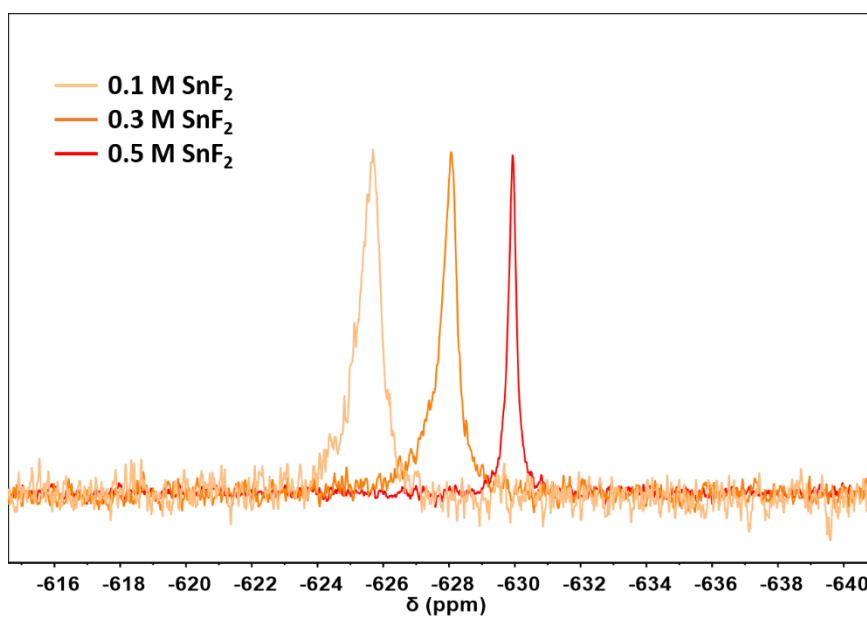
Figure S5.3. ^{119}Sn-NMR of SnF_2 in different concentrations in DMSO. More in detail about these and other solutions preparation, SnI_2 was dissolved at 1 M, while SnI_4, SnF_2 and SnF_4 were saturated (up to 0.5 M). However, as we show in this figure this should not affect the comparison, as SnF_2 signal barely shifts with solution concentration. SnF_4 is more restricted to interactions with the solvent due to the higher complexation degree by fluoride ions and therefore would show even lower signal shift.
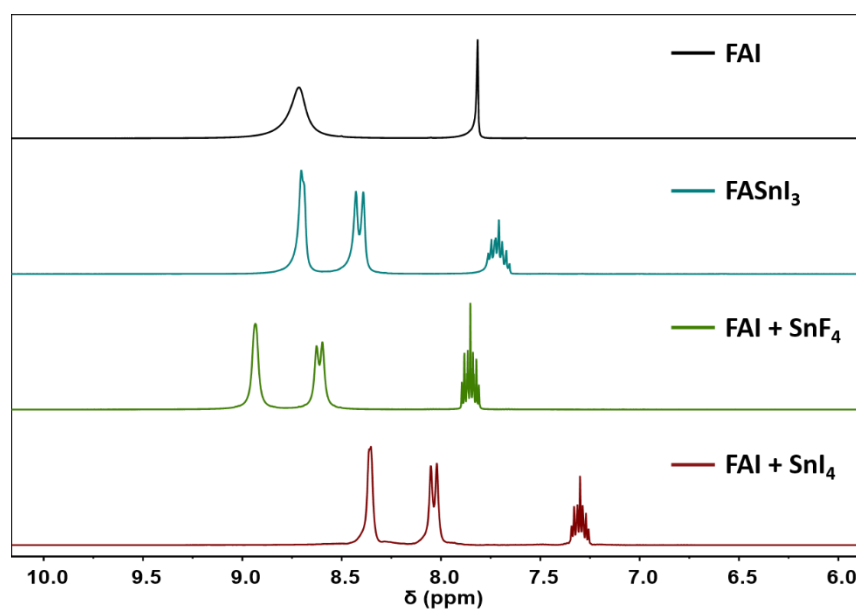
Figure S5.4. ^{1}H-NMR of FAI, FASnI$_3$, FAI + SnF$_4$ and FAI + SnI$_4$ solutions in DMSO at 1:1 stoichiometry. The range was restricted to 6 to 10 ppm for better resolution of the FAI protons.
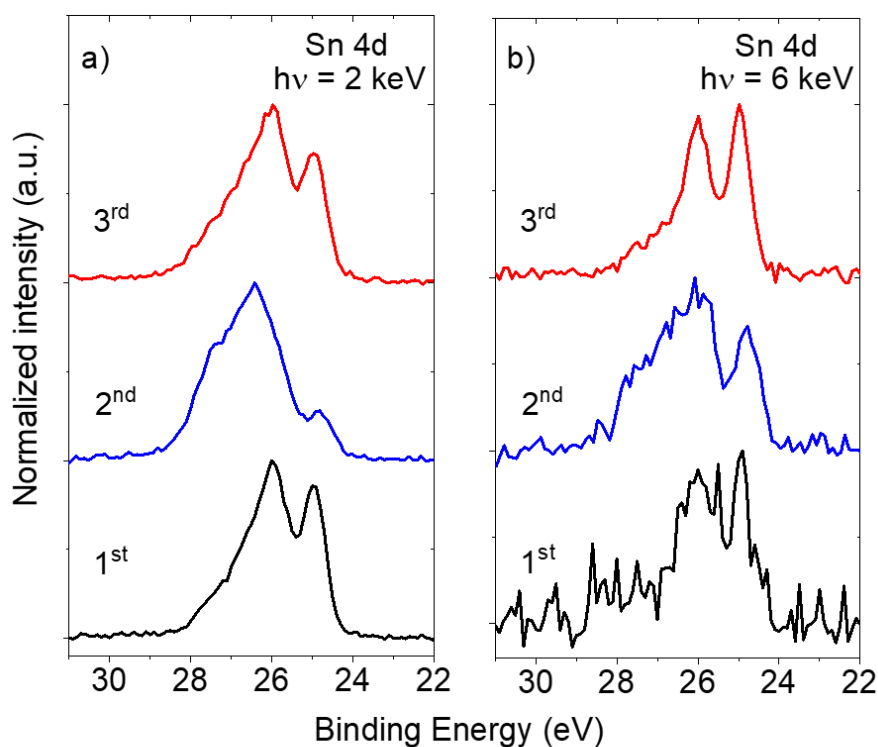
Figure S5.5. Hard X-ray photoelectron spectroscopy (HAXPES) spectra of Sn 4d core levels of three nominal identical FASnI$_3$ films prepared with 10 mol% SnF$_2$, measured using a) 2 keV and b) 6 keV excitations and normalized to maximum intensity (after background subtraction). The samples were measured on separate dates, in the order denoted by the labels.

Figures S5.5 and **S5.5b** display HAXPES spectra of Sn 4d core levels of three FASnI$_3$ films prepared with 10 mol% SnF$_2$ (using the same recipe) measured using 2 keV and 6 keV, respectively. The three nominally identical samples were prepared and measured on separate dates but following the same procedures and parameters. Differences in Sn chemical environment, which can be specially observed for the 2nd sample, indicate variations in sample properties despite an identical sample preparation process, the reason for which is likely due to a fluke in the conditions in one (or more) of the sample production (e.g., fluctuations in precursors, glovebox conditions, etc.)/handling (e.g., non-optimal selection of sample area to be cut and mounted for measurement)/transporting (e.g., improper sealing)/measurement (e.g., fluctuation in characterization vacuum conditions, duration between sample preparation and measurement, etc.) steps. However, these observed spectral variations should be considered when examining the Sn 4d spectra shown in the main section, as they are in most cases more pronounced than the differences between individual spectra as a result

of the different additives. Therefore, reaching statistically-relevant outcomes, beyond the conservative conclusions presented in the main text, on the impact of individual additives would require measuring multiple sets of this sample series, a task beyond the scope of the present work.
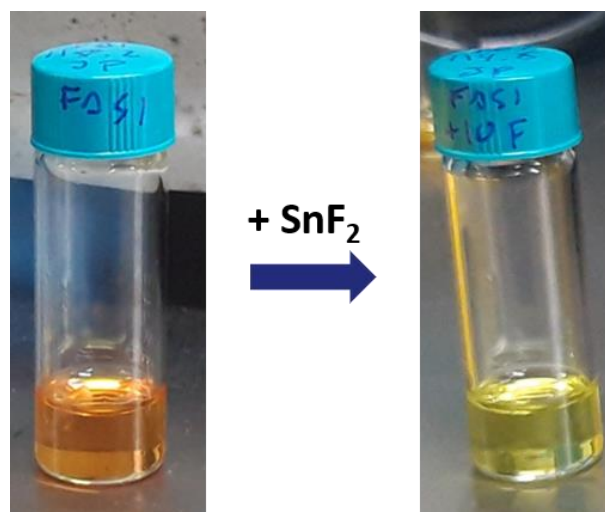
Figure S5.6. Picture of fresh 1 mol L^{-1} FASnI$_3$ solution in DMF (left) and after addition of 10 % SnF$_2$ (right).
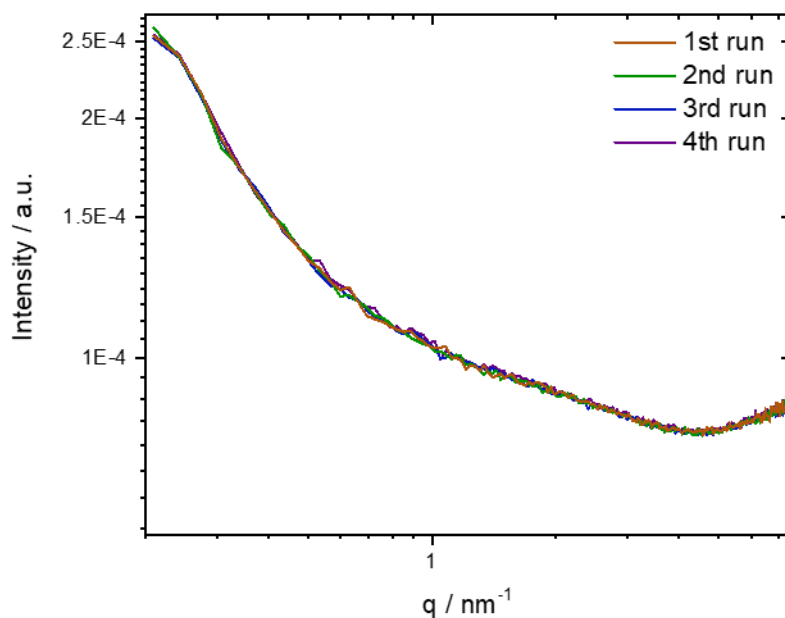
Figure S5.7. Reproducibility of SAXS measurements in different runs using the example of FASnI$_3$ in DMSO (1 mol L^{-1}). Beam damage can be excluded.
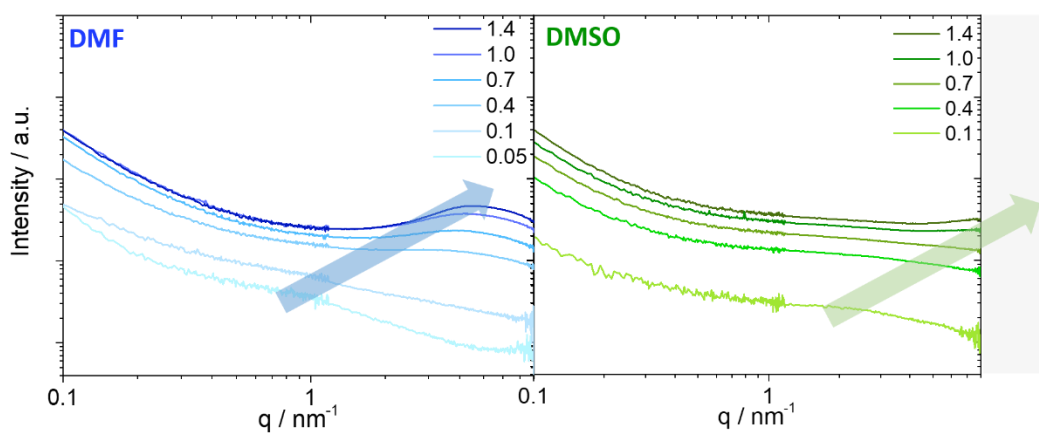
Figure S5.8. SAXS scattering curves for FASnI$_3$ in different concentrations in DMF (left) vs DMSO (right). Evolution of the structure factor peak goes beyond the limited window of the respected q-range in SAXS. Still, the trend is identifiable.
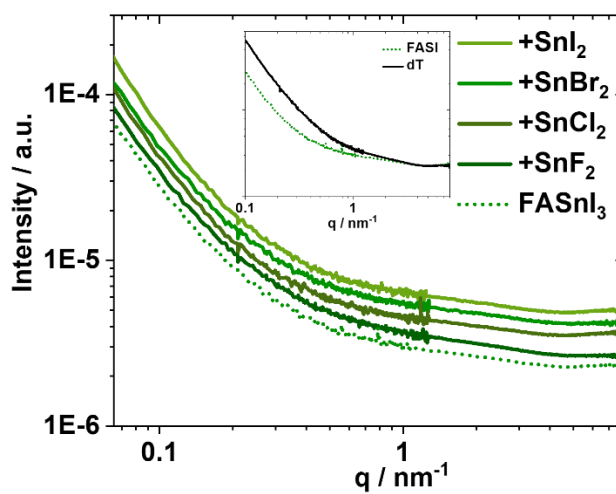
Figure S5.9. SAXS scattering curves of FASnI$_3$ solution in DMSO compared to FASnI$_3$ with 10 % of SnF$_2$, SnCl$_2$, SnBr$_2$ and SnI$_2$. In the small inset, the FASnI$_3$ scattering curve is plotted in direct comparison to an aged solution.
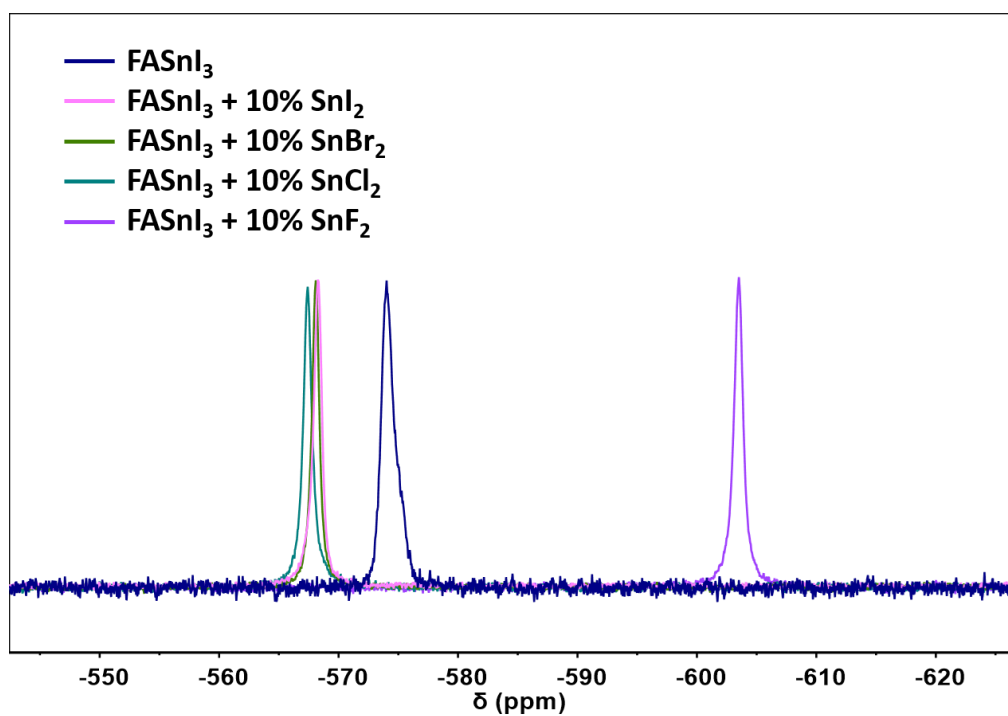
Figure S5.10. ^{119}Sn-NMR of 1 M FASnI$_3$ solutions with 10 % molar concentration of SnX$_2$ additives (X = F, Cl, Br, I).
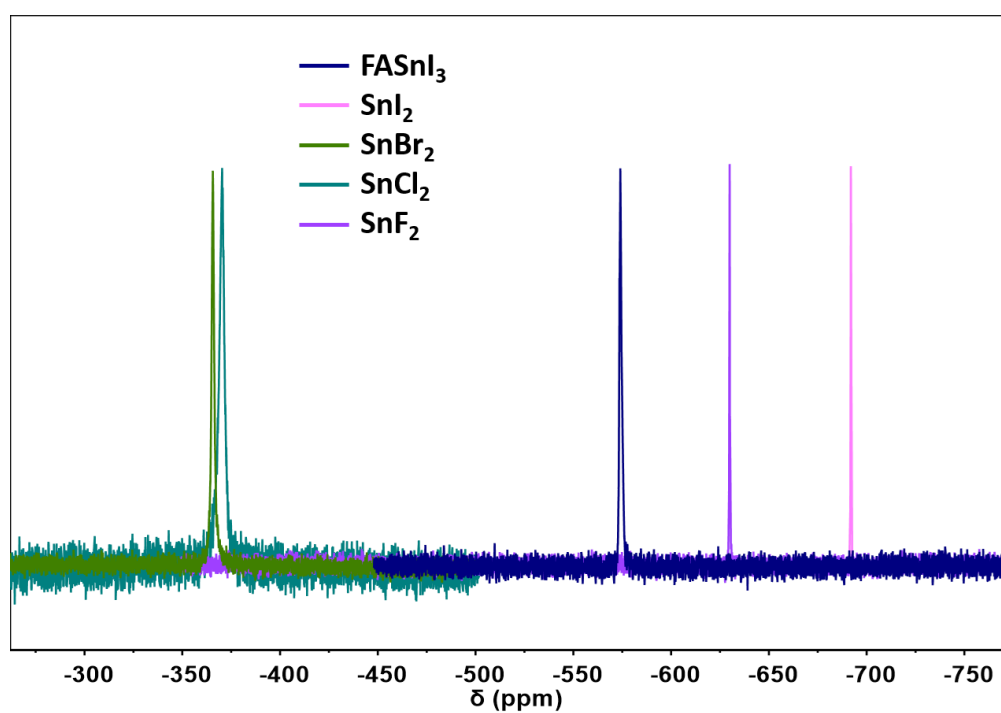
Figure S5.11. ^{119}Sn-NMR of FASnI$_3$, SnF$_2$, SnCl$_2$, SnBr$_2$ and SnI$_2$ in DMSO. FASnI$_3$ and SnI$_2$ were prepared at 1 mol L^{-1}, while SnF$_2$, SnCl$_2$ and SnBr$_2$ were at 0.5 mol L^{-1}.
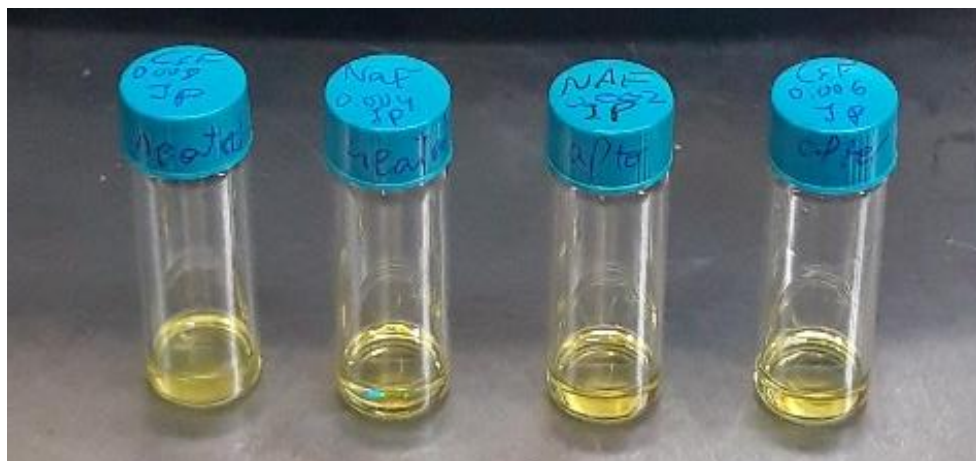
Figure S5.12. From left to right, heated 1 mol L^{-1} FASnI$_3$ solutions in DMSO first saturated with CsF and NaF, then heated and first heated, then saturated with NaF and CsF.
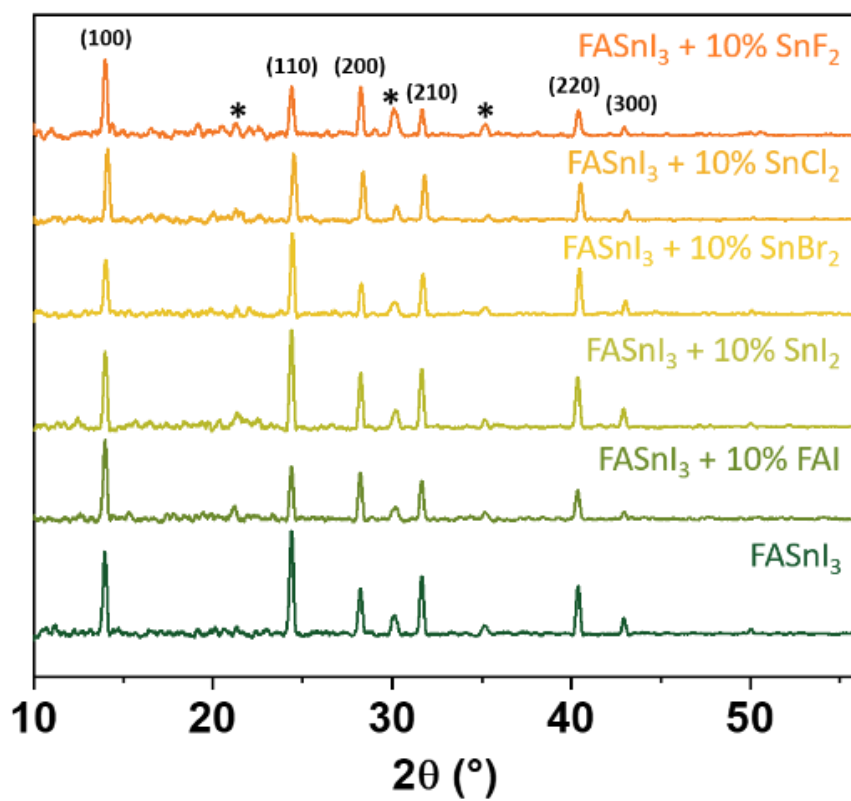
Figure S5.13. XRD of thin films of pristine FASnI$_3$ and containing a 10 % excess of FAI, SnI$_2$, SnBr$_2$, SnCl$_2$ and SnF$_2$.
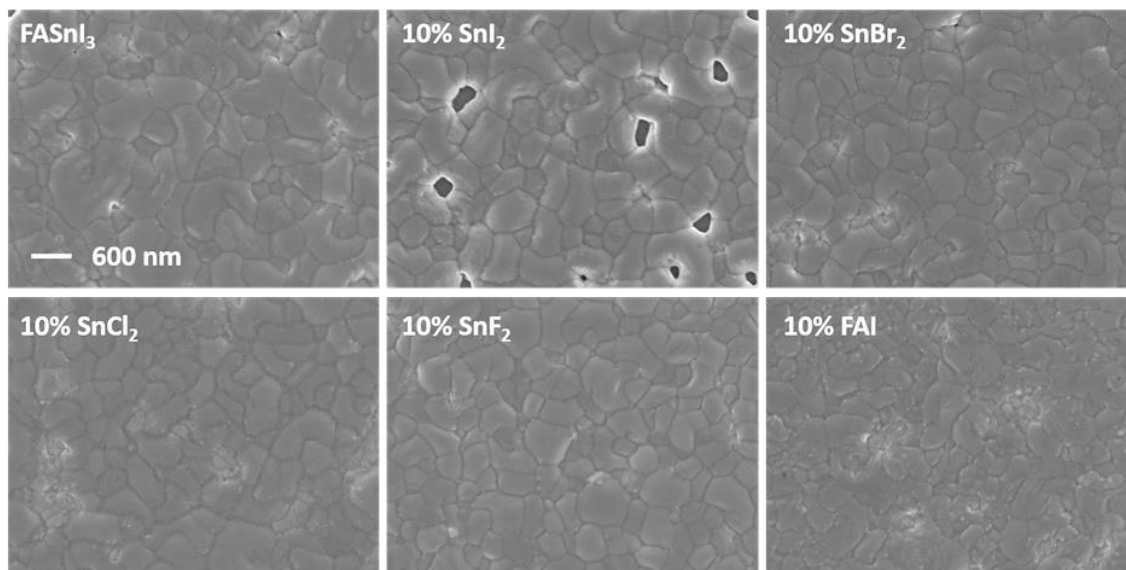
Figure S5.14. SEM of thin films of pristine FASnI$_3$ and containing a 10 % excess of FAI, SnI$_2$, SnBr$_2$, SnCl$_2$ and SnF$_2$.
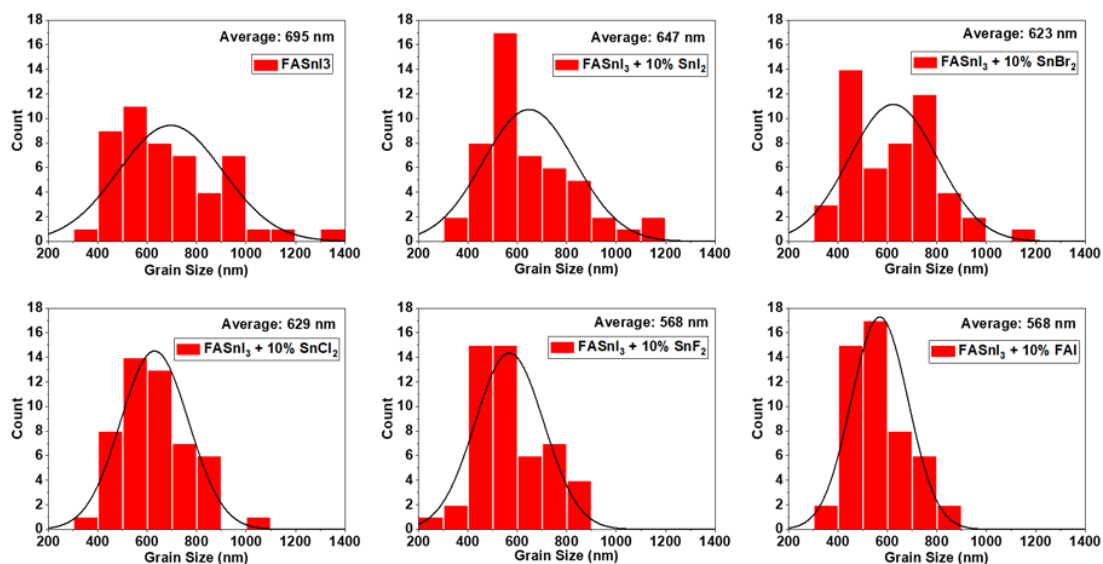
Figure S5.15. Grain size distribution from the SEM of thin films of pristine FASnI$_3$ and containing a 10 % excess of FAI, SnI$_2$, SnBr$_2$, SnCl$_2$ and SnF$_2$. 50 grains were measured for the statistics of each sample.
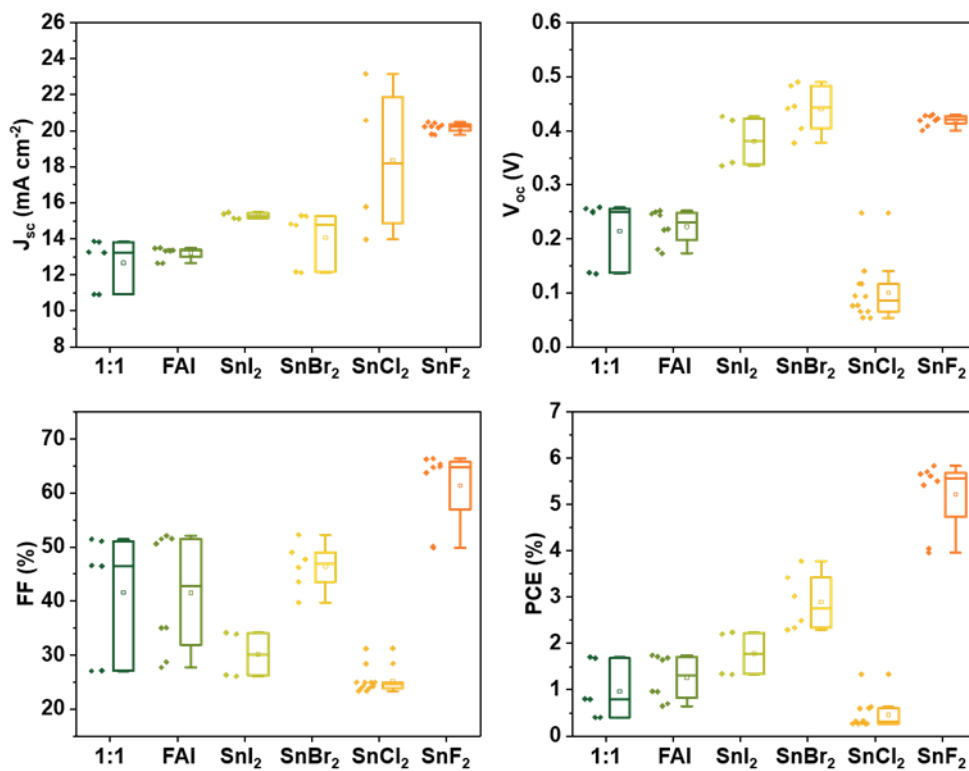
Figure S5.16. Performance of solar cells based on pristine FASnI$_3$ and containing a 10 % excess of FAI, SnI$_2$, SnBr$_2$, SnCl$_2$ and SnF$_2$.

9.4 Supporting Information – Preliminary Data
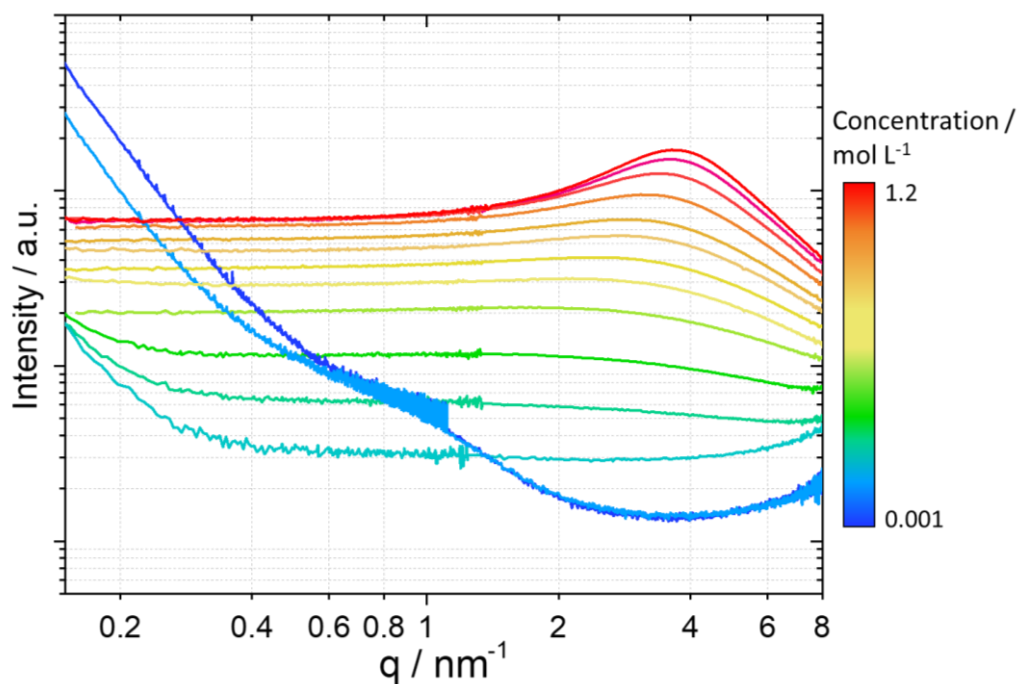
Figure S6.1. SAXS concentration series of MAPbI$_3$ precursor solution. Covering concentrations from 0.001 to 1.2 mol L^{-1} in a stoichiometry of 1:1 in a solvent mixture of DMF:DMSO, 6:1.
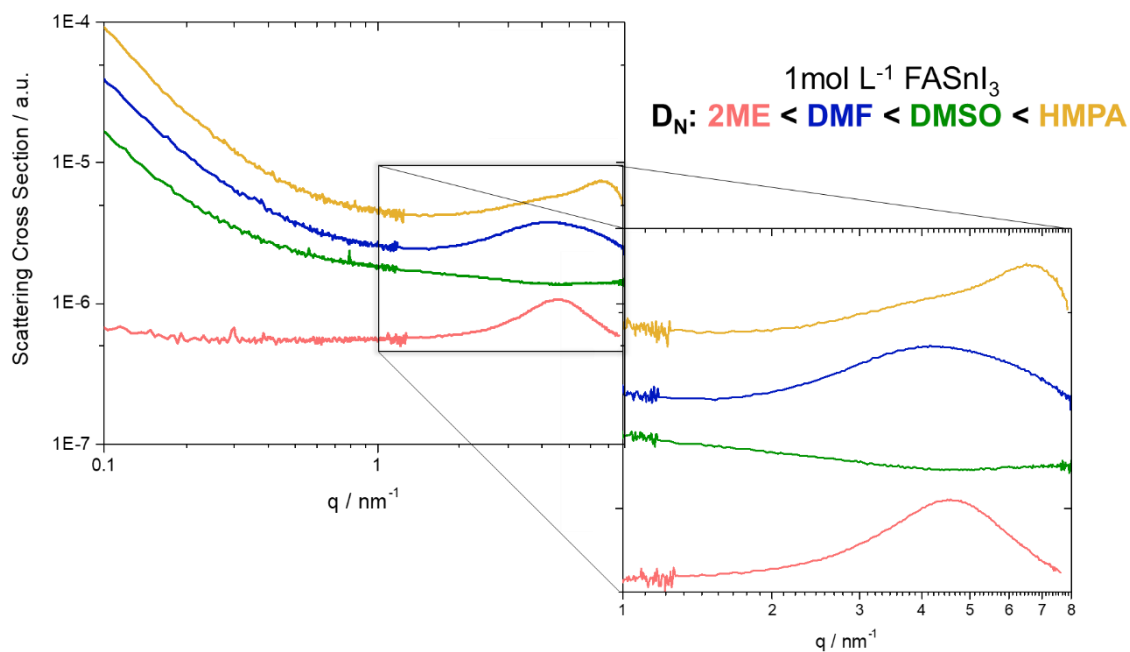
Figure S6.2. SAXS curves of FASnI$_3$ precursor solutions using different solvents. The measured samples were prepared in a concentration of 1 mol L^{-1} in 2ME (rose), DMF (blue), DMSO (green) and HMPA (yellow) respectively. The differences in the high q-region indicate significant changes of the colloidal interactions depending on the Gutmann Donor Number D$_N$ of the solvent.[214]

9.5 List of Publications

First authorship peer-review publications

Small-angle scattering to reveal the colloidal nature of halide perovskite precursor solutions

Marion A. Flatken, Armin Hoell*, Robert Wendt, Eneli Härk, André Dallmann, Albert Prause, Jorge Pascual, Eva Unger, Antonio Abate*

Status: Published (DOI: 10.1039/D1TA01468D)

Role of the A-site Cation on the Early Stages Crystallization of Halide Perovskite

Marion A. Flatken, Eros Radicchi, Robert Wendt, Ana Guilherme Buzanich, Eneli Härk, Jorge Pascual, Florian Mathies, Oleksandra Shargaieva, Albert Prause, André Dallmann, Filippo De Angelis, Armin Hoell, Antonio Abate*

Status: under review (Chem. Mater.)

Fluoride Chemistry in Tin Halide Perovskites

Jorge Pascual[§]*, Marion A. Flatken[§], Roberto Félix, Guixiang Li, Silver-Hamill Turren-Cruz, Mahmoud H. Aldamasy, Claudia Hartmann, Meng Li, Diego Di Girolamo, Giuseppe Nasti, Elif Hüsam, Regan G. Wilks, André Dallmann, Marcus Bär, Armin Hoell, Antonio Abate*

[§]these authors contribute equally to the work

Status: Published (DOI: 10.1002/anie.202107599)

First authorship conference paper

The bloom of perovskite optoelectronics: Fundamental science matters

Jue Gong[§], Marion A. Flatken[§], Antonio Abate*, Juan-Pablo Correa-Baena*, Iván Mora-Seró*, Michael Saliba*, Yuanyuan Zhou*

[§]these authors contribute equally to the work

Status: Published (DOI: 10.1021/acsenergylett.9b00477)

Co-authored publications

Origin of Sn (ii) oxidation in tin halide perovskites

Jorge Pascual, Giuseppe Nasti, Mahmoud H Aldamasy, Joel A. Smith, Marion A. Flatken, Nga Phung, Diego Di Girolamo, Silver-Hamill Turren-Cruz, Meng Li, André Dallmann, Roberto Avolio, Antonio Abate*

Status: Published (DOI: 10.1039/D0MA00245C)

Ion migration-induced amorphization and phase segregation as a degradation mechanism in planar perovskite solar cells

Diego Di Girolamo, Nga Phung, Felix Utama Kosasih, Francesco Di Giacomo, Fabio Matteocci, Joel A. Smith, Marion A. Flatken, Hans Köbler, Silver H Turren Cruz, Alessandro Mattoni, Lucio Cinà, Bernd Rech, Alessandro Latini, Giorgio Divitini, Caterina Ducati, Aldo Di Carlo, Danilo Dini, Antonio Abate*

Status: Published (DOI: 10.1002/aenm.202000310)

20.8% Slot-Die Coated MAPbI3 Perovskite Solar Cells by Optimal DMSO-Content and Age of 2-ME Based Precursor Inks

Jinzhao Li, Janardan Dagar, Oleksandra Shargaieva, Marion A. Flatken, Hans Köbler, Markus Fenske, Christof Schultz, Bert Stegemann, Justus Just, Daniel M. Többens, Antonio Abate, Rahim Munir, Eva Unger*

Status: Published (DOI: 10.1002/aenm.202003460)

Halogen-Bonded Hole-Transport Material Suppresses Charge Recombination and Enhances Stability of Perovskite Solar Cells

Laura Canil, Jagadish Salunke, Qiong Wang, Maning Liu, Hans Köbler, Marion A. Flatken, Luca Gregori, Daniele Meggiolaro, Damiano Ricciarelli, Filippo De Angelis, Martin Stolterfoht, Dieter Neher, Arri Priimagi, Paola Vivo, Antonio Abate*

Status: Published (DOI: 10.1002/aenm.202101553)

Releasing the Power of the Crowd with FAIR Data Management by introducing the Perovskite Database Project

T. Jesper Jacobsson*, Adam Hultqvist, Alberto García-Fernández, Aman Anand, Amran Al-Ashouri, Anders Hagfeldt, Andrea Crovetto, Antonio Abate, Antonio Gaetano Ricciardulli, Anuja Vijayan, Ashish Kulkarni, Assaf Y. Anderson, Barbara Primera Darwich, Bowen Yang, Brendan L. Coles, Carlo A.R. Perini, Carolin Rehermann, Daniel Ramirez, David Fairen-Jimenez, Diego Di Girolamo, Donglin Jia, Elena Avila, Emilio J. Juarez-Perez, Fanny Baumann, Florian Mathies, G. S. Anaya González, Gerrit Boschloo, Giuseppe Nasti, Gopinath Paramasivam, Guillermo Martínez-Denegri, Hampus Näsström, Hannes Michaels, Hans Köbler, Hua Wu, Iacopo Benesperi, M. Ibrahim Dar, Ilknur Bayrak Pehlivan, Isaac E. Gould, Jacob N. Vagott, Janardan Dagar, Jeff Kettle, Jie Yang, Jinzhao Li, Joel A. Smith, Jorge Pascual, Jose J. Jerónimo-Rendón, Juan Felipe Montoya, Juan-Pablo Correa-Baena, Junming Qiu, Junxin Wang, Kari Sveinbjörnsson, Katrin Hirselandt, Krishanu Dey, Kyle Frohna, Lena Mathies, Luigi A. Castriotta, Mahmoud. H. Aldamasy, Manuel Vasquez-Montoya, Marco A. Ruiz-Preciado, Marion A. Flatken, Mark V. Khenkin, Max Grischek, Mayank Kedia, Michael Saliba, Miguel Anaya, Misha Veldhoen, Neha Arora, Oleksandra Shargaieva, Oliver Maus, Onkar S. Game, Ori Yudilevich, Paul Fassl, Qisen Zhou, Rafael Betancur, Rahim Munir, Rahul Patidar, Samuel Stranks, Shahidul Alam, Shaoni Kar, Thomas Unold, Tobias Abzieher, Tomas Edvinsson, Tudur Wyn David, Ulrich W. Paetzold, Waqas Zia, Weifei Fu, Weiwei Zuo, Vincent R. F. Schröder, Wolfgang Tress, Xiaoliang Zhang, Yu-Hsien Chiang, Zafar Iqbal, Zhiqiang Xie, Eva Unger,*

Status: accepted (Nat. Energy)

The Role of Terminal Group Position in Triphenylamine Based Self-Assembled Hole-Selective Monolayers in Perovskite Solar Cells

Ece Aktas, Rajesh Pudi, Nga Phung, Robert Wenisch, Luca Gregori, Daniele Meggiolaro, Marion A. Flatken, Filippo De Angelis, Iver Lauermann, Antonio Abate,* Emilio Palomares*

Status: under review (Sol. RRL)

Lights and Shadows of DMSO as Solvent for Tin Halide Perovskites

Jorge Pascual*, Diego Di Girolamo*, Marion A. Flatken, Mahmoud H. Aldamasy, Guixiang Li, Meng Li, Antonio Abate*

Status: under review (Chem. Eur. J)

Solution-based Low Temperature CsPbI$_3$ Nanoparticles Perovskite Solar Cells

Adva Shpatz Dayan, Stav Rahmany, Marion A. Flatken, Tal Binyamin, Armin Hoell, Antonio Abate, Lioz Etgar*

Status: accepted (Material Advances)

Conference Contributions

Oral Presentations

Resonant Elastic X-ray Scattering (REXS 2019), Riverhead, Long Island, NY, 2019 June 17th - 21th – Title: "Characterization of Perovskite Layers in High-Performance Solar Cells using Small-Angle X-Ray Scattering"

PSCO 2019, Lausanne, Switzerland. September 30th, 2019 to October 2nd, 2019 – Title: "Characterization of Perovskite Precursor Solutions in order to achieve High-Performance Solar Cells"

nanoGe Fall Meeting 2019, Berlin, Germany. 2019 November 4th – 8th, Title: "Characterization of Perovskite Precursor Solutions in order to achieve High-Performance Solar Cells"

Virtual Spring Meeting FV Chemical and Polymer Physics: Polymer and Soft Matter, 2021 March 22nd – 24th, Title: "Characterization of Perovskite Precursor Solutions in order to achieve High-Performance Solar Cells"

BESSY@HZB User Meeting, virtual conference, 2021 December 9th, invited presentation, Title: "Energy conversion - Chemical Insights into Perovskite Precursors"

The 2021 International Chemical Congress of Pacific Basin Societies (Pacifichem). virtual conference, 2021, December 16th – 21st, Title: "Characterization of perovskite precursor solutions in order to achieve high-performance solar cells"

Poster Presentations

NanoGe - International Conference on Hybrid and Organic Photovoltaics (HOPV19) Roma, Italy, 2019 May 12th - 15th - Poster, Marion A. Flatken, 229 Publication date: 11th February 2019, "Structural Properties of Perovskite Layers in High-Performance Solar Cells"

Resonant Elastic X-ray Scattering (REXS 2019), Riverhead, Long Island, NY, 2019 June 17th - 21th – Poster, Marion A. Flatken, "Characterization of Perovskite Layers in High-Performance Solar Cells using Small-Angle X-Ray Scattering"

List of Abbreviations

AAAS	American Association for the Advancement of Science
BE	binding energy
$CaTiO_3$	calcium titanate
CNT	classical nucleation theory
CsF	cesium fluoride
DFT	density functional theory
DLS	dynamic light scattering
DLVO	Derjaguin, Landau, Verwey, Overbeek
DMF	*N*,*N*-dimethylformamide
DMSO	dimethyl sulfoxide
EDL	electric double layer
EXAFS	extended X-ray absorption fine structure spectroscopy
FA	formamidinium
FABr	formamidinium bromide
FAI	formamidinium iodide
$FAPbI_3$	formamidinium lead iodide
$FASnI_3$	formamidinium tin iodide
GIWAXS	grazing incidence wide-angle X-ray scattering
GIXRD	grazing incidence X-ray diffraction
HAXPES	hard X-ray photoelectron spectroscopy
HUST	Huazhong University of Science and Technology
HZB	Helmholtz-Zentrum Berlin
IMFP	inelastic mean free path
ISO	International Organization for Standardization
MA	methylammonium
MACl	methylammonium chloride
MAI	methylammonium iodide
$MAPbBr_3$	methylammonium lead bromide
$MAPbI_3$	methylammonium lead iodide
MASCN	methylammonium thiocyanate
MHP	metal halide perovskite
NaF	sodium fluoride
NMR	nuclear magnetic resonance
NP	nanoparticle
NREL	National Renewable Energy Laboratory
OA	oriented attachment
$PbCl_2$	lead chloride
PbI_2	lead iodide
PCE	power conversion efficiency

PL	photoluminescence
PSC	perovskite solar cell
PTFE	polytetrafluoroethylene
PV	photovoltaic
RSC	Royal Society of Chemistry
SANS	small-angle neutron scattering
SAS	small-angle scattering
SAXS	small-angle X-ray scattering
SEM	scanning electron microscopy
SLD	scattering length density
$SnBr_2$	tin bromide
$SnCl_2$	tin chloride
SnF_2	tin fluoride
SnI_2	tin iodide
XAS	X-ray absorption spectroscopy

Declaration

I hereby declare that I have written all parts of this dissertation independently and exclusively with the indicated resources. In addition, I declare that I have neither previously registered my intention to pursue a doctoral degree nor applied for a doctoral degree at any other university.

Ich erkläre hiermit, dass die vorliegende Dissertation in allen Teilen von mir selbständig und ausschließlich mit den angegebenen Hilfsmitteln angefertigt wurde. Zudem erkläre ich, dass ich an keiner anderen Hochschule zuvor eine Promotionsabsicht angemeldet oder ein Promotionseröffnungsverfahren beantragt habe.

Berlin, Germany
22.11.2021

_____

(Marion Flatken)